

Instituto Tecnológico y de Estudios Superiores de Monterrey

Campus Monterrey

School of Engineering and Sciences



**Data-Driven Modeling of the Mechanics Behaviour of Architected and Soft
Materials for Biomedical Applications**

A thesis presented by:

Josué García Ávila
(He/Him)

Submitted to the
School of Engineering and Sciences
in partial fulfillment of the requirements for the degree of

Master of Science

Major in Manufacturing Systems

Monterrey, Nuevo León, June 14th, 2022

Dedication

I dedicate my dissertation work to my family. A special feeling of gratitude to my dear Mother whose words of encouragement and push for tenacity always ring in my ears.

Acknowledgements

I would like to thank the Tecnológico de Monterrey for giving me the opportunity to realize my Master's degree in Campus Monterrey and support with scholarship for tuition. In addition, I thank CONACyT (Consejo Nacional de Ciencia y la Tecnología) for the living support scholarship.

Words cannot express my gratitude to my advisors and my honorable defense committee, who generously provided knowledge and expertise. I am grateful for the advice and arrangements of:

- PhD. Adriana Vargas Martínez
- PhD. Ciro A. Rodríguez González
- PhD. Erick G. Ramírez Cedillo
- PhD. J. Israel Martínez López
- PhD. Enrique Cuan Urquizo

Thank you for showing me how to cope with the vicissitudes of the Academy and to find joy, inspiration and encouragement even in the most trying moments of this brief and fleeting journey.

CONTENTS

ABSTRACT.....	7
PHYLOSOPHY	8
METHODOLOGY.....	10
BIOMEDICAL BACKGROUND PROBLEM	12
BIOMEDICAL PROBLEM STATEMENT	13
HYPOTHESIS AND RESEARCH QUESTIONS	15
OBJECTIVES	16
THESIS ORGANIZATION.....	17
CHAPTER 1	18
CHAPTER 2	48
CHAPTER 3	68
CHAPTER 4	83

Data-Driven Modeling of the Mechanics Behaviour of Architected and Soft Materials for Biomedical Applications

by

Josué García Ávila

ABSTRACT

The most relevant human-related problems where mechanics has played an important role are primarily due to the intersection with multidisciplinary biomedical applications such as implants or flexible sensors. Recent advances in sophisticated materials with customized properties envision the manufacturing of the future, in which the materials' design is precisely tailored to the purpose of the application. The implementation of data-driven methods from highly dynamic, complex, and nonlinear contexts holds promise for addressing this difficult materials science problem. Engineering has found two classes of materials of particular interest as study objects, namely soft multifunctional materials and architected materials. However, these exhibit difficult mechanical behaviors to fully comprehend, including viscoelastic properties, high nonlinear deformation, anisotropy, apparent properties, unconventional deformation mechanisms, complex manufacturing processes, and hysteresis. Stretchable multifunctional materials are closely related to the study of multiphysics responses from the standpoint of manipulating behavior under specific energy spectrum field, whereas architected materials or mechanical metamaterials can provide structural tensegrity behavior in order to manipulate shape response conditions. This thesis sheds light and insight on some ideas inspired by discussions and reflections to understand these materials via a successful project-based methodology and curiosity-driven research.

PHYLOSOPHY

The research presented in this thesis is based on the four fundamental principles of science and engineering research: *Knowledge, Questions, Experiments, and Data*. Gully A. Burns has masterfully stated this in the following statement:

“Scientific **knowledge** moves forward when a well-defined paradigm permits researchers to analyze their knowledge, formulate **questions** that can be **tested experimentally** so that **data** can be interpreted to generated **knowledge**”.

At a high level, my research work is centered on the construct shown in Figure 1.

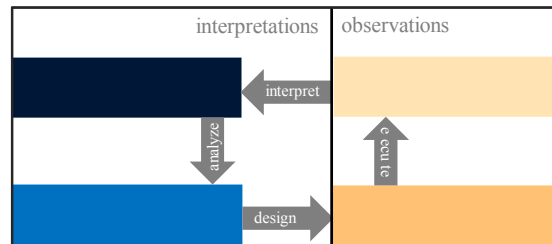


Figure 1. Cycle of the fundamental principles of Scientific Knowledge Engineering (SKE).

A fascinating, unresolved feature of this method of looking at the world is how this simpler, unifying model may be used to grasp the rapid breakthroughs and shifts that occur during a paradigm shift. This is referred to as *Scientific Knowledge Engineering (SKE)*. It is important to note that there are already information structures attempting to drive this cycle: scientific literature, academic conferences, scientific databases, ontologies, advanced analysis methods, scientific workflows, semantic web, and advanced informatics infrastructure. Furthermore, increasingly advanced computational approaches in the field of AI research are constantly being developed that could be applied to scientific knowledge to further expedite our progress over the cycle. An interesting idea instilled by this philosophy is that the research work cycle time is reduced by increasing the proportion of creative tasks as shown in Figure 2. Creative tasks typically involve arriving at multiple design alternatives, design optimization, etc.

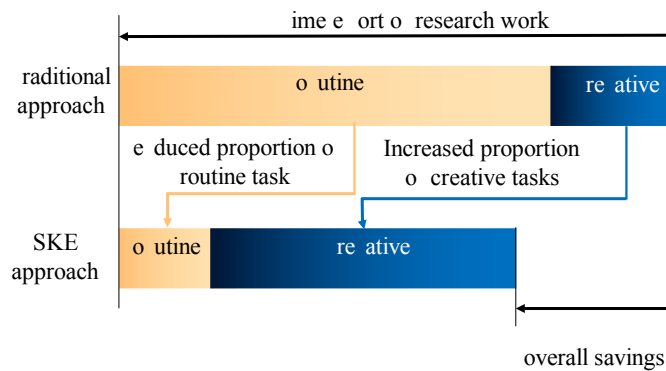


Figure 2. Pareto principle to show the difference and benefits between a traditional research approach and a research work with SKE philosophy.

Building knowledge representations of the domains at hand is a critical first step in any of these strategies. So far, I have mostly focused in this area in establishing the approach known as “Knowledge Engineering

from Experimental Design” (KE ED). In general, this methodology aims to generate a generative model for data based on the experimental protocol that generated the data. Beyond that, the focus is to look for computational approaches to speed up the process of doing scientific work by automating the various steps of the cyclic process described above. This thesis serves as a platform for testing informal new ideas and tracking unique advances in a thesis case.

Finally, SKE can also be defined as the set of *methods* and techniques for knowledge acquisition, application, validation, justification, inferencing, modelling, discovery, representation, reasoning, decision-making, and usage to resolve problems in specific scientific *domains*. SKE is the task of transferring human scientific knowledge into a data-driven system to resolve “comple” problems and is an important groundwork for structuring scientific knowledge. The latter can be illustrated as an introductory form for the explanation of the 7M's methodology applied in this thesis and explained in the next section, in general this can be illustrated in Figure 3.

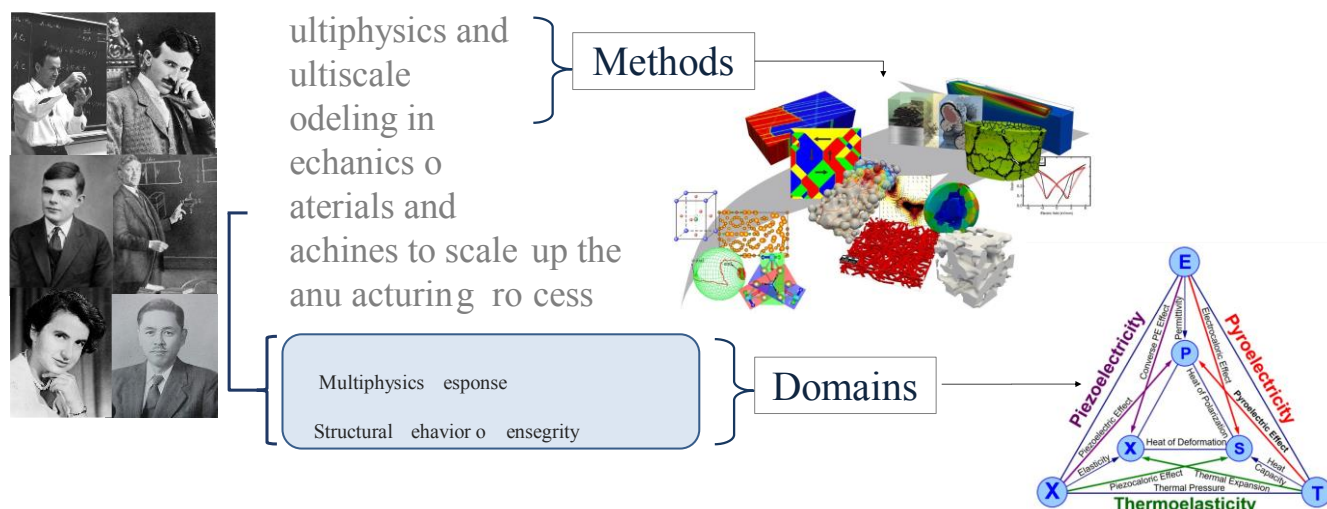


Figure 3. Internet photos of Richard Feynman, Nikola Tesla, Alan Turing, Stephen Timoshenko, Rosalind Franklin, and Taiichi Ohno as distinguished representatives of the various engineering disciplines of the 20th and 21st century; identification of the domains and methods of the 7M’s statement and illustrative images of both concepts (figure of methods from [1], figure of domains -Heckmann diagram- from [2]).

METHODOLOGY

The field of study of all domains of mechanical and materials engineering in the 21st century can be summarized in the following 7M's statement: *Multiphysics and Multiscale Modeling in Mechanics of Materials and Machines to scale-up the Manufacturing Process*. From this baseline, one of the most significant advance that could be achieved in the near future using tools and knowledge in materials science, mechanical engineering, and bioengineering is design and manufacturing of *3D-Architected Soft Living Micro and Nano Machines via Multifunctional Biomaterials*. This exciting objective draws on three important three energy-based subfields: biomachines (life \leftrightarrow movement), architected materials (shape \leftrightarrow structure), and multifunctional soft materials (field \leftrightarrow function). In general, it's possible to achieve a soft material through two main approaches, through the intrinsic nature of the bulk material or through its structuring. For example, the reproducible shape and spatial organization of stem cells imply the existence of physical rules directing the assembly of complex biological structures. The shape and function of cells depend on their controlled tensegrity architecture, self-organizing properties and another physical processes of cytoskeletal networks, an amazing architected and soft living matter. Although this example may appear to be unrelated to the research presented in this thesis, the author does not believe it is. From the mechanistic and manufacturing perspective of the author of this thesis entitled *Data-Driven Modeling of the Mechanics Behaviour of Architected and Soft Materials for Biomedical Applications*, the ultimate goal of this research is understand how to structure matter and endow a soft, stretchable material with functional properties at the macroscale. This thesis is certainly part of a series of interesting *Applications, Artefacts, Attributes, and Abilities* (A's quadrant) related to a multi-and trans-disciplinary research to mimetic the Nature-inspired designs using soft matter.

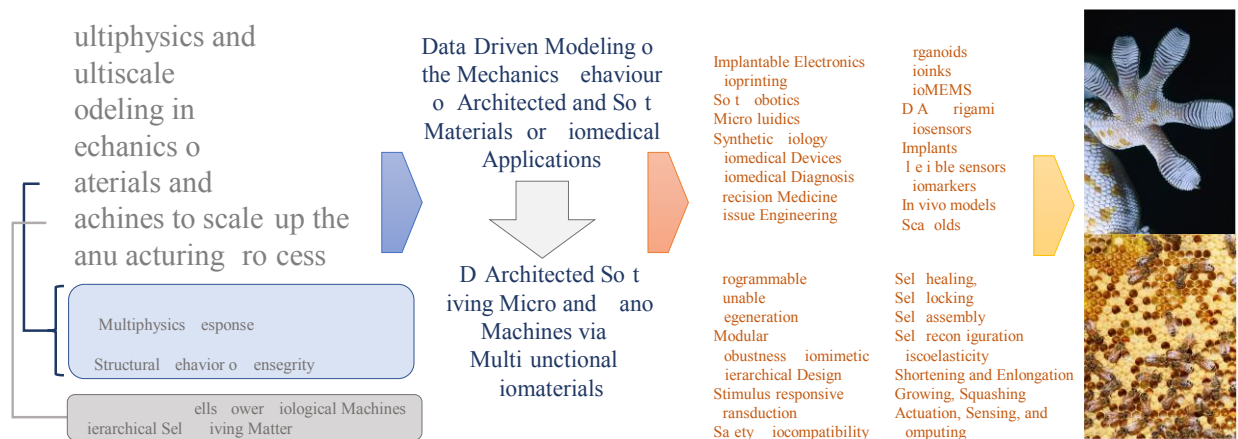


Figure 4. 7M's statement about the core research focus of the 21st century mechanical engineering and material science as well as its derivation to the thesis topic presented here and its implications more broadly using the 4A's quadrant related to a multi-and trans-disciplinary research to achieve Nature-inspired designs using soft matter (figures from [3]).

When we think about the world's top research and development laboratories, we generally think of cutting-edge enterprises, famous university institutions, or well-funded government facilities. But, time and again, Mother Nature has shown to be the finest R&D lab, continuing to churn out new discoveries after 3.8 billion years of trial-and-error. That's right, Nature as Mother, Model, Measure, and Mentor is still the greatest innovator. Since it is often thought that research methodologies for multidisciplinary topics, such as the one presented above and others mentioned in Figure 4, are typically only achieved in research labs with extensive technical staff expertise in specific areas. However, another one approach is to drive the creative solution to the engineering challenge without considering less favorable aspects such as access to material or human resources. The first step is organizing the most relevant topics of the state

of the art by means curiosity-driven research using specific topics inspired from the A's quadrant and thinking about the relationship with 7M's statement presented at the beginning of this section. This has a simple name, sometimes called finding your passion, finding your research interests, or simply seeking inspiration and purpose. This idea allows working on a discovery-driven methodology with the same baseline of knowledge but contributing substantially to a wide range of applications using hypothesis-generating research instead of unclear objective- or hypothesis-driven research. The SARS-CoV-2 pandemic limited access to conducting laboratory experiments and many other facilities for conducting traditional experimental research, the outlook really seemed daunting for many graduate students during the 2020 and 2021 years. The initial stages of the research presented in this thesis focused on the design and computational simulation stages, the final stages of experimentation aimed to build mechanistic models driven by experimental data. The work presented in this thesis is based on the completion of 4 projects with a total of 1.5 months of experimental stage and 22.5 months of design stage, conceptualization, computational simulations, manuscript writing, and seeking inspiration using a curiosity-driven, hypothesis-generating, and project-based research.

BIOMEDICAL BACKGROUND PROBLEM

When it comes to engineering research, the rule is generally a study topic with clearly indicated applicability. This thesis focuses on amputation, a physical condition having profound human and transcendental global and national implications. The amputation of a limb is one of the oldest surgical procedures, Hippocrates, in his book *On Joints* was one of the first to write some basic principles of the amputation of the lower limb [4]. There has been extensive work for a long time to solve the problems amputees face when wearing a prosthetic socket. Interest in the 21st century has led to the development of advanced mechanism systems for prostheses, new materials for sleeves and liner, new socket designs, and there is a particular interest in the advantages of osseointegration to implant prostheses directly to the bone [5], [6]. Currently, most lower extremity amputations can be caused by poor circulation in the extremities due to arterial disease, more than half of amputations occur in people with diabetes mellitus [7]. Looking at published statistics, worldwide, the reported incidence of lower extremity amputation between 1989 and 2010 ranged from 3.6 to 68.4 / 100. 000 in the general population and between 5.6 and 600/100,000 in diabetics [8] of all OECD members Mexico is the country with the highest number of amputations caused by diabetes with an incidence of 20 cases per 100,000 inhabitants [9] and as of 2015 there were 900,000 amputees living in the country, it is estimated that 1 in 10 people are rehabilitated and only 30% of those rehabilitated know how to use their prosthesis [10].

The prosthesis sockets or sockets oversee joining the residual limb with the prosthetic device. In the interaction between the socket and the residual limb, friction and areas of overpressure are generated that cause most patients who use prostheses to have severe injuries to the stump, due to the pain caused by the friction generated in the socket, the probability of not using it increases with the passage of time. These lesions can cause pressure ulcer due to prolonged and excessive epidermal loading [11]. The performance of the socket prosthesis is determined by three main factors, namely the interfacial tension between the residual limb and the socket, the variation in the shape and volume of the residual limb, and the temperature. The stump-socket interfacial pressure, behave differently in conditions of dynamic movements or in static conditions [7]. Numerous authors have conducted extensive research to understand the factors influencing interfacial pressure using novel techniques to model lower extremity biomechanics to gain insight into the positions, velocities, and accelerations of the different limbs of the body [12]. Other authors have implemented the use of other clinical tools to obtain musculoskeletal models of the extremities using magnetic resonance imaging (MRI) [13] and computational multibody mechanical analysis tools [14], [15]. A complete overview on how to implement a framework for the measurement and analysis of residual limb shape and deformation was described by Prof. Herr's research group at MIT, see Figure 5.

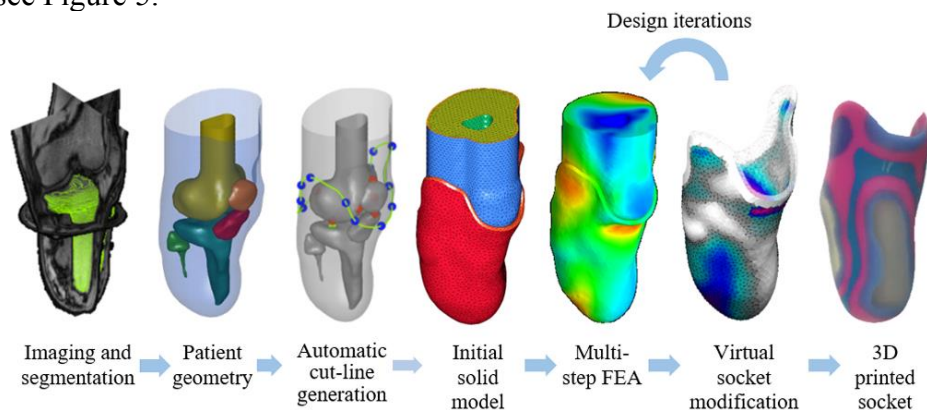


Figure 5. Schematic overview of a data-driven computational design framework (figure from [16], [17]).

BIOMEDICAL PROBLEM STATEMENT

When a person undergoes lower limb amputation surgery, he or she is urged to continue his or her rehabilitation phase. During this waiting time the wounds are expected to heal and heal. With this, it is possible to start fabrication of their new prosthesis 2-3 months after surgery [5]. If a person feels that a prosthesis improves their function and/or appearance, they will use the device. Conversely, if the prosthesis is perceived to impede function or comfort, or the appearance is inadequate, then they will not use the device. As simple as these statements are, they concisely explain the motivations behind the use or abandonment of prostheses [18].

The functional disparities generated by the amputation, such as the relocation of the center of mass, cause asymmetries to develop in the gait cycle, which is why new compensatory mechanisms emerge, such as work amplified produced over the stump hip joint. These non-optimal gait patterns can lead to the development of chronic degenerative morbidities, such as osteoporosis, osteoarthritis, scoliosis and atrophy [19] and if the patient has peripheral neuropathy there is a great propensity for the development of deep ulcerations in the skin that can cause the amputation of the second limb [20].

The origin of the problem is that it has not currently been possible to develop sufficiently comfortable prosthetic sockets and the weight-bearing transmission of bone to the socket do not have sufficient mechanical stability. The other problem is that little measurement information is available on the interaction of the residual limb within the socket. In general, the problems associated with socket-stump interaction are due to three phenomena, namely, overpressures at the contact interface, the change in volume of the die and the internal temperature of the socket (thermoregulation). For example, Figure 6 shows that the stump has areas that are more sensitive or more tolerant to pressure. The ideal socket design should allow the forces to be distributed over as large a residual surface as possible and to be applied as evenly as possible over the pressure-tolerant areas.

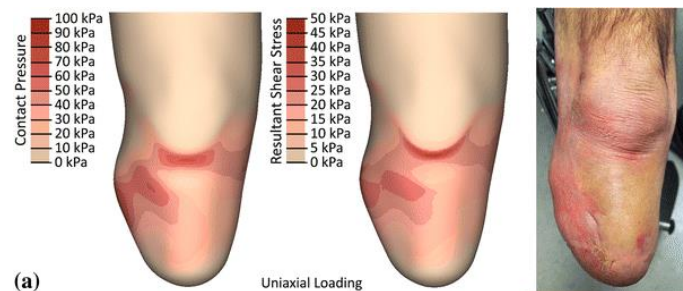


Figure 6. Pressure-sensitive areas in a transtibial residual limb patient who experienced a one instance of breakdown on the anterior aspect (figure from [21]).

Nowadays, estimating the interfacial pressure of the stump and socket for better design sockets has not been resolved in a simple and practical way to be replicated. Many of the sensing systems are adapted to sockets and liner with no thought for patient comfort and only work using expensive equipment or under specific study conditions. For example, the use of sophisticated and expensive technologies such as X-Ray Videofluoroscopy [22]–[24], however it is still a technology that involves its health risks and is not suitable for most situations of prosthetics and orthotics workshops in developing countries.

The first approach to this widely studied problem allows to contribute through the development of a smart flexible sensor that allows modeling the pressure system. The socket-stump interface is the one that plays an important role in the transmission of the weight towards the ground, the interface is made up of 4 essential elements: The bones (tibia, fibula, femur), soft tissues (e.g., quadriceps muscle, patellar

tendon, etc.), liner and the hard socket. To this day the sensing technologies for measuring stress distribution in interface socket-stump can be strain gauges, piezoresistive, capacitive or optical ones. Figure 7 shows a proposal through a Tekscan solution using a piezoresistive sensor array (F-Socket).



Figure 7. Example of implementation of acquisition systems for interfacial pressure measurement and color pressure mapping (figures from [25], [26]).

However, these sensing systems also remain expensive and sometimes the number of measurement points is limited by the number of sensors used, the size of the sensors creates discomfort during the study and limits research in outdoor conditions. The research proposal is to fabricate a soft conductive sensor with inexpensive fabrication techniques that can measure interfacial pressure without causing pain and discomfort during clinical studies. In addition, this research will allow future researchers to better understand the integral loading process of prostheses, the pressure produced on the residual limb due to socket geometry, and to have a better tool for socket design evaluation and validation. This idea is based on the continuous development and integration of these sensing technologies to achieve the future development of intelligent socket prostheses. These intelligent socket systems will not only function as socket prostheses but will be able to detect the parameters that cause discomfort to the amputee and self-adjust to optimize their prosthesis, its function, and its performance.

Typically, the most explored domains address residual limb deformation and enhance socket design; nevertheless, there are other lines of research that have received minimal attention, such as surgical techniques or the examination of gait cycle kinematics using motion capture systems, see Figure 8. This thesis addresses another approach little studied to improve the mechanical stability of residual limb bones and thus weight-bearing, this domain has been studied through the design of osseointegrated implants, the intention is to focus the solution of the problem having as a subject of study the mechanical stability of residual limb bones and their mimetic mechanical properties.

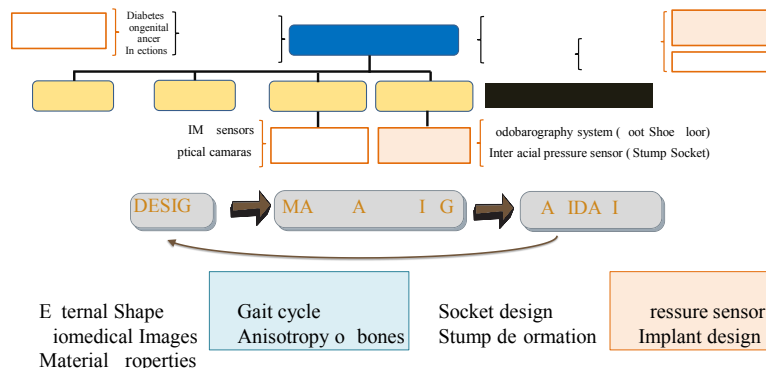


Figure 8. Schematic of the different domains related to amputation in order to define new lines of research.

HYPOTHESIS AND RESEARCH QUESTIONS

This thesis work is founded on the idea that utilizing an elastomeric material as a basis and a filler conductive material, it is feasible to fabricate at low cost a soft and high flexible sensor that is comfortable for the patient and reliable enough to monitor the interfacial pressure of the socket-stump interface with a matrix design with enough measurement points. On the other hand, the feasibility of modeling a mechanically optimized porous design from dynamic force data derived from previously reported gait cycles with acceptable and customizable anisotropy properties is used in implant design to improve mechanical stability and weight-bearing transfer. The research questions which shall be answered in this project are the following:

Domain #1, *Soft materials*: Pressure soft and stretchable sensor:

- How to provide conductive properties to a flexible material?
- What is the best conductive material for making easily conductive layers using an elastomer as a base material?
- Are there low-cost manufacturing processes for mixing the conductive material into the flexible material?
- What is the maximum deformation and stress that the conductive flexible material can undergo before breakage mechanics occurs?
- Is it possible to predict and computationally model complex scenarios of nonlinear material deformation?

Domain #2, *Architected materials*: Transtibial implant design:

- How to computationally model materials with the anisotropy mimetic properties of bone?
- Are porous microstructures sufficiently mechanical resistant to compressive fatigue?
- Is it possible to establish a suitable design framework from medical image acquisition to implant fabrication?
- Can gait cycle data be useful for dynamically optimizing implant design?
- What is the best method for incorporating patient kinematics into implant design?

OBJECTIVES

Domain #1, Soft materials: Pressure soft and stretchable sensor:

Objectives:

- Synthesize a soft and stretchable material with *conductive properties*.
- Validate a *low-cost manufacturing process* to synthesize the flexible conductive material.
- Fabricate conductive layers with *embossed geometries* in a pattern design configuration.

Domain #2, Architected materials: Transtibial implant design:

Objectives:

- Design *porous structures* with similar mechanical properties of bone.
- Study the *fatigue behavior* at compression of porous materials.
- Fabricate an *optimized implant* considering dynamic loads.

THESIS ORGANIZATION

Two of the projects are related to the mechanical study of anisotropy and fatigue of architected materials based on porous media mathematically modeled by level surfaces, and the use of novel dynamic topological optimization techniques to fabricate a transtibial implant with PEEK using additive manufacturing, the most important modeling data derived from medical imaging and previously reported data. Soft materials were studied by means of two projects to fabricate flexible conductive material using RTV, PDMS, and different loading SWCNTs filler, and the mechanical properties were characterized using specific mechanical tests based on soft materials' unconventional deformation mechanisms. The four projects illustrated in Figure 9 rely heavily on computational simulation approaches in conjunction with mathematical and mechanical models based on stiffness tensors, energy approximations, equations of motion, multibody models, optimization algorithms, deep learning, and state-space models. As a result, the thesis is divided into four main chapters, each having a structure similar to that of an individual publication, i.e., introduction, materials and methods, results, and so on. The four chapters cover the following topics:

- **CHAPTER 1:** Novel Porous Structures with Non-Cubic Symmetry: Synthesis, Elastic Anisotropy, and Fatigue Life Behavior.
- **CHAPTER 2:** Tunable Isotropic Design and Dynamic Topology Optimization of Transtibial Orthopedic Implant with 3D-Printed Structurally Porous PEEK.
- **CHAPTER 3:** E-Skin Development and Prototyping via Soft Tooling and Composites with Silicone Rubber and Carbon Nanotubes.
- **CHAPTER 4:** Modeling of Soft Stretchable Nanocomposite using Recurrent Neural Networks.

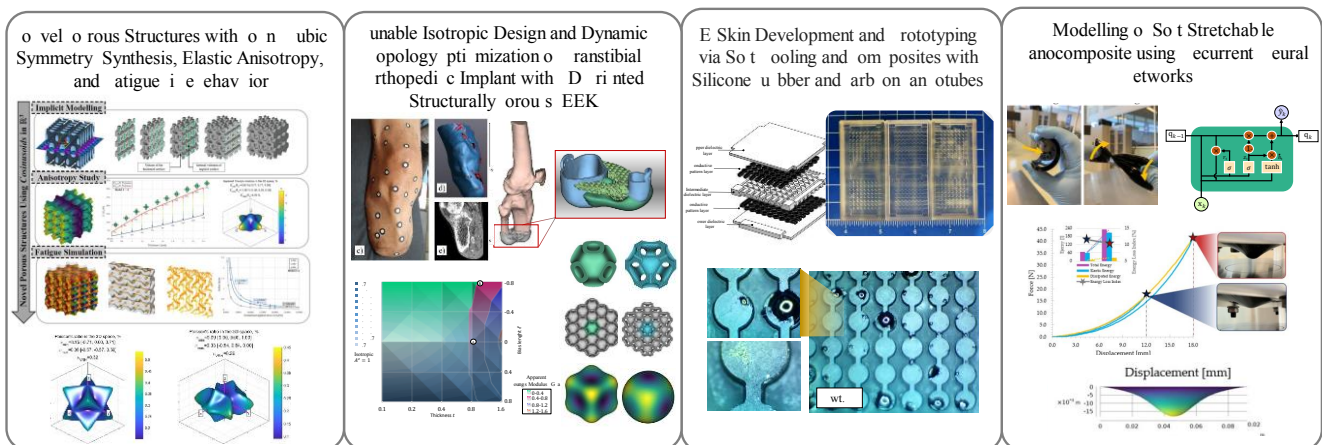


Figure 9. Chapter title and representative diagrams of the four projects developed and presented in this thesis to address the topic of architected and soft materials.

CHAPTER 1: Novel Porous Structures with Non-Cubic Symmetry: Synthesis, Elastic Anisotropy, and Fatigue Life Behavior.

Abstract	18
1. Introduction	19
1.1. Related Work	20
1.1.1. Synthesis of Surface(sheet/plate)-based Porous Structures	20
1.1.2. Current Challenges of Anisotropy in Artificial Porous Structures	20
1.2. Objective	21
2. Materials and Methods	22
2.1. Simulation Workflow Framework	22
2.2. Implicit Modeling and Relative Density	23
2.3. Mechanical FEM Simulation and Anisotropy Study	24
2.4. Curvature Estimation Method	25
2.5. Compression Fatigue Testing	26
3. Results	26
3.1. Defining the Concept of Families of Porous Structure Using Cosine Surfaces	26
3.2. Mathematical Modeling of Orthotropic Porous Structures and Relative Density	29
3.3. Mechanical Simulation and Apparent Elastic Linear Properties	29
3.3.1. Stiffness Scaling and Elastic Surface Variations	29
3.3.2. Linear Modulus Averages	34
3.3.3. Compression Fatigue Behavior of Porous Structures	34
4. Analysis and Discussion of Results	35
4.1. Relative Density and its Relation to Wall Thickness	36
4.2. Apparent Properties, Scaling Laws, and Curvature Classification	36
4.3. Anisotropy of Porous Media	38
4.4. Fatigue Properties of Porous Structures	40
5. Conclusions	41
Appendix A The Elastic Anisotropy for Cubic and Orthotropic Structures	42
Appendix B Anisotropy Indexes	45

Abstract

Natural porous structures are often anisotropic in their elastic properties, i.e., they have directional variations that are related to their topology and geometry. This paper presents the synthesis and simulation framework of novel families of non-cubic porous structures based on implicit modeling of cosine surfaces in the three-dimensional Euclidean space. The synthesis was performed using Field-Driven Design (FDD). An in-depth study of the elastic properties and simulated fatigue compression-compression behavior of a selection of five structures from the orthotropic anisotropy family is presented as case studies exposing the stretching-dominated mechanisms. The apparent properties characterized

include Young's modulus (E^*), Poisson's ratio (ν^*), shear modulus (G^*), bulk modulus (K^*), and relative density $\bar{\rho}$. A systematic approach to the characterization of average apparent properties was performed according to the schemes of Voigt, Reuss, and Hill. We show the anisotropic variation of the cosine surface-based porous structures using the Universal Elastic Anisotropy Index (A^U) and compare it with six well-known triply periodic minimal surfaces (TPMS) structures by analyzing the stiffness tensor to validate and discuss which individual property (stiffness, rigidity, compressibility) have a higher impact on the final anisotropy value. We also provide a formal curvature analysis, based on the notions of mean (\mathcal{H}) and Gaussian (\mathcal{K}) curvatures to evidence the ridge-shaped surface in the structures. The proposed porous structures showed advantages when compared to cubic TPMS structures. From the data processing of the five analyzed porous structures, two synthesized structures have $A^U=0.394$ and 0.478 , which are lower values than the structures based on Neovius and Schwarz's Primitive surfaces with $A^U=0.529$ and 0.604 . In addition, simulation results of cyclic compressive fatigue loading indicate that the fatigue resistance properties of the non-cubic porous structures are higher than the TPMS structures.

Keywords: anisotropy; field-driven design; porous structure; fatigue; triply periodic minimal surface; metamaterials.

1. Introduction

Porous structures have apparent properties different from the intrinsic properties of their base material due to the discontinuity (voids) generated in their structural topology. In general, porous structures can be classified into beam or struts-based structures and surface-based structures with or without curvature. The great advantage of surface-based porous structures is that they tend to have lower stress concentration levels than structures based on struts or beams [27]. With an appropriate representative volume element (RVE) of the periodic porous structure, it is possible to derive the mechanical properties from the 6×6 stiffness tensor induced with macroscopic external stresses [28]. These *apparent* properties (E^* , ν^* , G^* , and K^*) represent the *effective* properties of material only when periodic boundary conditions (PBC) are applied on a periodic structure (even if applied to a single unit cell). One of the methods available to quantify the mean values of these apparent properties is the Voigt-Reuss-Hill model using arithmetic and harmonic weighted average values, which are the values used for the calculation of the Universal Elastic Anisotropy Index (A^U). This V-R-H average approach was earlier applied to highly anisotropic structures (bone, rocks, polycrystalline materials, advanced composite materials) where in many cases the stiffness tensor symmetry could not be assumed or known and where the directional mechanical behavior of the material cannot be represented by means of 2 independent elastic constants (E , G) but by means of the whole stiffness tensor with reliable rigorous first-order bounds. This schema is also valid for porous media with a single isotropic base material (or single solid phase) from the point of view of micromechanics [29]–[31]. Nevertheless, once fabricated, the actual apparent mechanical properties (uniaxial, shear, and bulk moduli, Poisson's ratio) of these porous structures are closely related to their manufacturing techniques, geometry, anisotropy, porosity distribution, and unit cell scalar and vector sizing [32].

The synthesis and modeling of porous structures with complex, improved and customizable characteristics are benefited from novel advances in implicit modeling and Field-Driven Design (FDD) embedded in computer-aided design (CAD) [33] and more efficient Finite Element Modeling (FEM) simulation homogenization methods [34]. During the design process and topological synthesis of porous structures, the effects of porosity must be considered regarding the estimated fatigue life. As with the elastic modulus and other mechanical properties, a higher porosity results in an increase in the value of

absolute stresses due to the reduction of the effective area. The latter leads to a correspondingly lower value of the number of cycles to the failure of the structure [35]. Given the potential use of these porous structures as an essential part of the design of bone substitutes and implants, compression-compression is the most relevant loading mode, so most of the studies carried out on the fatigue behavior of porous structures use this loading regime. Another important recent observation is that surface-based structures strongly outperform beam-based structures in their fatigue resistance [36], [37].

Porous structures have other favorable properties, e.g., high specific surface area and high permeability. Consequently, porous structures, referring to porous materials, can be classified from several aspects, e.g., as natural or artificial solids with closed or open pores, voids, cavities, channels, or interstices with variable shapes and curvatures [38]. Families of periodic level surfaces have been proposed as candidates for modeling microdomain morphologies in block copolymers (BCP) known as separated microphases. Of particular interest are spheres, cylinders, sheets, and triply periodic bicontinuous morphologies [39]. Even simulations generate novel non-native morphological structures beyond conventional structures, such as perforated/modulated lamellar morphology, coaxial cylinders or double diamond with core, still without formal mathematical representation by level surfaces [40], [41].

1.1. Related Work

1.1.1. Synthesis of Surface(sheet/plate)-based Porous Structures

Plate-based designs (without curvature) use the vertices of a beam-based topology as a base template; the solid plates are the faces formed by the vertices or intersections of the structure. Different types of these structures can be achieved by proposing different base lattices (e.g., FCC, BCC, etc.) and varying the thickness of the plates to change the relative density (volume fraction) [42]. Alternatively, mathematically elaborated designs, called triply periodic minimal surfaces (TPMS), have been synthesized (see Table A. 1). TPMS structures are unique as their mean curvature H is zero, i.e., the curvature is constant. Application in specific cases of porous structures has generally been limited to the use of TPMS structures [43]. Lattice structures with unit cells based on TPMS have a minimal surface in Euclidean space \mathbb{R}^3 but are not exclusive; for example, non-periodic porous structures based on curved surfaces have recently been developed using the concept of the level surface of Gaussian random field called *spinodoid* [44].

Other researchers have developed new topologies designs called *functional graded* that are generated by varying morphological parameters gradually [45]. These modeling techniques can be divided into three different types: multi-morphology set, relative density grading set, and cell size grading set [46]. However, all applied research works have taken the TPMS structures as a starting point and have been categorized in some way as the *de facto* basic structures in the absence of other novel porous structures for a long time even though they are only a family of morphological descriptors known as *tensorial Minkowski functionals* [46]–[49] and *Periodic Nodal Surfaces* [50].

1.1.2. Current Challenges of Anisotropy in Artificial Porous Structures

Anisotropy can be expressed as a function that quantifies the variation of the scalar magnitude of some properties (mechanical, thermal, acoustic, etc.) of the base material in all spatial directions. Nowadays, it has been possible to obtain almost isotropic porous structures [51]. However, in current promising applications of porous structures, their design and topology must consider other phenomena where total isotropy is not necessarily required. These phenomena where porosity is relevant are usually related to

mass vs. strength optimization or energy transport and diffusion processes such as those occurring in natural porous structures like bones or muscle tissues [52].

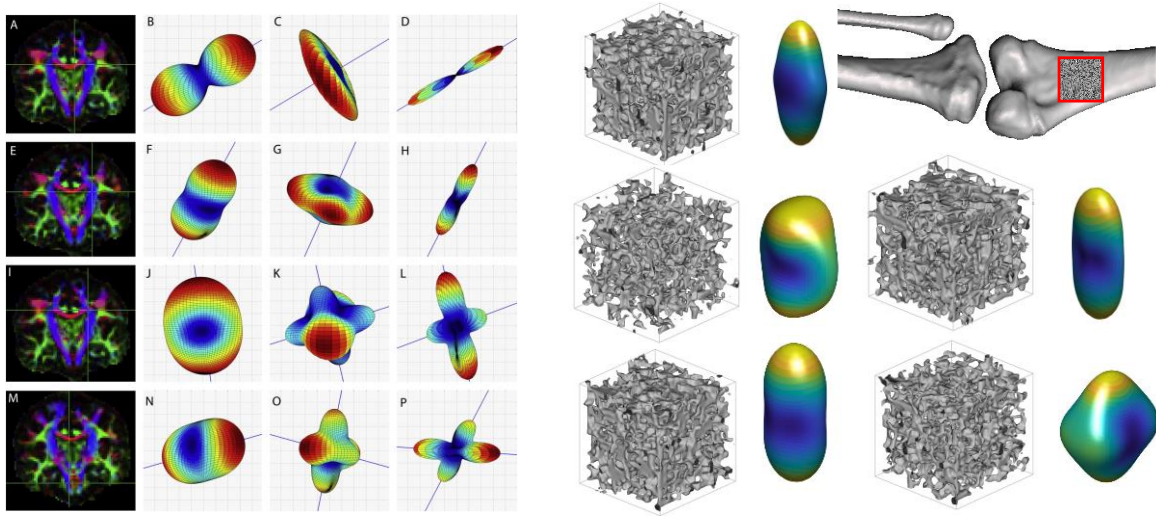


Figure 1. (a) Estimates of neural fiber orientation using the orientation distribution function (figure from [53]); (b) trabecular bone anisotropy using stiffness tensor processed here using data from [54].

Advances in medical imaging techniques have made it possible to know that many of these promising applications for artificial porous structures tend to have behaviors not only with *cubic* but also *orthotropic* anisotropy. Therefore, one of the current challenges is to achieve anisotropy customization for orthotropic structures, where optimization of mechanical properties is required for each principal axis independently. Furthermore, a customized and oriented anisotropy is required to improve compatibility and performance, as found in nature illustrated by trabecular bone [55] or in brain tissues (see Figure 1).

1.2. Objective

The study's objective reported here is to propose a new set of novel porous periodic structures based on the properties of cosine surfaces allowing customized elastic properties and anisotropy. Section 2 describes the methodology for the implicit modeling of the structures, curvature estimations, and their computational apparent mechanical characterization, which includes relative density ($\bar{\rho}$), Young's modulus (E^*), Poisson's ratio (ν^*), shear modulus (G^*), and bulk modulus (K^*) using the stiffness tensor obtained by Finite Element Analysis (FEA) and fatigue life estimation by uniaxial compression.

The analysis of the elastic constants of the apparent properties E^* , K^* , G^* , and ν^* are reported following 3 different approaches as:

1. Maximum and minimum values (upper and lower limits) of the whole spectrum of the 3D structure are reported to quantify the full variation of apparent properties. In addition, the apparent property E^* is used to further study the stiffness scaling law when analyzing the evolution of the anisotropy of Young's Modulus as the thickness t varies (relative density). This allows us to obtain fit coefficients for the classical scaling law and compare them with other values reported previously in the literature of porous structures and deformation mechanisms.
2. We report the 3D spatial representations and 2D polar projections of the principal planes of normalized apparent properties for all the structures, including the TPMS structures selected for

the comparison, the labels in each figure not only indicate the maximum and minimum values mentioned in the previous point but also the axis orientation by means of a vector $[x,y,z]$. This leads to the association of these orientations with the fatigue performance of the porous structures since the fatigue compression test was performed in the principal x,y,z directions of the structure.

3. We report average values of E^* , K^* , G^* , and ν^* via Voigt, Reuss, and Hill schemas. The Universal Anisotropy Index A^U uses these average schemas to weight the overall anisotropy of the structure to a single index number. Knowing these independent average values allows us to validate and discuss which individual property (stiffness, rigidity, compressibility) has more impact on the final anisotropy value.

The apparent properties E^* , K^* , G^* , and ν^* are reported as normalized values with respect to the elastic constants of the base material (E_s , K_s , G_s , and ν_s ; each of them is calculated from the tensor \mathbb{C} which was obtained from the computational homogenization of each porous structure under PBC. The structures are quasi-anisotropic with controlled and known symmetry which allows us to analyze and associate the direction with specific properties by means of the constants using the three approaches mentioned above, that is why we find more understanding of the stiffness behavior of porous materials from elastic constants than of the second-rank stiffness tensor since a \mathbb{C} tensor follows a more phenomenological fundamental charge while the elastic constants provide a more engineering perspective [56]. The results of these procedures are presented in Section 3. Section 4 discusses the findings of the porous structures' results, emphasizing the structures with orthotropic anisotropy and a comparison with six widely known TPMS structures. Finally, Section 5 provides some concluding remarks.

2. Materials and Methods

2.1. Simulation Workflow Framework

The workflow followed for the synthesis, modeling, and analysis of the new porous structures includes the sequence of steps presented in Figure 2a. The Software used is nTopology 3.1.2®. The implicit equations and the linear elastic results and the 6×6 elastic tensor matrix \mathbb{C}_{ij}^* are obtained from the Math and Design Analysis modules, respectively, proprietary to nTopology. Figure 2b shows the colormap representation of the scalar field of an implicit function generated in nTopology; this process is known as Field-Driven Design (FDD). MATLAB R2020® and an adaptation of AnisoVis toolbox [57] were used to calculate the normalized elastic moduli and 3D/2D graphical representations. The fatigue simulations were performed in ANSYS Mechanical 2021 R2®. Computational homogenization by the finite element method (FEM) was used, using a cubic representative volume element (RVE) of size $20 \times 20 \times 20$ mm for each presented porous topology made of a homogeneous and isotropic linear elastic base material (with Young's modulus $E_s=205$ GPa, yield strength $\sigma_Y=250$ MPa, and Poisson's ratio $\nu = 0.3$).

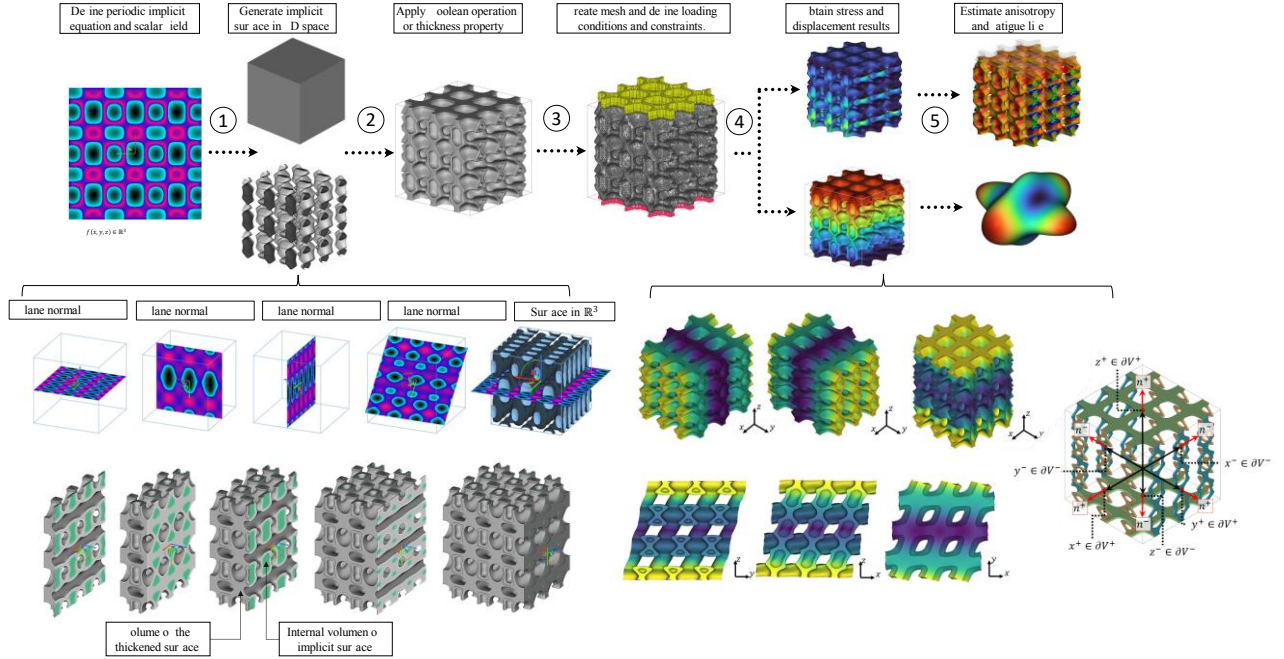


Figure 2. (a) Methodology for the design and testing of anisotropy and fatigue of porous structures from cosine surfaces in \mathbb{R}^3 ; (b) example of the generation of a surface from a scalar field of an implicit equation and cross-sections of the porous structure, the green color is the internal volume of the implicit surface, the gray color is the volume of the thickened surface; (c) RVE under six loading conditions and application of the periodic boundary condition: Pure x, y, z tension and pure xy, xz, yz shear.

The computational homogenization procedure requires the results of six independent elementary loading cases in the RVE under periodic boundary conditions, see Figure 2c. The latter means considering a cubic RVE, and each opposing pair of their parallel faces ∂V^+ and ∂V^- there is each point $+x$ in ∂V^+ that is related to a unique point $-x$ in ∂V^- (similarly for y -axis and z -axis) with unit outward normal vectors n^+ and n^- , respectively. Therefore, identical meshes on opposite faces must guarantee the satisfaction of the periodic boundary condition. Each of the six load cases defines a component of the compliance tensor, which refers to three uniaxial extensions and three shear deformations. The uniaxial compression fatigue condition is a basic case of side ∂V^- restraint with no displacement and normal load application on the ∂V^+ side with applied normalized stress equal to 30% below the yield strength σ_Y .

2.2. Implicit Modeling and Relative Density

The implicit equations are of the form $f(x, y, z)$. In the implicit form, the dependent variable is not explicit with respect to the independent variable. If one has a scalar field of three variables $f(x, y, z)$, the points (x, y, z) satisfying $f(x, y, z) = 0$ form, in general, a surface S . Then $f(x, y, z) = 0$ is said to be the implicit equation of S or implicitly defining surface $S \in \mathbb{R}^3$. nTopology is a flexible platform that can easily model scalar fields (spatial representation of the implicit equation) and virtualize surfaces from them to obtain CAD models. The volume enclosed (void) by the S surface V_{surface} is useful to calculate the relative density $\bar{\rho}$ of the porous structure, which is calculated from the equation $\bar{\rho} = V_{\text{surface}}/V_{\text{solid}}$. The volume of a surface V_{surface} is calculated internally according to the equation $V_{\text{surface}} = \iiint_{\mathcal{C}} f(x, y, z) dx dy dz$ [58].

Once a surface is obtained, it is possible to generate a porous volumetric structure. The first option is by Boolean intersection operations with the existing continuous solids. The second option is the thickening of the wall (off-set operation) so that the implicit surface can generate internal voids (porosity) in the material, as shown in the sequence of images in Figure 2b. In this paper, the second method is used to generate the surfaces, and the porous structures formed from them are contained in a $20 \times 20 \times 20$ mm bounding box. The calculation of the volume was performed directly by CAD software using default computational numerical approximations. For example, thickness values greater than half of the unit cell periodicity result in an overlapping of wall volumes, however, in some other areas, capricious concavities with different dimensions are usually generated which are only filled with $t > k/2$ of certain surfaces (see Figure 3).

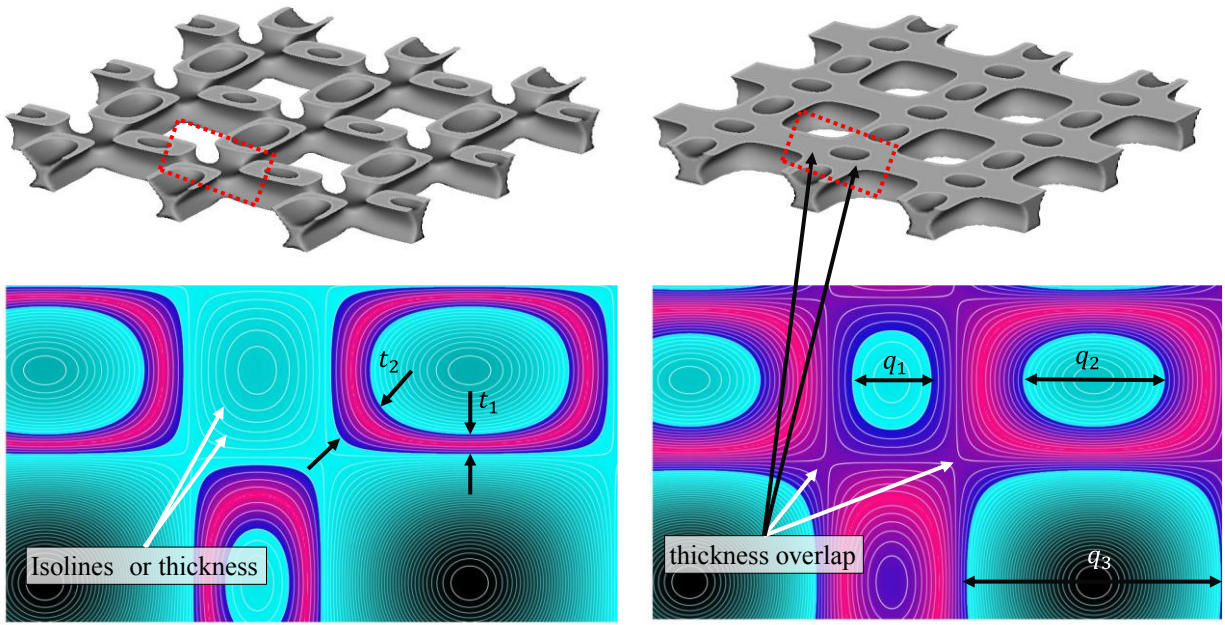


Figure 3. (a) Cross-sections of the same porous structure with thickness $t = k/4$ and $t = k/2$: Shows the isolines and deformation of thickness with $t_2 > t_1$; (b) Thickness overlap and dimensions of three different capricious concavities with dimensions $q_3 > q_2 > q_1$ (if k is the period of the porous structure always $q_{1,2,\dots,n} < k$).

2.3. Mechanical FEM Simulation and Anisotropy Study

When the 3D model is obtained, the next step of the methodology consists of meshing the volume or surface. There are several meshing techniques and types of finite elements, and it depends mainly on the complexity of the solids and the type of analysis to be performed. Convergence studies revealed that a mesh greater than 500,000 elements and 800,000 nodes is sufficient to calculate the apparent stiffness tensor; the characteristics of the meshing performed for the simulations of this work are listed in Table 1. Additionally, we implemented a homogenization scheme with periodic boundary conditions to calculate the modulus in all directions, first obtaining the full elastic modulus tensor \mathbb{C}^* and then extracting the compliance tensor $\mathbb{S}^* = \mathbb{C}^{*-1}$, which gives the magnitudes of the various apparent elastic properties (E^* , G^* , K^* , ν^*) along with arbitrary directions (see more in Appendix A). Finally, the apparent properties are normalized with respect to the moduli of the constituent materials; the relationship between the apparent property of the material E^* and the relative density $\bar{\rho}$ is generally studied by means of the scaling law $E^*/E_S = C\bar{\rho}^n$.

Table 1. List of essential characteristics of the finite solid elements used for fatigue testing and calculation of the stress tensor of porous structures.

	V
Edge length	. - . mm
Shape	riangle
Span angle	. °
Growth rate	
eature angle	. °
Min. edge length	. mm
hord height	A
Min. eature size	. - . mm

A set of 3D surfaces and 2D polar plots projected onto principal planes ([100], [010], [001]) are used to visualize the anisotropy of the elastic properties of porous structures. For any radius vector measured from the origin to the 3D volumetric surface, the radius proportionally represents the scalar magnitude of the elastic properties in that specific direction. The above visualization methods can be used to represent elastic properties such as Young’s modulus, where the property is a single scalar value for a specific direction. Young’s modulus is the ratio of uniaxial stress to uniaxial strain, and it is understood that the directions of stress and strain are colinear. However, for Poisson’s ratio and shear modulus, this is not the case. Poisson’s ratio is transverse strain to axial strain, so it implies two orthogonal directions. The shear modulus is the ratio of shear stress to shear strain, with directions perpendicular to each other. For a stress (normal or shear) applied in a specific direction, there is only one value of E^* , but there are many possible values of ν^* and G^* . To plot the surfaces representing ν^* and G^* , the minimum and maximum values calculated for stress applied along each direction in 3D space are taken [59]. The estimate of anisotropy is based on the Universal Anisotropy Index (A^U) (see Appendix B).

Finally, the average apparent moduli and the A^U index of the different properties of the six TPMS structures (Gyroid, SplitP, Lidinoid, Primitive, Neovius, and Diamond) with cubic anisotropy were calculated following the same methodology as described above, the results are attached in the Appendix A. This is taken as a point of comparison, and since to the best of our knowledge, no such index has been reported in the scientific literature for these structures.

2.4. Curvature Estimation Method

To quantitatively describe surface curvature requires two independent measures. The most common choices are either the two principal curvatures (i.e., the maximum and minimum curvatures, κ_1 and κ_2 , respectively), or the pair of the mean $\mathcal{H} = (\kappa_1 + \kappa_2)/2$ and Gaussian $\mathcal{K} = \kappa_1 \times \kappa_2$ curvatures. Note that last both measures are dimensional, with the mean curvature having the dimension $[1/l]$ and the Gaussian curvature having the dimension $[1/l^2]$, where l is the length dimension. In this paper, the calculated Gaussian and mean curvatures are made from a triangular mesh which is regular, orientable, closed surface with boundary in the Euclidean space \mathbb{R}^3 . We use the scale-dependent quadric filtering estimator method from MeshLab 2021.10 software which involved normal vectors and vectors between the point of smooth estimation and their neighbors in order to estimate local convergent curvature results via an Umbrella operator. Then, we used two approaches to evidence the shape classification space of porous structures using the pair mean-Gaussian curvatures [60] (see Table 2) and the shape index [61], the latter is a dimensionless and scale-independent surface measure and can be calculated as:

$$SI = \frac{2}{\pi} \arctan \frac{\kappa_2 + \kappa_1}{\kappa_2 - \kappa_1} = \frac{2}{\pi} \arctan \frac{\mathcal{H}}{|\mathcal{H}| - \mathcal{K}} = , (\kappa_1 \geq \kappa_2 \text{ and } \mathcal{H}^2 \geq \mathcal{K}) \quad \text{Equation}$$

The shape index has a value between -1 and 1, classifying intuitively complex surface-based structures a continuous gradient of ridge, rut, saddle, and another shapes.

Table 2. The primitive folding combination possible eight shapes at a point considering the signs of mean curvature \mathcal{H} and Gaussian curvature \mathcal{K} .

	$\mathcal{K} > 0$ elliptic	$\mathcal{K} = 0$ parabolic planar	$\mathcal{K} < 0$ hyperbolic
$\mathcal{H} < 0$	eak	idge	Saddle ridge
$\mathcal{H} = 0$	Impossible	lat	Minimal sur ace
$\mathcal{H} > 0$	it	alley	Saddle valley

2.5. Compression Fatigue Testing

Fatigue studies were performed by applying uniaxial compressive cyclic loads with constant periodic amplitude (proportional loading). The constant application is zero-based, i.e., a load was applied and then removed with a constant load ratio, $R=0$. R is defined as the ratio between the minimum and maximum values of the absolute load stress. The type of analysis was of the stress life type based on $S-N$ curves (Stress-Cycle curves). The stress-life type refers to a relatively high number of cycles ($>10^6$ cycles). The mean stress correction used was the Soderberg correction as it is a conservative approximation of any combination of mean and alternating stress above or below the Soderberg line defined by $\sigma_a/\sigma_e + \sigma_m / \sigma_Y = 1/SF$, where σ_Y is the yield strength of the base material, σ_e for endurance limit, σ_a is the stress amplitude, σ_m is the mean stress, and SF stands for fatigue safety factor. It is usual to normalize the stress level to the yield stress (or plateau) of the porous structure and calculate the so-called normalized $S-N$ curve [34]. The von Mises stress σ_{VM} is a material failure criterion used in the design and analysis of porous periodic structures in several works [62]–[64] and which was also used in the present manuscript. The criterion states that, to avoid failure, the von Mises stress must be less than the yield strength σ_Y of the material under complex loading from the results of uniaxial tests. Therefore, the values of the $S-N$ curves were normalized with respect to yield strength. However, it should be understood that failure in slender porous materials at low relative densities is also governed by buckling instabilities that occur prior to material failure [65].

3. Results

3.1. Defining the Concept of Families of Porous Structure Using Cosine Surfaces

The cosine function differs from other trigonometric functions due to its symmetry properties concerning the origin (0,0,0) because it is an even function. Also, it is a periodic function in the interval $(-\infty, +\infty)$ and it is a fundamental part for a powerful tool such as the Fourier series widely used to approximate or converge continuous functions with linear combinations. It is important to emphasize that TPMS structures and any other cosine-based porous structure (*cosinusoids*) can be fully represented by the following scalar field of Fourier series $\phi(\mathbf{r}) = \sum_k A(\mathbf{k}) \cos[2\pi\mathbf{k} \cdot \mathbf{r} - \alpha(\mathbf{k})]$, where \mathbf{k} is the reciprocal topology vectors for a given topology, $\alpha(\mathbf{k})$ is a phase shift, and $A(\mathbf{k})$ is an amplitude associated with a given \mathbf{k} -vector [66], [67].

To show the potential of modeling porous structures based on the cosine equation, a classification of surfaces generated using Field-Driven Design (FDD) of implicit functions is proposed (see Figure 4). This rational classification is based on and inspired the Landau-Ginzburg model of phase transition

theory [66] and in the work of Schnering and Nesper about periodic space partitioners [68], [69]. The classification is divided into eight main morphological families classified according to the shape of the generated surface. The synthesis of the first three families is guided by the following premises, while the rest of the families are a specific mix of these same attributes mentioned below.

1. The first family (Figure 4-1) are structures with continuum cubic morphology very similar to the TPMS (not necessarily with constant curvature), to achieve this requires the same periodicity, shrink and shift factors in the three axes x , y and z and must be composed of homonymous functions between them, example $z = x \cos x$ is homonymous or isomorphic with $z = y \cos y$, i.e., if an orthogonal rotation transformation is applied, the surface is the same. The available range of relative density values that can be obtained from the same base equation is limited using the amplitude coefficients. As shown in Table 3, the same equation is used to obtain four different structures (the coefficients k_1 and k_2 are selected to control the shape of the voids). For instance, the morphogenesis and effect of the amplitude coefficients on their relative density, when k_2 increases with respect to k_1 (see Figure 5a). This simple analysis allows us to understand that it is possible to construct a quasi-square lattice ($k_1 = 1$ and $k_2 = 4$) from mathematical equations based exclusively on the cosine function.
2. The second family (Figure 4-2) are dual structures generated naturally by restricting the domain of the functions, a simple method is to make use of quadratic functions as a composition element, for example $z = y^2$ or $z = y^2 \cos^2 y$, are functions restricted to the domain $(-\infty, \infty)$. They are called two-phase structures because they are mainly constituted of porosity in the $(-\infty, 0)$ domain and a different one in the $(0, +\infty)$ domain, and a transition zone between them. Thus, these structures have not required a prior morphological transformation transition process as in other research work but are the intrinsic result of the nature of the domain of the functions that constitute them. Two examples of implicit equations of this type of structures is listed in Table 3. The influence of porosity on their relative density was analyzed by quantifying the relative density of the phases individually and as a whole (see Figure 5b). Each phase represents half of the total volume, and they are divided by a plane normal to the x -axis, the lower half is that of the $(-\infty, 0)$ domain, the upper half is that of the scalar field with domain $(0, +\infty)$. The combination of both phases is taken as a single relative density for the whole structure and can be calculated as the arithmetic average of the individual phases.
3. The third family (Figure 4-3) are structures with continuum orthotropic morphology (different porosity in the x , y and z axes). To achieve this, non-homonymous functions must be used, e.g., $z = y \cos x$ or $z = y \cos(x + y)$, this is to break the symmetry in the three axes. Their mechanical properties, anisotropy and fatigue compression response will be presented in subsequent sections.

Table 3. Examples of two-phase and cubic porous structures and their implicit equations and parameters.

Dual structures	$m_1[\cos^2(x) + \cos^2(y) + \cos^2(z)] -$ $m_1[x \times Q^2 \times P^2] + c_1$ $t = 1.8 \text{ mm}$	
	Model	Model
	$m_1 = 2$ $m_2 = 1$ $Q = \cos(y)$	$m_1 = 1$ $m_2 = 1$ $Q = 0.5$

	$P = \cos(x)$ $c_1 = -2$	$P = \cos(z)$ $c_1 = -1$
ubic structures	$k_1[\cos(x) \times \cos(y) + \cos(y) \times \cos(z) + \cos(z) \times \cos(x)] - k_2[\cos^2(x) \times \cos^2(y) \times \cos^2(z)] - 0.24$ $t = 1.8 \text{ mm}$	
	Model	Model
	$k_1 = 1$ $k_2 = 1$	$k_1 = 1$ $k_2 = 2$
	Model	Model
	$k_1 = 1$ $k_2 = 3$	$k_1 = 1$ $k_2 = 4$

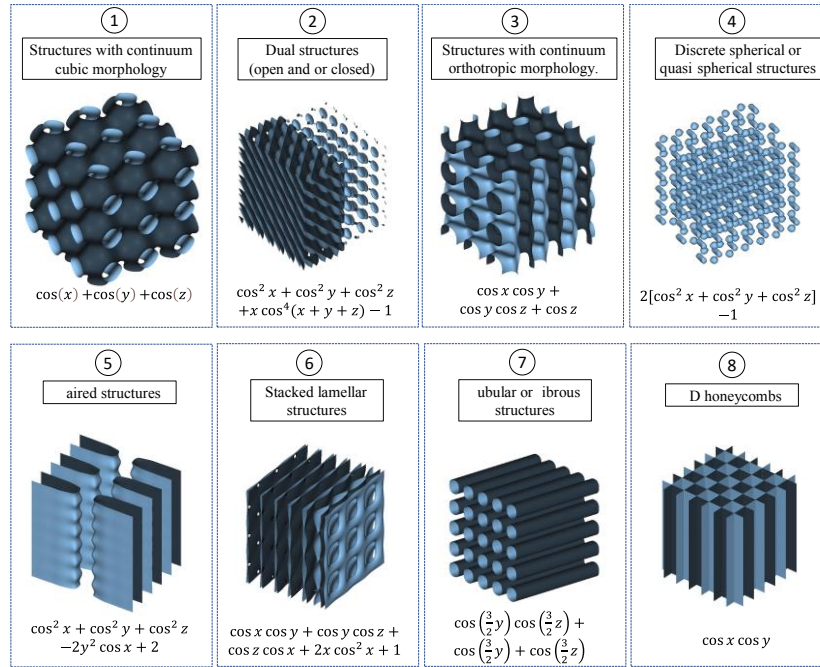


Figure 4. Classification of families of novel porous structures modeled with implicit cosine function equations.

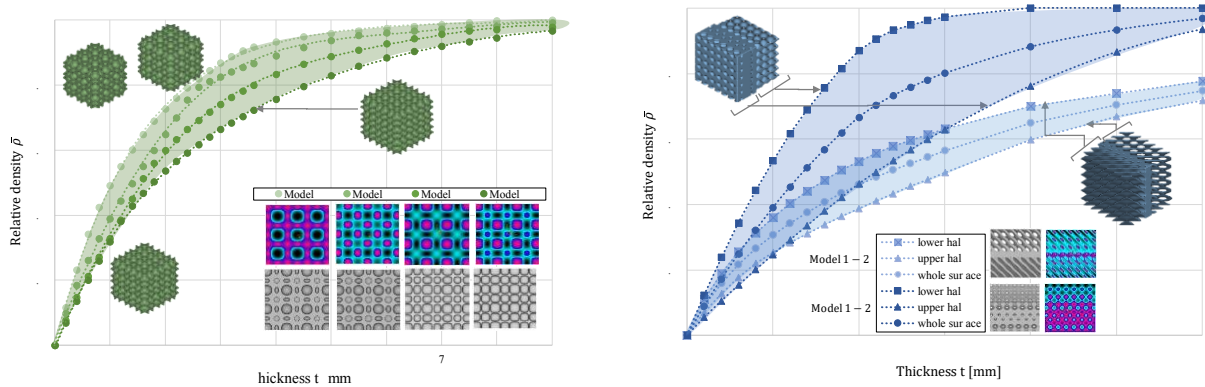


Figure 5. Relationships between thickness t and relative density $\bar{\rho}$ and shaded areas of possible values of dual porous structures (*right*) and cubic structures (*left*).

3.2. Mathematical Modeling of Orthotropic Porous Structures and Relative Density

This section presents the study thickness-relative density relationship and porosity modeling of structures with orthotropic anisotropy (different porosity in its three main planes) introduced in Section 3.1. For this purpose, in the five new models of porous structures in this section (Models: 2-1, 2-2, 2-3, 2-4, and 2-5) were changed the term $\cos(z) \times \cos(x)$ and was replaced by $\cos^2(z)$ taking as a base equation the one used in Table 3 (cubic structures), each of the equations has different amplitude coefficients of k_1 and k_2 ; The last two models (Models: 2-4 and 2-5), in addition to the term $\cos^2(z)$, the term $\cos(y) \times \cos(z)$ is replaced by another $\cos^2(z)$ (see Table 4).

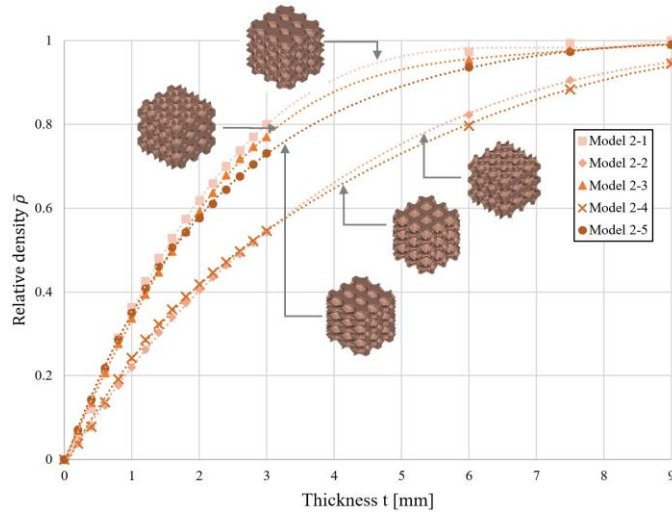


Figure 6. Relationships between thickness t and relative density $\bar{\rho}$ of porous structures with orthotropic anisotropy.

3.3. Mechanical Simulation and Apparent Elastic Linear Properties

The study of the structures of mechanical properties is focused on the analysis of the last five orthotropic structures. This section shows the morphogenesis of the anisotropy of these structures. The quantification of anisotropy of mechanical properties and representation by triaxial ellipsoidal surfaces.

3.3.1. Stiffness Scaling and Elastic Surface Variations

The variation of the minimum and maximum values of the normalized apparent elastic modulus with respect to the value of the elastic modulus of the base material of each orthotropic structure can be seen in Figure 7. Thickness ranges are between 0.6 mm and 2.4 mm for all cases. Table 5 shows the specific case of $t = 1\text{mm}$ and the calculation of the normalized shear modulus and Poisson's ratio. As can be seen, model 2-5 has auxetic values in the minimum range with $\nu^* = -0.017$.

The relationship between the thickness of the surfaces generated from the scalar fields and the relative density of the five structures are shown in the Figure 6. In this type of family, it was decided to add a fifth case study porous structure since there were 2 pairs of structures with similar relative densities (models 2-4 and 2-2 and models 2-1 and 2-3).

Table 4. Structures with orthotropic anisotropy (left) and their scalar fields of implicit equations (right) with $t = 1.8 \text{ mm}$.

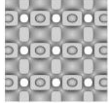
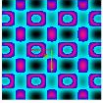
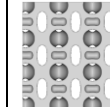
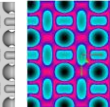
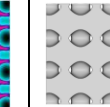
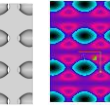
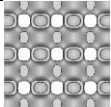
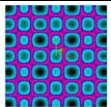
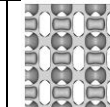
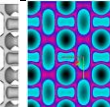
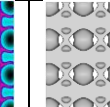
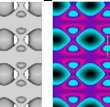
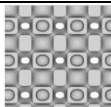
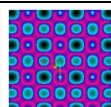
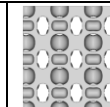
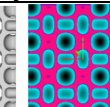
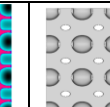
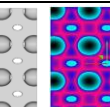
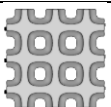
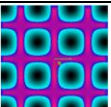
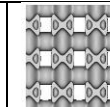
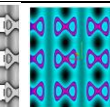
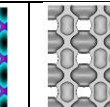
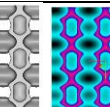
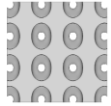
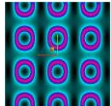
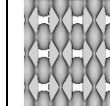
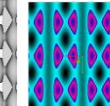
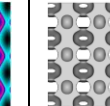
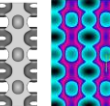
	V	[100]	V	[010]	V	[001]
Model	$1[\cos(x) \times \cos(y) + \cos(y) \times \cos(z) + \cos^2(z)] - 1[\cos(x) \cos(y) \cos(z)] - 0.24$					
						
Model	$2[\cos(x) \times \cos(y) + \cos(y) \times \cos(z) + \cos^2(z)] - 2[\cos(x) \cos(y) \cos(z)] - 0.24$					
						
Model	$1[\cos(x) \times \cos(y) + \cos(y) \times \cos(z) + \cos^2(z)] - 2[\cos(x) \cos(y) \cos(z)] - 0.24$					
						
Model	$2[\cos(x) \times \cos(y) + \cos(y) \times \cos(z) + \cos^2(z)] - 2[\cos(x) \cos^2(z)] - 0.24$					
						
Model	$1[\cos(x) \times \cos(y) + \cos(y) \times \cos(z) + \cos^2(z)] - 2[\cos(x) \cos^2(z)] - 0.24$					
						

Table 5. Maximum and minimum values of normalized apparent properties for $t = 1 \text{ mm}$. Here, anisotropy ratio of X is denoted by $A_X = X_{\max}/X_{\min}$.

	'			'			'			'		
	$\frac{E_{min}^*}{E_s}$	$\frac{E_{max}^*}{E_s}$	A_E	$\frac{K_{min}^*}{K_s}$	$\frac{K_{max}^*}{K_s}$	A_K	$\frac{G_{min}^*}{G_s}$	$\frac{G_{max}^*}{G_s}$	A_G	ν_{min}^*	ν_{max}^*	A_ν
Model	.7	.	.7	.	7.7	.7	.	.	.7	.	.	.
Model	.7	.7	.	.	.7
Model77	.	.
Model7
Model	7.	.	.	.7	.	.7	.7	.

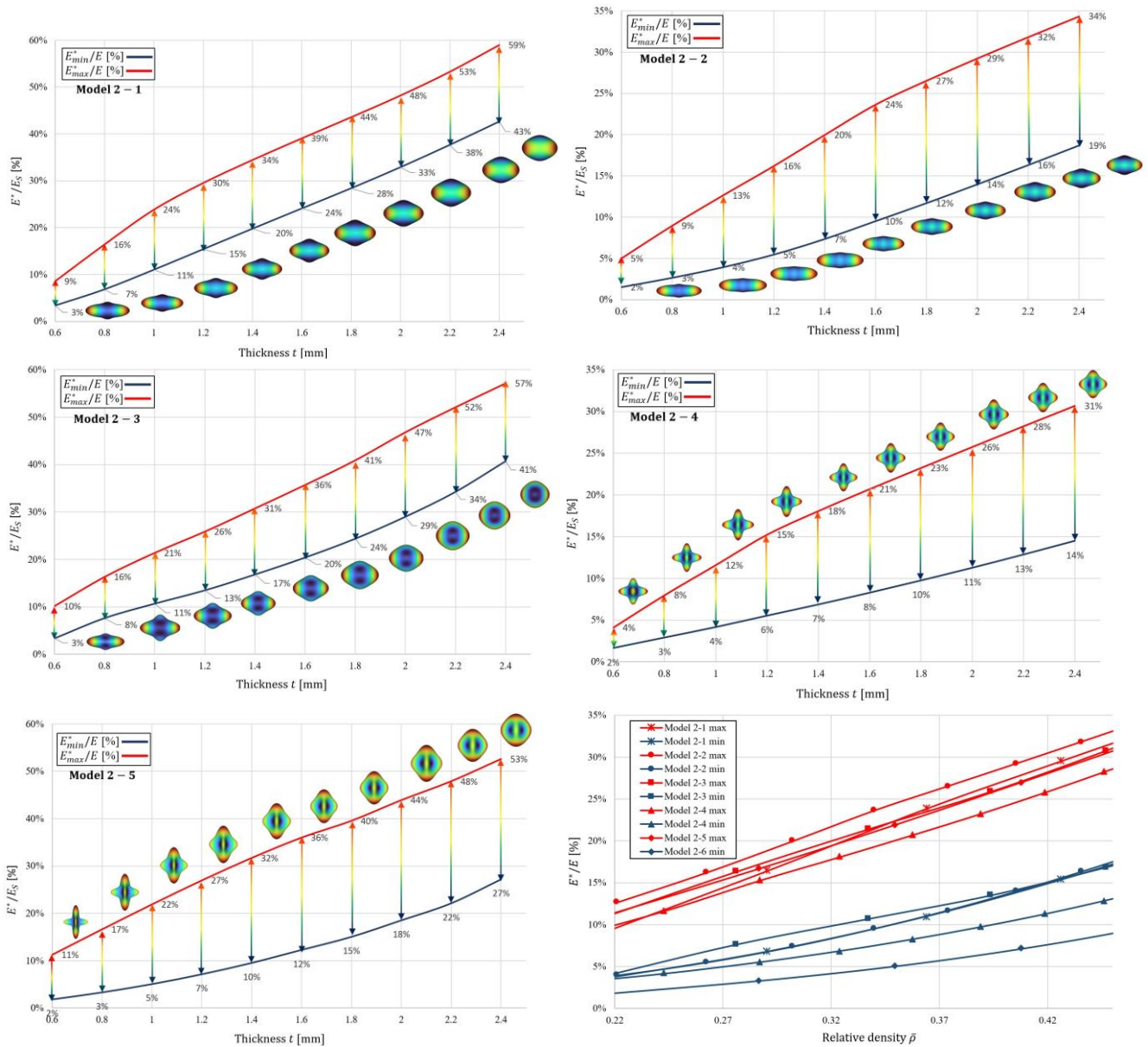


Figure 7. Evolution of the anisotropy of apparent Young's modulus lower and upper bounds value E^*/E_S and summary of apparent value of the lower and upper limits of Young's modulus E^*/E_S vs. Relative density $\bar{\rho}$.

The scaling argument of these structures was analyzed from the summary curves shown in Figure 7, where the maximum and minimum values obtained from the FEM analysis of the anisotropy of the structures is presented. Table 6 reports the coefficients n and C of the scaling law and the R^2 value of the curve fit for the data FEM considering the maximum and minimum values of apparent Young's modulus. The representations in three-dimensional space of the apparent Young's modulus and its polar projections on the principal planes shown in Figure 8 allow to correctly identify the axes on which the maximum

and minimum values are oriented. The other apparent properties and their polar projections are shown in Table 7.

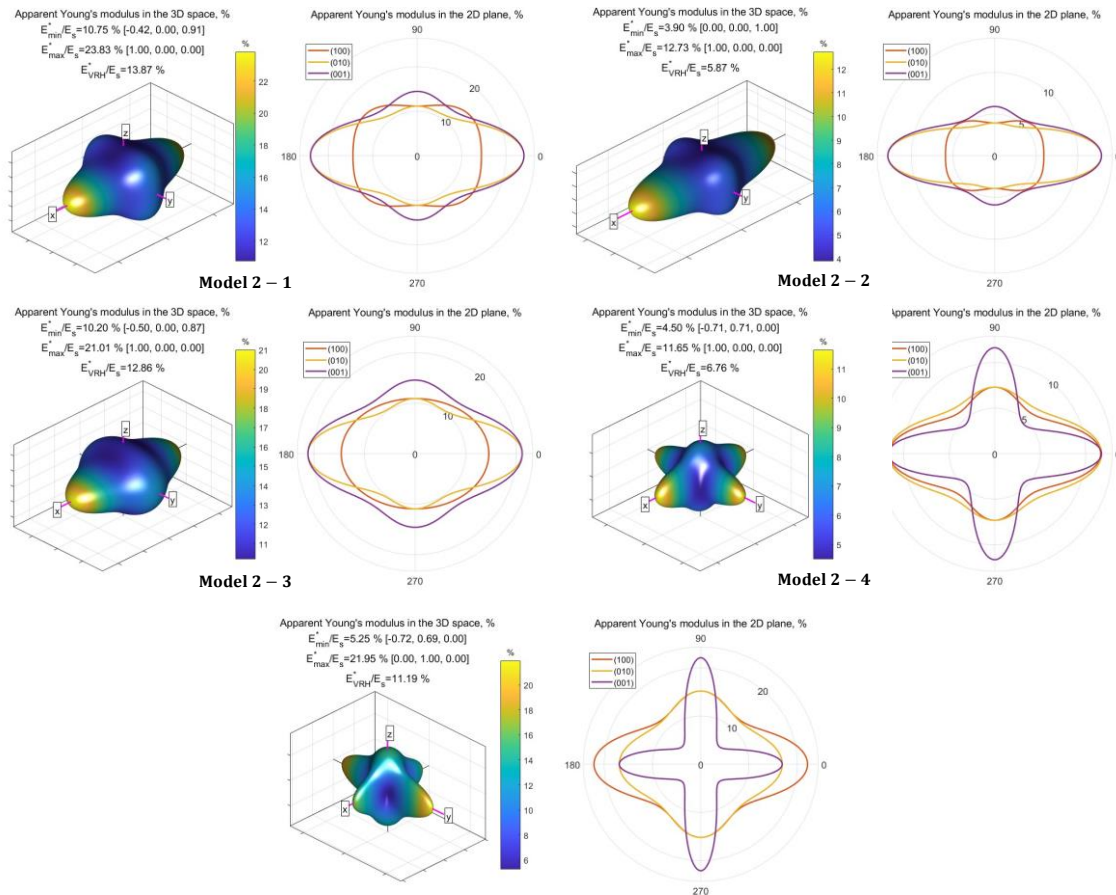
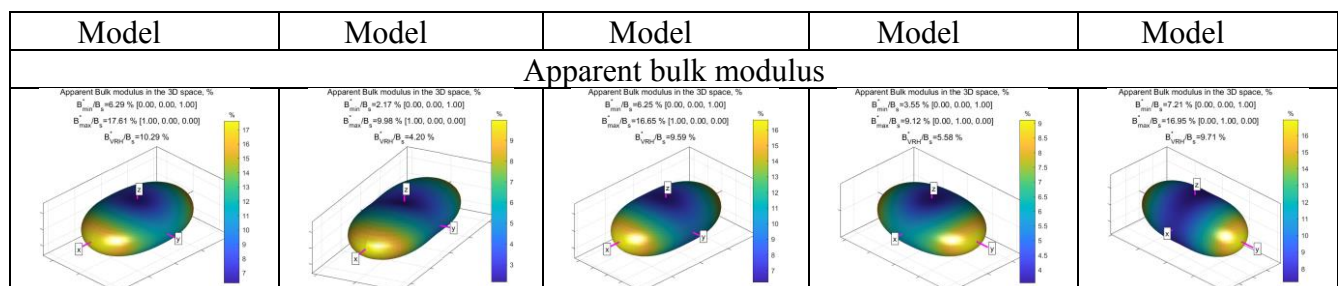


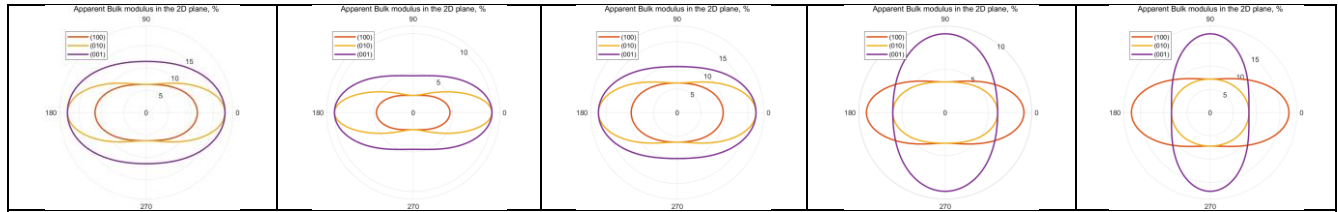
Figure 8. Apparent Young's modulus in 3D space and projections on the principal planes of porous structures with orthotropic anisotropy.

Table 6. Fit coefficients for the scaling law of orthotropic structures.

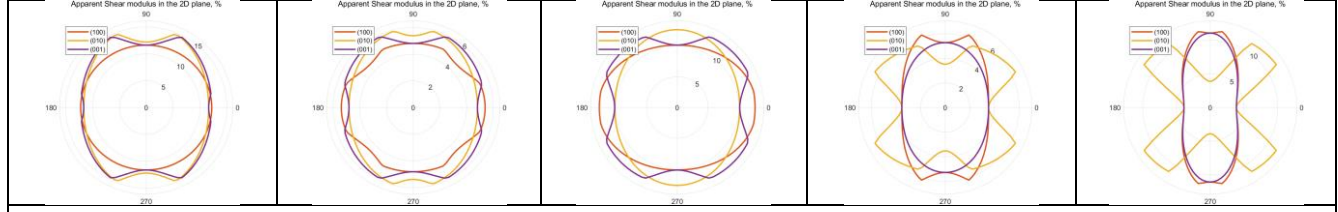
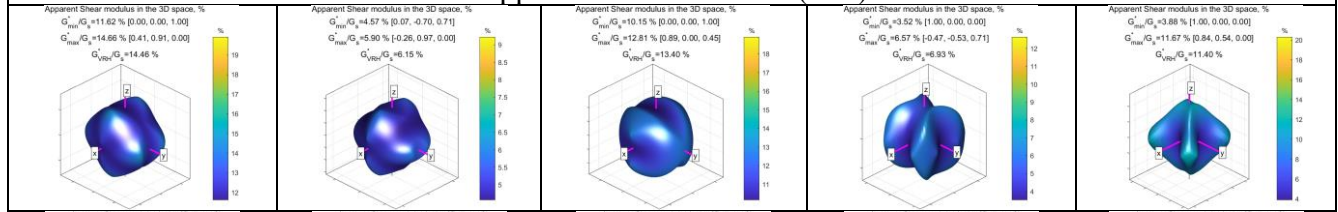
$\frac{E^*}{E_s} = C\bar{\rho}^n$	2 1		2 2		2 3		2		2 5	
	Ma	Min	Ma	Min	Ma	Min	Ma	Min	Ma	Min
n	.	.	. 7 7	.	. 7
C 7 7
 7 7	.	.

Table 7. Three-dimensional representations and polar projections of anisotropy of normalized apparent properties of orthotropic structures.

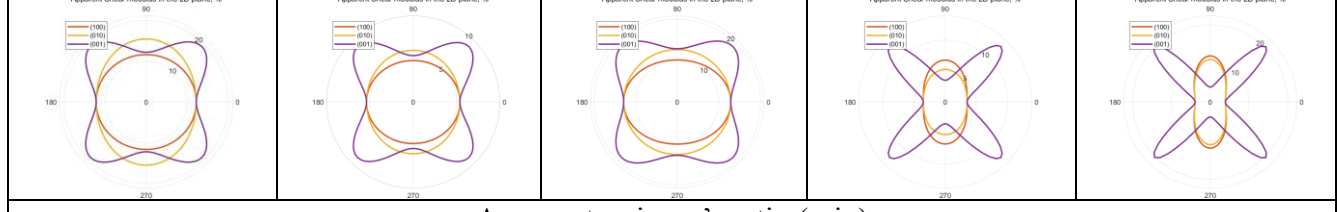
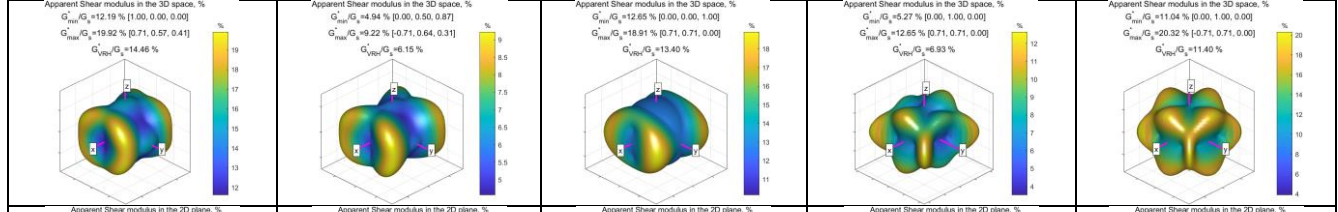




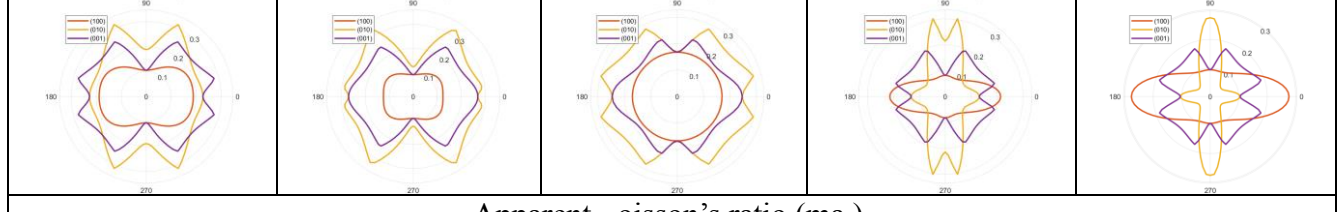
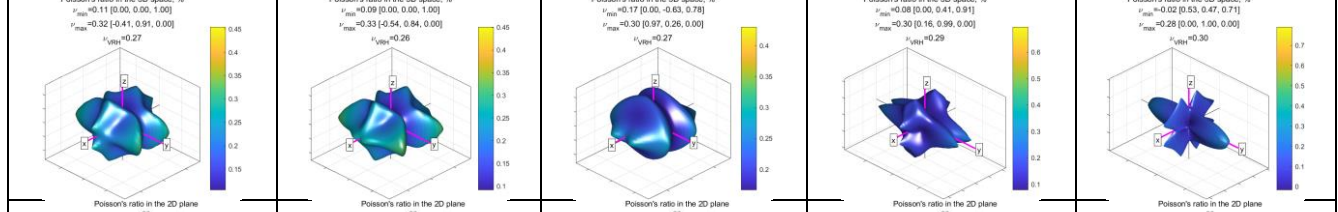
Apparent shear modulus (min)



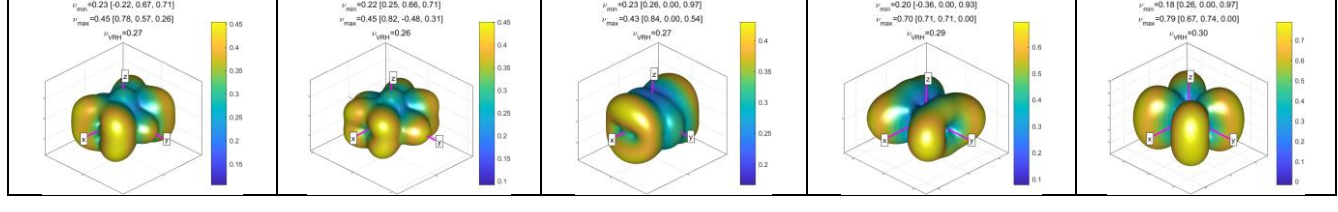
Apparent shear modulus (ma)

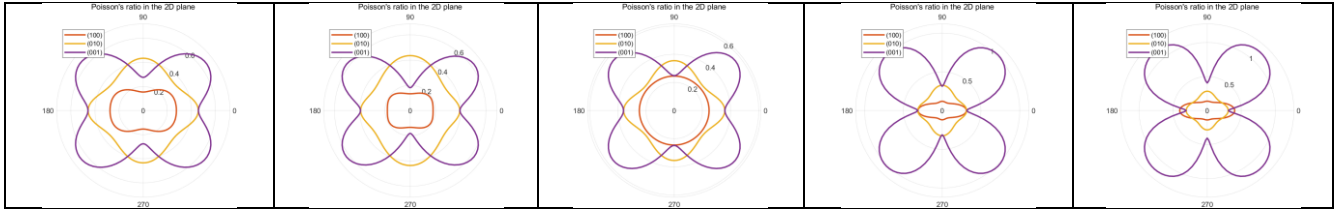


Apparent poisson's ratio (min)



Apparent poisson's ratio (ma)





3.3.2. Linear Modulus Averages

The maximum and minimum values of the stiffness properties serve only to expose their directional dependence. A more accurate representation of the anisotropy of materials is via the A^U index that uses average of the apparent elastic properties. Table 8 shows the average normalized values of the elastic properties of the porous structures.

Table 8. Average apparent properties of orthotropic porous structures using Voigt-Reuss-Hill schema.

Approach Schema	orous structure model	Average Apparent Bulk modulus $\frac{K_{\psi}^*}{K_S} [\%]$	Average Apparent Young's modulus $\frac{E_{\psi}^*}{E_S} [\%]$	Average Apparent Shear modulus $\frac{G_{\psi}^*}{G_S} [\%]$	Poisson's ratio ν_{ψ}^*
Voigt ($\psi = V$)	Model	.7	.	.7	.7
	Model	.7	.	.	.
	Model7
	Model	.7	.7	.7	.
	Model	.	.7	.	.7
Reuss ($\psi = R$)	Model7
	Model	.7	.	.7	.
	Model	.	.	.7	.7
	Model7
	Model
Hill ($\psi = VRH$)	Model	.	.7	.	.7
	Model	.7	.7	.	.
	Model7
	Model	.	.7	.	.
	Model	.7	.	.	.

3.3.3. Compression Fatigue Behavior of Porous Structures

The uniaxial compression fatigue test results for the five orthotropic porous structures based on cosine surfaces can be seen in Figure 9. The values of the applied stresses were normalized using the yield strength of base material (σ_Y). The testing was performed on each of the principal axes (x, y, z) in the orthotropic porous structures. The $S-N$ curves presented follow a scaling law nature of the form $\sigma/\sigma_Y = CN^{-n}$, with n between 0.133 to 0.314 as shown in Table 9. The behavior of porous structures is similar to the behavior of continuous materials, the rate of σ/σ_Y reduction becomes negligible near $N = 10^6$ and the slope of the $S-N$ curve becomes more or less horizontal.

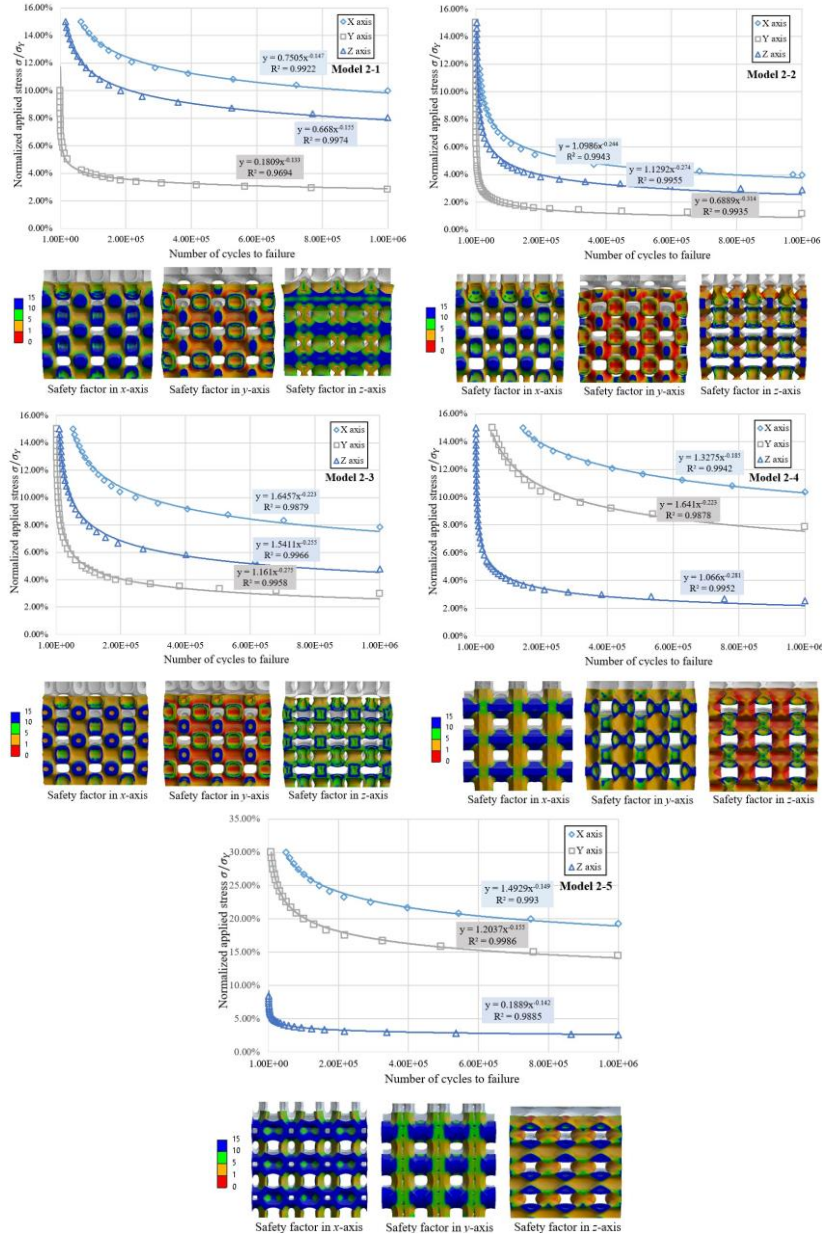


Figure 9. Normalized S-N curves of five orthotropic porous structures (*top*) and 3D colormap of fatigue safety factor for each principal axis of porous orthotropic structures (*bottom*).

Table 9. Fit coefficients for the scaling law of S-N curves of orthotropic structures.

	2 1		2 2		2 3		2		2 5		
	y	z	y	z	y	z	y	z	y	z	
n	.77	.	.7
C	.77
	.	.7	.	.	.7	.	.	.7	.	.	.

4. Analysis and Discussion of Results

This section is divided into the three main topics addressed to the new porous structures presented here: relative density, anisotropy, and fatigue studies to improve the comparison and discussion of the results. Six TPMS structures (Gyroid, Primitive, Neovius, Lidinoid, Diamond and SplitP), which were characterized in anisotropy and fatigue as part of this same research using the same methodology to avoid

systematic bias, have been selected and can be found in Appendix A. Undoubtedly, the discussion is also enriched by previous research on related results.

4.1. Relative Density and its Relation to Wall Thickness

The relative density variation of the porous structures presented in this paper are linked mainly not only to the periodicity of the implicit surface but also by the wall thickness t , this can be observed in Figure 10. From the value $t = \pi \approx 3.141$ (half of the period 2π) the thickness tends to force specific structures to increase their relative density to values $\bar{\rho} \approx 1$ abruptly. This is mainly due to the overlapping (known by other authors as *blending* [70], [71]) of the volumes of the thickened walls with increasing t , while there are other porous structures that due to the concavities of the surface curvature, the increase in thickness at values $t > \pi$ does not have great influence. Porous structures with abrupt changes in their relative density indicate that their scalar fields generate more excellent intrinsic proximity between their surfaces. The appearance of new special concavities (new pores) is another phenomenon that occurs when increasing t ; these occur around what other authors call *singular points* of the implicit equation [72], [73]. It has been studied that these points are present in TPMS structures such as the Diamond associating with the Weierstrass function [74]. The blending process and the proximity of singular points favor the increase of the cross-sectional areas of the structures and are the cause of the surface-based structures presenting elastic surface variations and that the lower and upper limits of their moduli change as the thickness increases or decreases. The difference between the maximum and minimum values of apparent Young's modulus tends to decrease with decreasing t and is also an indirect result of these phenomena.

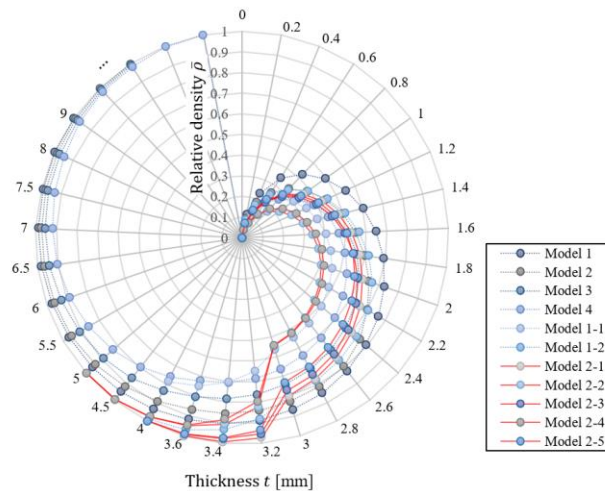


Figure 10. Comparison of the influence of thickness on relative density for $t > \pi$ values of the four families with cubic symmetry, four families with biphasic topology, and five families with orthotropic symmetry.

4.2. Apparent Properties, Scaling Laws, and Curvature Classification

According to the scaling law, the maximum and minimum values of apparent modulus of orthotropic structures have different power coefficients. For the maximum values $1.4 < n < 1.6$, while for the minimum values, this range is wider $0.8 < n < 2.5$. The n values reported for apparent Young's modulus for TPMS structures in several previous research articles range from values of $1.2 < n < 2.2$ and lower values $1 < n < 1.2$ when fabricated and experimentally characterized [75]–[77]. Many research and mathematical models show that the power-law exponent n is helpful for determining the deformation

mechanism of porous structures [78]. It has been shown that TPMS structures have a bending-dominated mechanism with n exponent values close to or greater than 2. The exception is the Primitive structure, which is cataloged closer to the stretching-dominated [76] with $n = 1.437$, especially for relative densities $\bar{\rho} < 0.1$ [79]. The Neovius structure has also been reported to have stretching-dominated behavior with $n = 1.24$ [80]. Under this same classification scheme, it is possible to affirm that the five porous structures with orthotropic symmetry presented in this work have a stretching-dominated behavior in the axis where the highest apparent Young’s modulus values were obtained. The higher efficiency under mechanical loads and high toughness of a stretching-dominated structure compared to bending-dominated structures are more attractive for lightweight structural applications because stretching-dominated porous structures are more weight-efficient [81]. For example, due to axial loads, a stretch-dominated structure is expected to be about $10\times$ as stiff and about $3\times$ as strong as a bending-dominated structure [82].

Although other authors have attributed bending- and stretching- dominated behavior to the double curvature morphology of some TPMS structures [83] it has only recently been corroborated in-depth that the Gyroid structure distributes its mechanical stresses in spiral domains along its structure [84]. The fact is that Gyroid’s double curvature generates two continuous concentric spirals or helices (one external and one internal) parallel to the direction of application of the load on their surfaces with zero Gaussian curvature. On the other hand, the Primitive structure generates mainly hoop-shaped stress concentrations around its concavities with positive Gaussian curvature. This introductory statement lies the main difference between the two deformation mechanisms in porous structures [85], [86]. The five new porous orthotropic structures studied show previously unreported cross-ladder stress distributions representing a rigid framework that satisfies Maxwell’s stability criterion for 3D structures with a stretching-dominated mechanism [82] (see Figure 11). This contribution opens up understanding and insight for future studies of fatigue and deformation mechanisms for curvature-based porous structures and the strengthening of critical areas susceptible to failure.

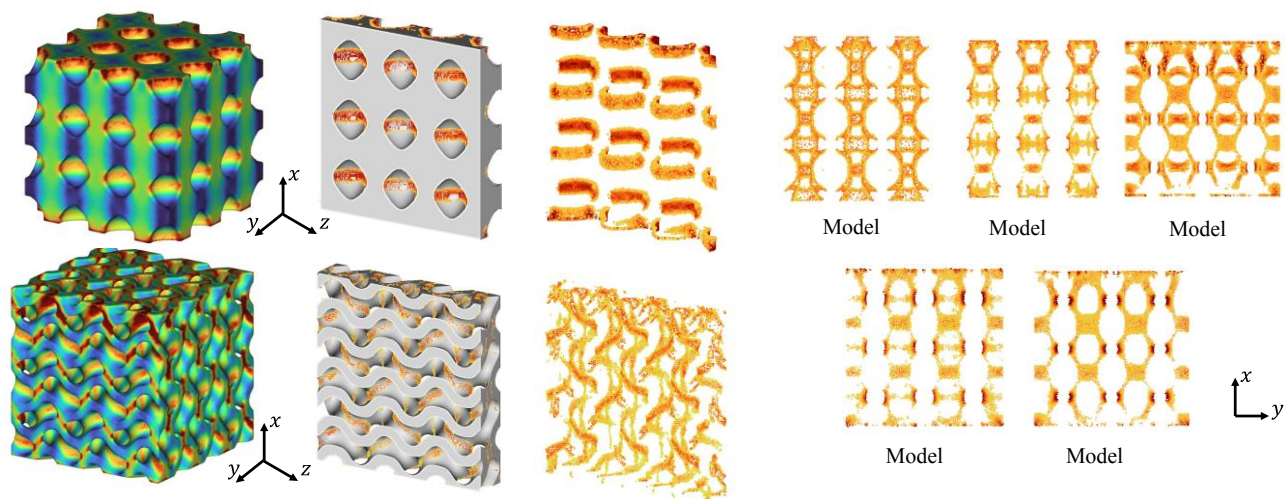


Figure 11. Von Mises stress distributions in FE compression fatigue simulations: (a) Primitive, (b) Gyroid, and (c) novel orthotropic porous structures. Regions of high red saturation indicate regions prone to crack initiation and fatigue disconnection.

Differential geometry of curves provides an alternative way to quantify and compare both the on-surface geometric shape descriptors versus mechanical performance from stress distributions data. TPMS are oriented surfaces immersed in \mathbb{R}^3 that have constant zero mean curvature $\mathcal{H} = 0$ and negative or vanishing Gaussian curvature $\mathcal{K} \leq 0$; Hence, TPMS are saddle-dominated surface based on their shape

index estimation (see Figure 12a), except at some single points where the surface is locally flat surface $\mathcal{K} = 0$. According to [87], Gyroid and Diamond exhibited the more uniform distribution of the negative Gaussian curvature, while Neovius very localized curvature regions. Figure 12b-f shows the curvature monotonic probability distribution of our different porous structures as well as the dominated stress bimodal distribution obtained from the fatigue test at the time of mechanical failure. It can be seen that the surface curvatures are distributed similarly among the different structures, all with a general tendency concentration of mean curvature shift $\mathcal{H} \in (0, -0.1)$, the lower stress range has a tendency to have a positive mean curvature range $\mathcal{H} \in (0, +0.3)$.

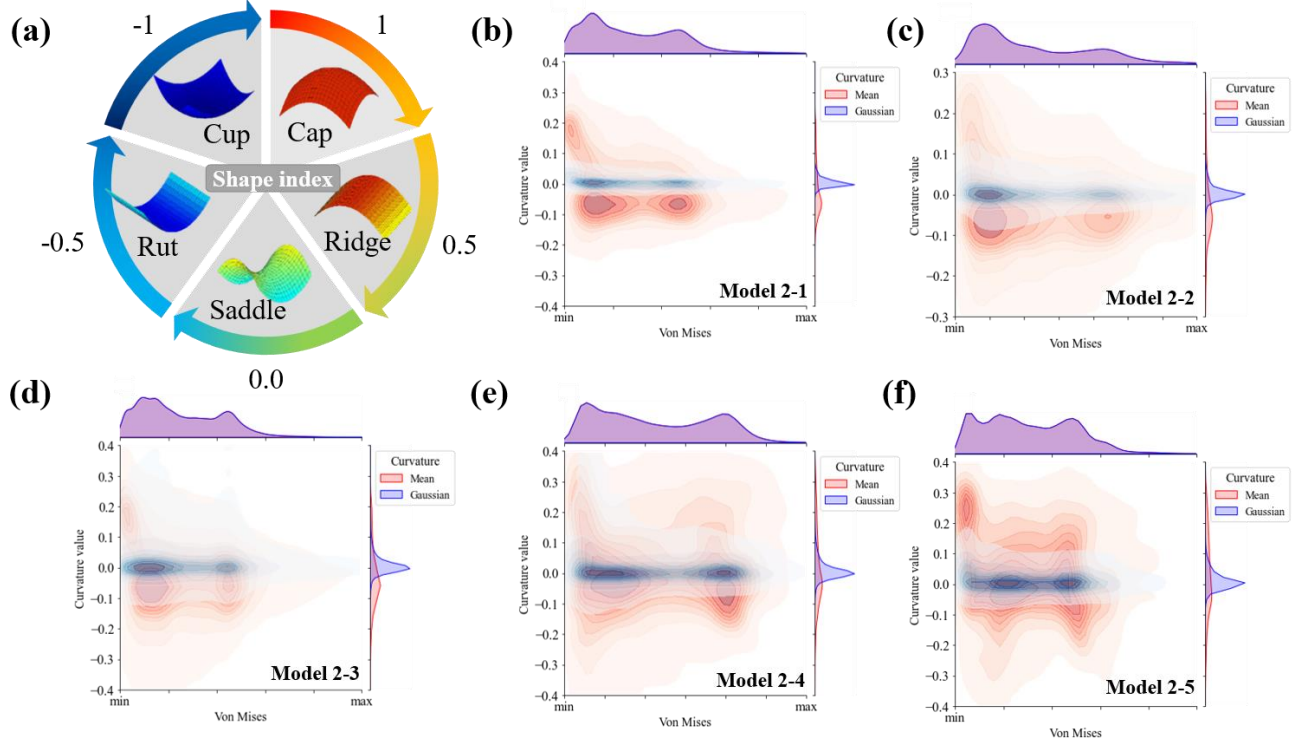


Figure 12. (a) Five common surface type defined by shape index scales; (b-f) Normalized Gaussian (K) and mean (H) curvatures and their respective probability functions versus stress distribution, the color map represents the kernel density levels of measurements distribution datasets.

We found that all structures are dominated by zero Gaussian curvature patches $\mathcal{K} = 0$ and vanishing mean curvature $\mathcal{H} \leq 0$, so our structures are ridge-shaped porous structures with shape index into 0.45 to 0.51. It is worth mentioning the influence of surface curvature beyond structural mechanical applications, the specific curvature characteristic is part of the reason why surface-based structures have attracted interest as templates for tissue engineering scaffolds, since surface curvature is known to control the spatiotemporal cell and tissue organization [88].

4.3. Anisotropy of Porous Media

The comparison of the average elastic moduli (E , G , and K) between TPMS and cosine-based porous structures is shown in Figure 13. According to Equation B.10, values close to 1 of the G_V^*/G_R^* and K_V^*/K_R^* ratios contribute to lower anisotropy. As can be seen, TPMS structures such as Neovius and Primitive tend to be more anisotropic structures due to their ratios $G_V^*/G_R^* > 1$, the same is true for models 2-4 and 2-5 of the orthotropic porous structures.

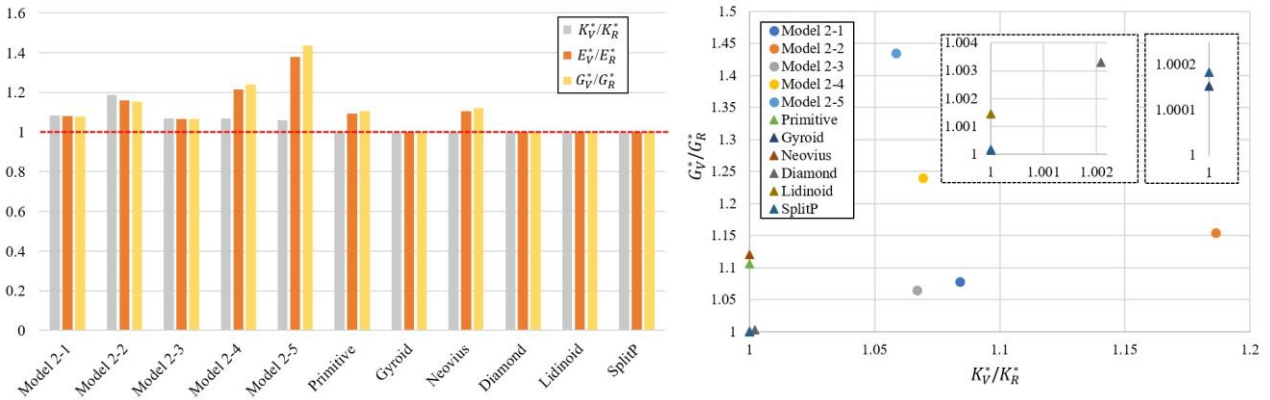


Figure 13. (a) Comparison of the ratios of average elastic moduli of structures with cubic (TPMS) and orthotropic symmetry (cosine surface-based porous structure); (b) Ratios with values close to 1 contribute less to anisotropy.

Models 2-2 and 2-4 show the lowest averages apparent stiffness (\bar{E}_{VRH}/E_S), rigidity (\bar{G}_{VRH}/G_S), and the compressibility (\bar{K}_{VRH}/K_S) with percentages very close to the TPMS structure of Neovius, taking the Voigt-Reuss-Hill schema as a reference. Models 2-1 and 2-3 present percentage ranges of the normalized apparent elastic moduli that exceed Gyroid and Neovius as can be observed in Figure 14. These same models (models 2-1 and 2-3) show better levels of anisotropy with $A^U=0.394$ and 0.478 values than the Neovius and Primitive structures with $A^U=0.529$ and 0.604 values as shown in Figure 14. The Voigt-Reuss-Hill approximation has been used previously to calculate the anisotropy of Gyroid, Primitive, and Diamond manufactured at the nanoscale, and the statement that Gyroid has low anisotropy is consistent with other research work. [89]. Using the Zener index A^Z , other studies agree that Neovius and Primitive structures tend to have higher anisotropy [77], [90], and it is these same structures that have stretching-dominated behavior with greater anisotropy of the shear modulus acting on during the axial loads of their surfaces. Although intuitively, a structure with cubic symmetry should have better mechanical anisotropy with respect to one with orthotropic symmetry, this is only true if there is complete dependence between the elastic constants [91]. However, materials with orthotropic and cubic symmetry have nine and three independent elastic coefficients, respectively. For example, the shear modulus and elastic modulus can be tunable in the same material independently, thus maximizing stiffness and strength [92].

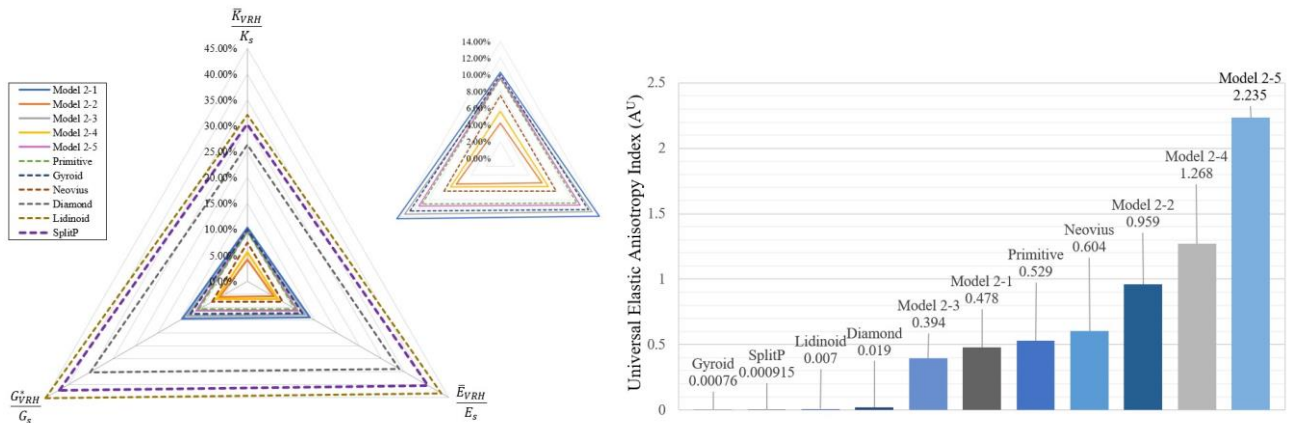


Figure 14. (a) Comparison of average normalized elastic moduli according to the Voigt-Reuss-Hill schema; (b) Comparison of A^U index of structures with cubic symmetry (TPMS) and with orthotropic symmetry (cosine surface-based porous structure).

4.4. Fatigue Properties of Porous Structures

The uniaxial compressive fatigue life estimation results indicate that five of the six TPMS structures exceed the range of one million cycles ($N > 10^6$) with normalized stress values around the range of 1-3 % approximately as can be seen in Figure 15a. On the other hand, all the analyzed porous orthotropic structures exceed that range for the same cyclic fatigue test in at least two of their principal axes, while the third axis shows similar values to the TPMS structures, and in some cases, it is higher. The results show that all the orthotropic porous structures obtained higher results for the x -axis, this axis is the one that allowed breaking the cubic symmetry and transforming the structures to orthotropic symmetry using the $\cos^2 x$ term in their implicit equations, as can be seen in Table 4. It is also important to remember that this is congruent with the results shown in Figure 8 where it can be observed that the axis where the highest value of Young's apparent modulus is located is the x -axis for four of the five orthotropic porous structures, except for model 2-5 whose maximum apparent Young's modulus is located in the y -axis.

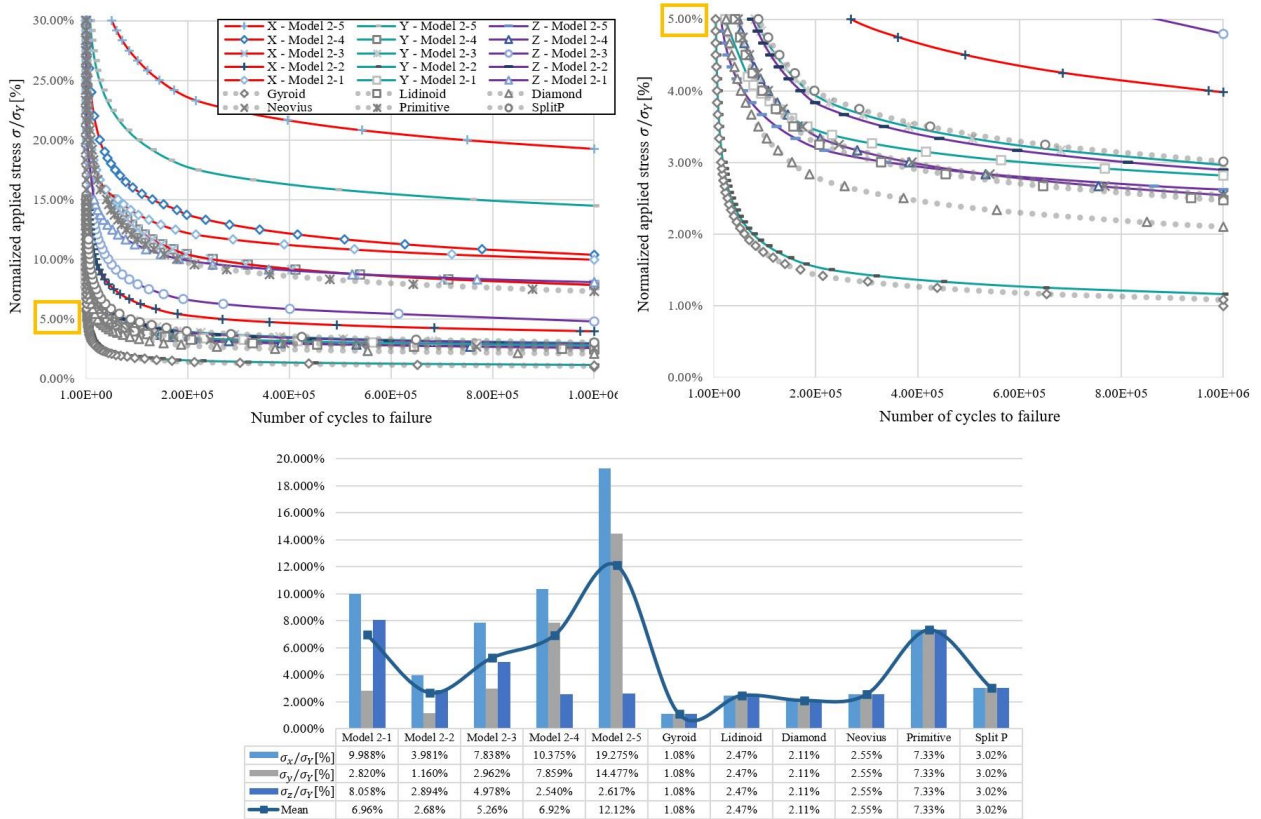


Figure 15. (a) Normalized S-N curves of orthotropic structures and TPMS structures: with normalized applied stress at 30% and 5%; **(b)** Histogram of normalized and mean stress values of TPMS structures and orthotropic structures for which $SF=1$.

Figure 15b shows a comparison of the normalized stresses for which safety factor values equal to one ($N=1$) are obtained, i.e., above these normalized stress values, the safety value decreases and vice versa. In the case of TPMS structures, the SF values in the 3 main axes are identical due to cubic symmetry, and in the case of porous structures, the stress value for each axis is different. The TPMS structure less resistant to fatigue is the Gyroid with normalized stress of 1.08%, and the one with the highest resistance is the Primitive with normalized stress of 7.33%, the rest of the structures are around the value of 3%. On the other hand, the orthotropic structures have better fatigue results, the structure of model 2-5

achieves values higher than 14% for the x -, y -axes, and for the z -axis, a value of 2.6% is obtained. The scaling law of S - N curves it is usually more helpful to choose to compare the C term since by its logarithmic nature this value indicates the stress supported when reaching a $SF=1$ or entering the infinite life zone ($N > 10^6 \sim 10^7$) and the higher the C term, the higher the SF of the structure.

Models 2-5, 2-1 are the structures with the best fatigue results and coincide with the fact that they are the structures with the highest apparent Young's modulus. In addition, it is important to mention that although the structure of model 2-5 is the one with the highest anisotropy index A^U , it is the one that manages to duplicate the fatigue resistance performance of the Primitive structure, which is the one that obtained the best results of the TPMS group. Primitive's good fatigue results coincide with other research where low-stress values have been reported with respect to other TPMS structures such as Gyroid or Neovius [76]. Although there is scarce literature on the in-depth study of compressive fatigue of TPMS structures [93], the conclusion that the Gyroid structure has the lowest anisotropy but is not necessarily the most fatigue resistant has been corroborated in this study.

The researchers agree that the observed stretch-dominated structures tend to fail layer by layer with sequential local collapse at the stress plateau [94] and that structures attribute fatigue failure to the accumulation of stress in the weakest cross-section [95]. It has been observed that for the same level of applied load, it can withstand higher cycles before failure generally increases as the relative density increases [96]. The stress distribution of the orthotropic porous structures has a crisscrossed staircase distribution. Together with the fact that they have higher apparent shear stresses (although this affects their anisotropy), they increase their fatigue capacity. The coincidence that these orthotropic structures have a similarly dominated stretching to the Primitive structure indicates a concordance with the latter structure having the best fatigue performance of the TPMS structures studied in this research.

5. Conclusions

In this paper, the development of new porous structures from cosine surfaces using implicit equations in \mathbb{R}^3 , the essential concept of their characterization and the influence of mathematical parameters such as periodicity or amplitude coefficients have been investigated. The mathematical approach makes it possible to generate different families with different properties from the same base equation. The modeling approach presented here leads to exploring numerous programmable, fast, efficient, and simple modeling possibilities. Furthermore, these structures open the panorama to research new porous structures based on surfaces where the known optimization techniques, morphology gradients, and surface conforming can be applied. In addition, their apparent elastic properties were analyzed from the components of the apparent stiffness tensor to quantify the elastic anisotropy compared to six typical TPMS structures. Both the average values of the elastic moduli and the homogenization estimates.

The main remarks and outcomes of this manuscripts are:

1. The stress distribution of the five orthotropic porous structures studied has a "criss-cross staircase" distribution, and they also have higher apparent shear moduli (although this affects their anisotropy) than the TPMS structures. However, both phenomena improve their compressive fatigue behavior of the orthotropic structures, suggesting a better performance than the TPMS structures as it can see in the S - N curves.
2. Based on the applicability of the A^U index, two porous structures with orthotropic topology (models 2-1 and 2-3) are reported to have lower anisotropy than two well-known cubic TPMS structures, namely Neovius and Primitive. This is due not to the elastic modulus E , but to variations in the moduli K and G . The individual study of these moduli provides insight into the

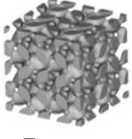

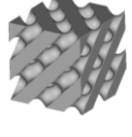
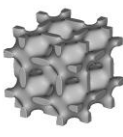

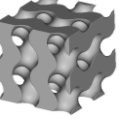
stiffness, rigidity and compressibility of the structures and their contribution to the overall anisotropy.

3. The thickening of the level surfaces and the proximity of the singular points promotes the increase of the cross-sectional areas of the anisotropic structures which causes the variations of the lower and upper limits of their elastic moduli. Although at higher apparent density the overall anisotropy is improved, the gap between the maximum and minimum values of the elastic modulus may increase.
4. We bring together in a single manuscript the computational implicit modeling based on the principle of leveled surfaces together with periodic modeling using cosine functions to show that the scalar field of Fourier series theory allows the generation of different structural porous morphologies beyond those described in some previous works, Furthermore, it is shown that the study of the apparent mechanical properties of porous structures derived from these morphologies can be studied by means of the A^u index in a more flexible way regardless of the symmetry class, by means of computational homogenization and different averaging schemes via stiffness tensor.

Appendix A The Elastic Anisotropy for Cubic and Orthotropic Structures

Although not all TPMS structures have cubic symmetry, the best-known ones do. Table A.1 lists the six structures taken as a reference to compare the results obtained in this paper.

Table A.1 Common examples of previously proposed triply periodic minimum surfaces (TPMS) structures and their corresponding implicit equations.

	q		q
idi noid  7 ,	$U_L = \sin(2x) \cos(y) \sin(z) + \sin(2y) \cos(z) \sin(x) + \sin(2z) \cos(x) \sin(y) - \cos(2x) \cos(2y) - \cos(2y) \cos(2z) - \cos(2z) \cos(2x) + 0.3$	Split S  ,	$U_{SP} = 1.1[\sin(2x) \cos(y) \sin(z) + \sin(2y) \cos(z) \sin(x) + \sin(2z) \cos(x) \sin(y)] - 0.2 [\cos(2x) \cos(2y) + \cos(2y) \cos(2z) + \cos(2z) \cos(2x)] - 0.4[\cos(2x) + \cos(2y) + \cos(2z)]$
Diamond D  ,	$U_D = \sin(x) \sin(y) \sin(z) + \sin(x) \cos(y) \cos(z) + \cos(x) \sin(y) \cos(z) + \cos(x) \cos(y) \sin(z)$	e ovius  ,	$U_N = 3[\cos(x) + \cos(y) + \cos(z)] + 4\cos(x) \cos(y) \cos(z)$
rimitive  7 , ,	$U_P = \cos(x) + \cos(y) + \cos(z)$	Gyroid G  ,	$U_G = \cos(x) \sin(y) + \cos(y) \sin(x) + \cos(x) \sin(y)$

For linear elastic deformation, the generalized form of Hooke's law can be written as:

$$\varepsilon_{ij} = \mathbb{S}_{ijkl} \sigma_{kl} \quad \text{Equation A.}$$

Or,

$$\sigma_{ij} = \mathbb{C}_{ijkl} \varepsilon_{kl} \quad \text{Equation A.}$$

where ε and σ are the second-rank tensors of strain and stress, respectively, where the indices i and j ($= 1, 2, 3$) relate to a standard Cartesian reference frame ($x = 1, y = 2, z = 3$). The elastic compliance \mathbb{S} or stiffness \mathbb{C} of material can therefore be represented in a more compact form, known as the Voigt matrix. This is a square 6×6 matrix, for example, an orthotropic solid has three mutually orthogonal symmetry planes.

The 6×6 matrix of the apparent stiffness tensor \mathbb{C}_{ij}^* is obtained from the homogenization process compute using nTopology®. The normalization (Ψ^*/Ψ_S) of the apparent property Ψ^* with respect to the base material properties Ψ_S (bulk modulus, Young's modulus, shear modulus, and Poisson's ratio) was also implemented. The maximum and minimum bounds values for TPMS structures are listed in Table A.2 and the three averaging schemes of Voigt, Reuss, and Hill are obtained, see Table A.3. Three-dimensional representations and polar orthogonal projections of the apparent properties are presented in Table A.4.

Table A.2 Minimum and maximum values as well as anisotropy of apparent Young's modulus, shear modulus, bulk modulus and Poisson's ratio for the six TPMS structures studied. Here, anisotropy ratio of X is denoted by $A_X = X_{\max}/X_{\min}$.

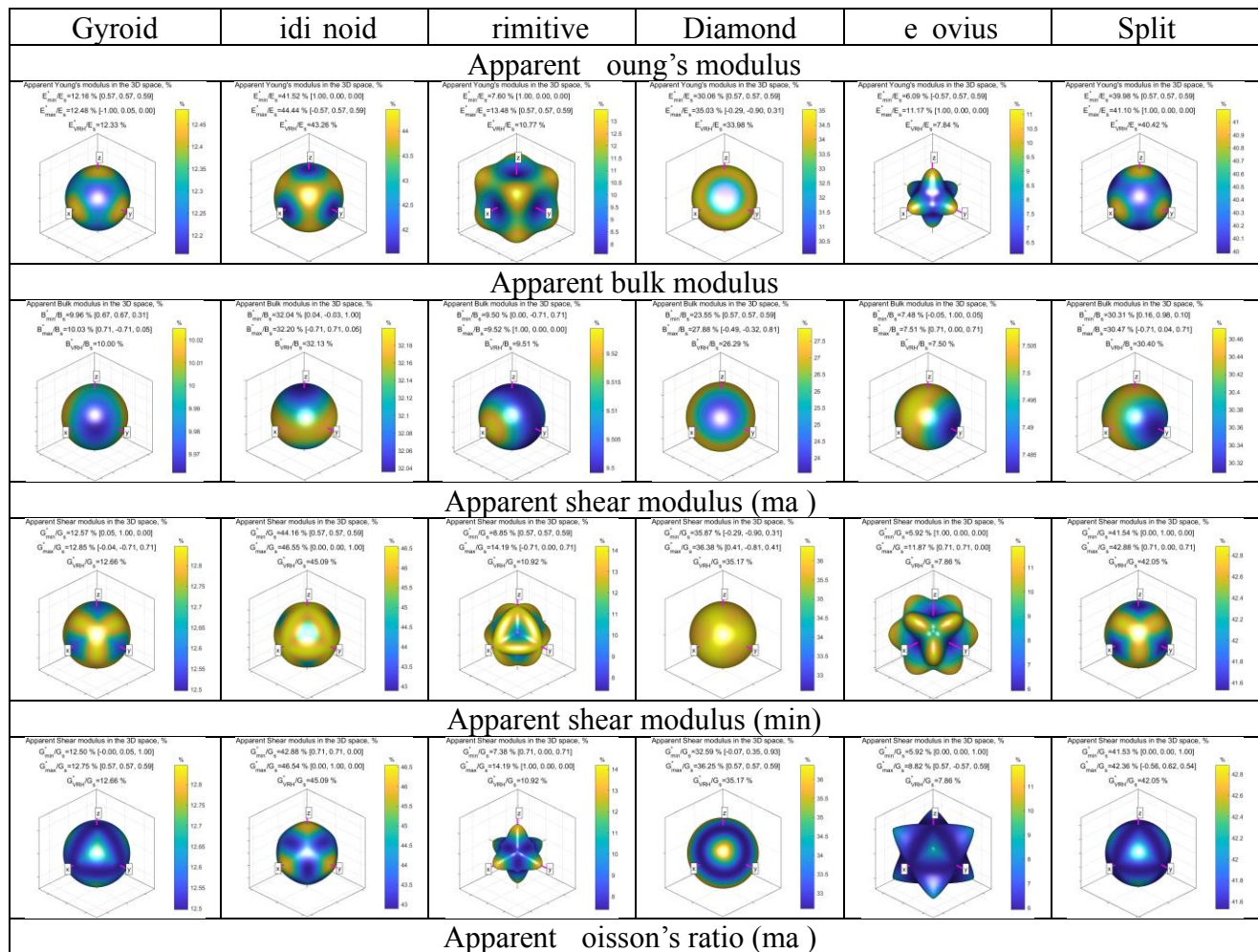
	Young's Modulus			Bulk Modulus			Shear Modulus			Poisson's Ratio		
	E^*/E	E_x^*/E	A_E	K_x^*/K	K^*/K	A_K	G^*/G	G_x^*/G	A_G	ν^*	ν_x^*	A_ν
Gyroid	.7	.7	.7	.7	.7	.7	.7	.7	.7	.7	.7	.7
Indinoid	.7	.7	.7	.7	.7	.7	.7	.7	.7	.7	.7	.7
Primitive	.7	.7	.77	.7	.7	.7	.7	.7	.7	.7	.7	.7
Diamond	.7	.7	.7	.77	.7	.7	.7	.77	.7	.7	.7	.7
Cubic	.7	.7	.7	.7	.7	.7	.7	.7	.7	.7	.7	.7
Split	.7	.7	.7	.7	.7	.7	.7	.7	.7	.7	.7	.7

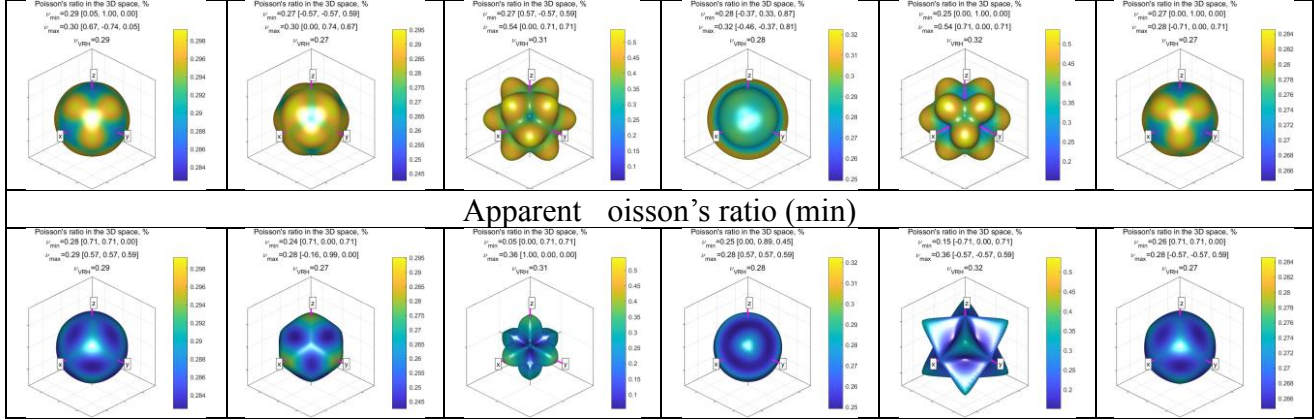
Table A.3 Average apparent elastic properties of six TPMS structures with thickness $t = 1$ mm using Voigt-Reuss-Hill schema.

Approach Schema	MS	Average apparent bulk modulus $\frac{B_\psi^*}{B_S}$ [%]	Average apparent Young's modulus $\frac{E_\psi^*}{E_S}$ [%]	Average apparent shear modulus $\frac{G_\psi^*}{G_S}$ [%]	Average apparent Poisson's ratio ν_ψ^*
Voigt ($\psi = V$)	Gyroid	.7	.7	.7	.7
	Indinoid	.7	.7	.7	.7

	rimitive	.	.	.7	.
	Diamond
	e ovius	7.	.	.	.
	Split	.	.7	.	.7
euss ($\psi = R$)	Gyroid	.	.7	.	.
	idi noid7
	rimitive	.	.	.7	.
	Diamond	.7	.	.	.
ill ($\psi = VRH$)	e ovius	7.	7.	7.	.
	Split7
	Gyroid
	idi noid7
	rimitive	.	.77	.	.7
	Diamond	.	.	.7	.
	e ovius	7.	7.	7.	.
	Split7

Table A.4 Three-dimensional representations of anisotropy of normalized apparent properties of TPMS structures.





An orthotropic solid has 9 independent elastic constants. The generalized Hooke's law that relates the stresses to strains for orthotropic (orthorhombic class) material can be written using Voigt's notation as:

$$\begin{bmatrix} \sigma_{11} \\ \sigma_{22} \\ \sigma_{33} \\ \tau_{23} \\ \tau_{31} \\ \tau_{12} \end{bmatrix} = \begin{bmatrix} C_{11} & C_{12} & C_{13} & 0 & 0 & 0 \\ C_{12} & C_{22} & C_{23} & 0 & 0 & 0 \\ C_{13} & C_{23} & C_{33} & 0 & 0 & 0 \\ 0 & 0 & 0 & C_{44} & 0 & 0 \\ 0 & 0 & 0 & 0 & C_{55} & 0 \\ 0 & 0 & 0 & 0 & 0 & C_{66} \end{bmatrix} \begin{bmatrix} \epsilon_{11} \\ \epsilon_{22} \\ \epsilon_{33} \\ \gamma_{23} \\ \gamma_{31} \\ \gamma_{12} \end{bmatrix} \quad \text{Equation A.}$$

The generic mechanical stability conditions (Born-Huang criteria) for orthorhombic class are:

$$\begin{aligned} C_{11} > 0, C_{11}C_{12} > C_{12}^2, \\ C_{44} > 0, C_{55} > 0, C_{66} > 0, \\ C_{11}C_{22}C_{33} + 2C_{12}C_{13}C_{23} - C_{11}C_{23}^2 - C_{22}C_{13}^2 - C_{33}C_{12}^2 > 0 \end{aligned} \quad \text{Equation A.}$$

Cubic systems have only three independent elastic constants,

$$\begin{bmatrix} \sigma_{11} \\ \sigma_{22} \\ \sigma_{33} \\ \tau_{23} \\ \tau_{31} \\ \tau_{12} \end{bmatrix} = \begin{bmatrix} C_{11} & C_{12} & C_{12} & 0 & 0 & 0 \\ C_{12} & C_{11} & C_{12} & 0 & 0 & 0 \\ C_{12} & C_{12} & C_{11} & 0 & 0 & 0 \\ 0 & 0 & 0 & C_{44} & 0 & 0 \\ 0 & 0 & 0 & 0 & C_{44} & 0 \\ 0 & 0 & 0 & 0 & 0 & C_{44} \end{bmatrix} \begin{bmatrix} \epsilon_{11} \\ \epsilon_{22} \\ \epsilon_{33} \\ \gamma_{23} \\ \gamma_{31} \\ \gamma_{12} \end{bmatrix} \quad \text{Equation A.}$$

The mechanical stability conditions for cubic anisotropy are:

$$C_{11} - C_{12} > 0, C_{11} + 2C_{12} > 0 \text{ and } C_{44} > 0 \quad \text{Equation A.}$$

Appendix B Anisotropy Indexes

Many indexes have been proposed to quantify the degree of anisotropy. The Zener anisotropy index (A^Z) is used for structure with cubic symmetry and is defined as:

$$A^Z = \frac{2C_{44}}{C_{11} - C_{12}} \quad \text{Equation .}$$

where C_{44} , C_{11} , C_{12} are three independent elastic constants. This index is only applied to the cubic structure and neglects the contribution of the bulk part of the stiffness tensor. Two useful ‘averaging’ approximations that can be applied to the complete set of anisotropic elastic properties are those due to Reuss and Voigt. The bulk and shear moduli in the Voigt scheme (upper bound) are defined as:

$$K_V = [(C_{11} + C_{22} + C_{33}) + 2(C_{12} + C_{23} + C_{31})]/9 \quad \text{Equation .}$$

$$G_V = [(C_{11} + C_{22} + C_{33}) - (C_{12} + C_{23} + C_{31}) + 3(C_{44} + C_{55} + C_{66})]/15 \quad \text{Equation .}$$

and the Reuss schema (lower bound) as:

$$K_R = 1/[(S_{11} + S_{22} + S_{33}) + 2(C_{12} + C_{23} + C_{31})] \quad \text{Equation .}$$

$$G_R = 15/[4(S_{11} + S_{22} + S_{33}) - 4(S_{12} + S_{23} + S_{31}) + 3(S_{44} + S_{55} + S_{66})] \quad \text{Equation .}$$

The Voigt-Reuss-Hill (VRH) average of a property is defined as the arithmetic mean of the Voigt and Reuss bounds:

$$G_{VRH} = (G_V + G_R)/2 \quad \text{Equation .}$$

$$K_{VRH} = (K_V + K_R)/2 \quad \text{Equation . 7}$$

From C_{ij} , bulk (K) and shear (G) moduli, one can estimate various other material-specific parameters. The elastic modulus (E) and Poisson’s ratio (ν) can be expressed as follows:

$$E = \frac{9KG}{3K + G} \quad \text{Equation .}$$

$$\nu = \frac{3K - 2G}{2(3K + G)} = \frac{3K - E}{6K} \quad \text{Equation .}$$

To plot the variations of disparate elastic properties across topologies with widely different symmetries and anisotropies, we use the Universal Anisotropy Index (A^U) proposed by Ranganathan et al, [107], defined as:

$$A^U = 5 \frac{G_V}{G_R} + \frac{K_V}{K_R} \geq 0 \quad \text{Equation .}$$

where G_V and K_V are the Voigt average shear and bulk moduli, respectively; and G_R and K_R are the Reuss average shear and bulk moduli, respectively. In contrast to the Zener index the Universal Anisotropy Index was proposed to incorporate contributions from the volume elasticity part (terms in K). The A^U is zero for isotropic materials and increases as symmetry decreases. Other indexes have been proposed, such as A^F proposed by Fang et al, [108], A^{SU} proposed by Li et al, [109], A^K proposed by Kube [110].

Author Contributions:

Josué García-Ávila: Conceptualization, Methodology, Investigation, Visualization, Writing- Original draft preparation, Software. **Enrique Cuan-Urquizo:** Methodology, Investigation, Formal Analysis, Writing, Review & Editing, Supervision, Resources. **Erick Ramírez-Cedillo:** Supervision, Project Administration. **Ciro A. Rodríguez:** Supervision, Project administration. **Adriana Vargas-Martínez:** Supervision, Project Administration. All authors have read and agreed to the published version of the manuscript.

Acknowledgments:

The authors would like to acknowledge support from CONACyT for Master studies of first author (scholarship number 1002683) and nTopology for providing access to research and academic licenses.

Declaration of conflicting interests:

The Authors declares that there is no conflict of interest.

Funding:

This research was funded by Tecnológico de Monterrey and Mexican National Council for Science and Technology (CONACYT) and J.G.-Á. MSc studies (scholarship number 1002683).

Publication:

The entire contents of this chapter are in the process of published in the *Journal Mathematics and Mechanics of Solids* of SAGE Journals.

CHAPTER 2: Tunable Isotropic Design and Dynamic Topology Optimization of Transtibial Orthopedic Implant with 3D-Printed Structurally Porous PEEK.

Abstract	48
1. Introduction	49
1.1. Transtibial Amputation	49
1.2. Additive Manufacturing of PEEK Implants.....	50
2. Materials and Methods.....	50
2.1. Acquisition Data Processing Model.....	51
2.2. Dynamic Topology Optimization (DTO)	53
2.2.1. Kinematic Model and Multibody Dynamics.....	54
2.2.2. Topology Optimization for Dynamic Loads.....	55
2.3. Manufacturing and Post-Processing Methods (M&PPM)	57
3. Results.....	58
3.1. Isotropic and Lightweight Design with Porous Media	58
3.2. Topologically Optimized Transtibial Implant.....	60
4. Analysis and Discussion	61
5. Conclusion	63
Appendix A Apparent Elastic Properties	63
A.1. Special Case: Normalized Linear Compressibility K^* and Bulk Modulus H^*	64
Appendix B Equations of Motion and Energies	65
Appendix C Anthropometry.....	66

Abstract

Herein, we present the design and manufacturing of a transtibial orthopedic implant. Poly(ether ether ketone) (PEEK) high-performance filament is used to manufacture 3D porous architected implant with tunable isotropy by high-temperature fused filament fabrication (FFF). We seek to improve weight-bearing through the bone structures of the residual limb without the need to resort to a natural bridge as it is usually done. A tailored-made design is achieved by acquiring the topology and morphology of the residual limb and the bone structure of the tibia and fibula using computed tomography (CT) and high-resolution 3D scanning. A dynamic topological optimization method based on gait cycle data (previously reported) was used to reduce the implant mass appropriately. This method, unlike traditional static methods, allows quantifying the variations of the applied forces over time. The equations of motion of a homologous multibody model with three degrees of freedom were proposed to achieve this, using the Euler-Lagrange energy approach. The versatility of density-based optimization SIMP allows homogenization methods for microscale porous architectures into the optimized domain. The designs of the porous architectures were based on a bias-driven tuning symmetry isotropy of triply periodic minimal surface (Primitive surface). The internal porosity of the structure helps to reduce the weight significantly without compromising the isotropic implant behavior.

Keywords: orthopedic implant; topology optimization; transtibial; additive manufacturing; gait cycle; biomechanical design; PEEK.

1. Introduction

1.1. Transtibial Amputation

Despite considerable advances in limb salvage and revascularization, transtibial amputation is a frequent procedure mainly secondary to severe traumatic events or complications of type 2 diabetes. A below-knee or transtibial amputation results in an asymmetry of the patient's weight. Thus, prosthesis use helps improve body symmetry by distributing the patient's weight between the prosthesis and the sound limb (see Figure 1a). Appropriate surgical treatment of lower limb amputation can significantly improve the quality of life, increase comfort, reduce comorbidities, and expand the use of prostheses by patients. However, optimizing weight-bearing distribution between the socket and stump is often a persistent problem unsatisfactorily solved in our days. The main reasons are the changing shape of the residual limb, the increase or decrease of the person's weight, and the weakening of the bony extremities of the tibia and fibula [111] (see Figure 1b). Achieving a more functional residual limb from surgery is achieved by forming a distal bone bridge (also known as osteomyoplasty or osteoperiosteoplasty) that joins the tibia with the fibula forming distal tibiofibular synostosis (see Figure 1c). This technique significantly affects the distribution and transmission of the weight load on the distal end of the residual limb, obtaining a much larger transversal area than in conventional amputations and recreates the tension of the muscles, increasing and stabilizing the surface available for prosthesis fitting [112].

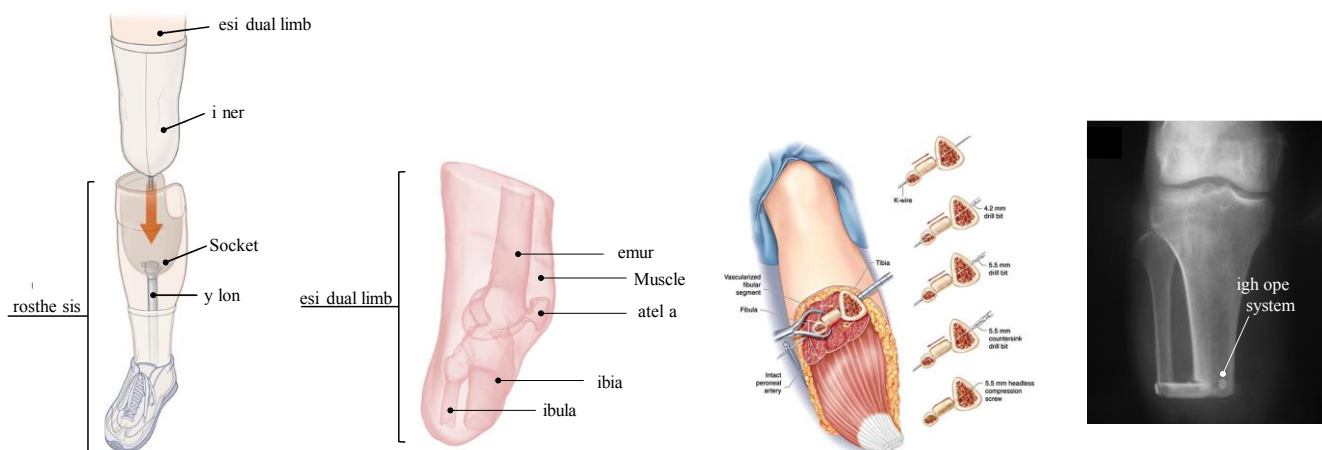


Figure 1. (a) Accessories and parts of a transtibial prosthesis (figure adapted from [113]); (b) Anatomy of the musculoskeletal structure of the transtibial stump; (c) Schematic image of a biological bone bridge surgical procedure (figure from [114]); (d) X-ray of a transtibial amputation shows a Ertl's osteomyoplasty using the TightRope® system 3 months postoperatively (figure adapted from [115]).

Other non-biological techniques such as epiphysiodesis have used small conformal plates (especially in the case of children [116]) and closure of distal bony extremities to avoid deformation of the residual limb. For example, it is usual to fix the distal part of the pedicled osteoperiosteal flap to the distal fibula with a 3.5 mm screw with variable length [117]; the use of headless compression screws has also been reported as well as the TightRope® (Arthrex, Naples, FL) (see Figure 1d), in this last case the patient was able to use a prosthetic device without difficulty. These fixation systems prevent a relative movement between the tibia and the fibula (known as chop-sticking) in a socket that may be uncomfortable injurious[118] and allow to keep the tibiofibular distance constant. In conventional amputations, the lack

of an axial load causes atrophy (pencil) of the residual limb, consequently requiring multiple adjustments of the liner, socket, and prosthesis over time. In addition, the presence of a bony bridge allows the fibula to participate in regular weight-bearing [118]. The most recent solutions propose using oseo-integrated prostheses (e.g., Edo-Exo® [119]) for transfemoral and transtibial amputees [120]. The latter has reported high effectiveness in joining the femur or tibia to the implant structure using a porous abutment. Despite its success, it remains an unaffordable alternative due to the high costs it represents for public health systems in many developing countries and the lack of available financing coverage [121].

1.2. Additive Manufacturing of PEEK Implants

The success of low-cost additive manufacturing processes has enabled patient-specific tuning of implants from three-dimensional bone images reconstructed from computed tomography (CT) and magnetic resonance imaging (MRI). The raw data in DICOM format is processed into a 3D model that serves as a twin digital bone [122]. In recent years, AM technology and the development of biocompatible materials has captured the attention of the orthopedic practice, as it allows for customized implants using the digital twin bone as a reference and given its ability to process high-temperature thermoplastics such as Poly(ether ether ketone) (PEEK). In recent decades, PEEK is a prime 3D printer material candidate to replace metallic and ceramic implants and prostheses in orthopaedic, spine, maxilla-facial, cranial applications [123], [124].

The elastic modulus of PEEK is 3.7–4.0 GPa, being considerably lower than that of cortical bone ranging from 7–30 GPa. However, maximizing stiffness by means of new topological optimization geometries can achieve same mechanical performance. PEEK also has a stable aromatic linear structure with a high melting temperature (T_m) around 343°C and glass transition temperature (T_g) 153 °C. The development of a 3D-printed transtibial bridge implant using dynamic topology optimization has not been reported in the scientific literature until today. Herein, our goal is to implement mechanical optimization based on the dynamic loads of the gait cycle. In addition, a porous TPMS structure is incorporated and designed to fabricate a lightweight transtibial PEEK implant by additive manufacturing (AM). The clinical application case focuses on designing a bridge implant that would join the extremities of the tibia and fibula bones in a person who has undergone a lower extremity amputation.

2. Materials and Methods

A methodology is proposed to manufacture an orthopedic implant validated using three-dimensional digital technologies and mechanical computational simulation. The main aspects of the proposed methodology are based on the integration of the geometric modeling of the bones and residual limb and the topologically optimized design of architected biomaterials for a customized implant. The IDEF0 mapping was used to help identify which elements are a Control (C) (e.g., techniques, parameters), Mechanism (M) (equipment, software), Resources on the left side, and each process output on the right side. The explanation of the Materials and Methods is based on a methodology that identifies the following three main subprocesses: Acquisition Data Processing Model (ADPM), Dynamic Topology Optimization (DTO), and Additive Manufacturing and Post-Processing Methods (AM&PP-M) (see Figure 2).

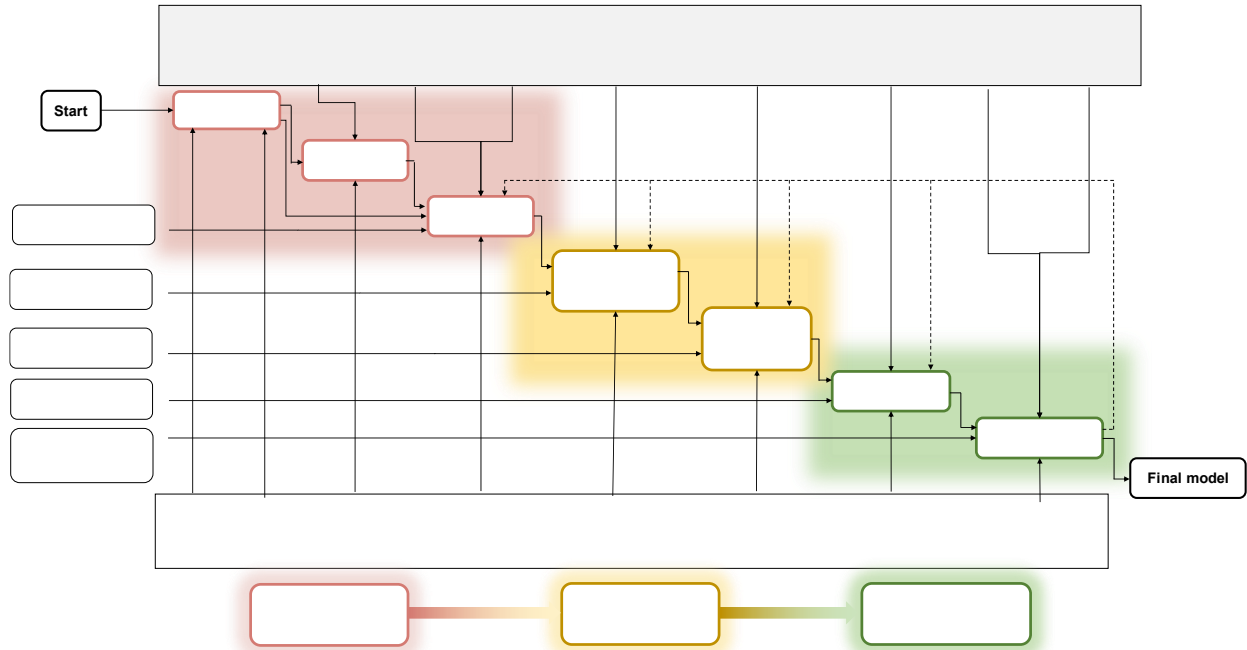


Figure 2. IDEF0 diagram of the transtibial implant design, topology optimization, and manufacturing process.

2.1. Acquisition Data Processing Model

The patient's profile is described as a 63-year-old person; the cause of the amputation is dysvasculature by type 2 diabetes, the amputated limb is on the right side, and the shape of the stump is cylindrical (see Figure 3a-3b). The external geometry of the stump was taken with a HandySCAN 3D® (Creaform, Canada) handheld scanning device (EXAscan model). 64 optical markers were used to create the triangulation. The density and placement of the markers depended on the size and shape of the scanned stump (see Figure 3c). The mesh of the external shape of the stump was exported as an STL file. The geometric virtual models of the bones were obtained via computed tomography (CT) using MedStation Express® and Exprivia software® (Exprivia S.p.A., Italy); parallel sections of the residual limb were obtained as DICOM images processing the area of the lower limb in 395 sections spaced 1 mm apart (see Figure 3d).



Figure 3. (a) Front and (b) lateral stump view; (c) Location of 64 markers around the stump; (d) DICOM lateral image showing a sectional slice of the soft tissues and bones of the stump; (e) Mesh from the 3D EXAscan; (f) Cleaning of digital twin model imperfections.

Data storage and processing is the core of digital technologies applied to implant development. Two types of files were used at this stage: DICOM (Digital Imaging and Communication in Medicine) image, which is the standard for the storage and exchange of medical images, and STL (STereoLithography) file, which is the extension for the standard data transmission in the creation of prototypes accepted in Additive Manufacturing equipment. The DICOM and scanner images must be assembled (joined) using a mathematical model to extract the essential mesh curves of each section and create a clean three-dimensional model (see Figure 3e). This translation of 2D bitmaps into 3D objects is called segmentation. Bone segmentation was performed manually using InVesalius 3.1 opensource software. Using the InVesalius software, the tibia, fibula, patella, and femur bones were identified (see Figure 3f). The segmentation was based on Hounsfield units, an attenuation coefficient of the radiograph to find the bone tissues. For bone, Hounsfield values between 226 and 2028 were designated.

The digitization and CT scan data showed minor discrepancies in the form of small spheres due to noise or missing data that creates some gaps in the 3D model. For solving these problems, a pre-modeling process is required. For this task, software that compiles the point cloud or mesh and allows cleaning the floating data was used; Geomagic Freeform Plus® (3D Systems, USA) was used to improve the mesh structure and perform the modifications and cleaning. Geomagic's embedded methods were used to repair intersections, fill holes, reduce the number of triangles, and sculpt the structure through smoothing and sculpting commands, as well as the decimation technique. The design domain modeling is a prism with dimensions 90mm×70mm×40mm and the individual cavities of each bone prior to dynamic optimization was performed in nTopology® (nTopology, USA). These operations consist of an intersection with the bones and prism volume, and then a 2 mm thick shell geometry is modeled (see Figure 4a).

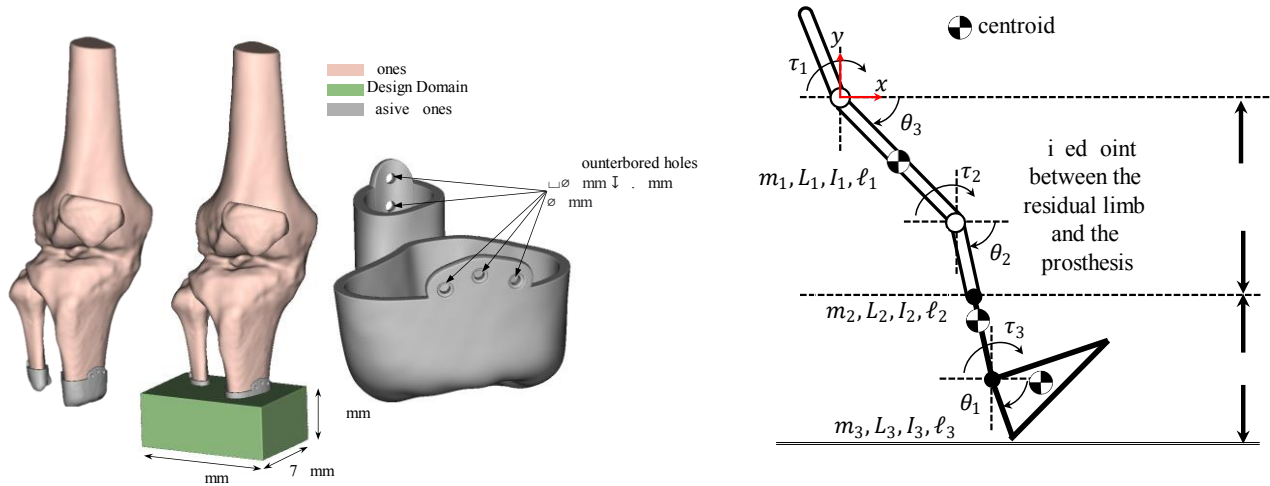


Figure 4, (a) Tibia and fibula caps (passive and immovable zones) and design domain Ω_D (green box); **(b)** Multibody system is modeled as a three degrees-of-freedom mechanism. Each limb segment (thigh, shank, and foot) has different dynamic parameters: mass (m_i), total length (L_i), inertia with concerning center of mass (I_i), distance from the joint to center of mass (ℓ_i), $i = 1,2,3$.

2.2. Dynamic Topology Optimization (DTO)

The analysis uses the methodology of a multibody system to simulate the lower limb system. The anatomical segments are represented kinematically with a homologous model using a set of rigid bodies. The hip joint, knee joint, and ankle joint comprise the multibody dynamic system (MBS); these three joints form three angles (θ_1 , θ_2 , and θ_3). These three angles make the three generalized coordinates (\mathbf{q}_1 , \mathbf{q}_2 , and \mathbf{q}_3). The variations of the angles during the gait cycle represent the condition constraint $\Phi(\mathbf{q}, t) = 0$. $\tau = [\tau_1 \quad \tau_2 \quad \tau_3]^T$ are components of joint torques (see Figure 4b). The variation of ground reaction forces is taken from the one-person test with weight ($m = 55$ kg) presented in [125] (see Figure 5a). This paper's dynamics modeling is based on a four-link system in two dimensions with three degrees of freedom in the sagittal plane (right lateral view of the body). The solution of the dynamics equations as a system of a nonlinear second-order differential algebraic equations implements the MATLAB function

fsolve to obtain the solution of systems of equations and the function *backslash* to find possible redundancies in the system.

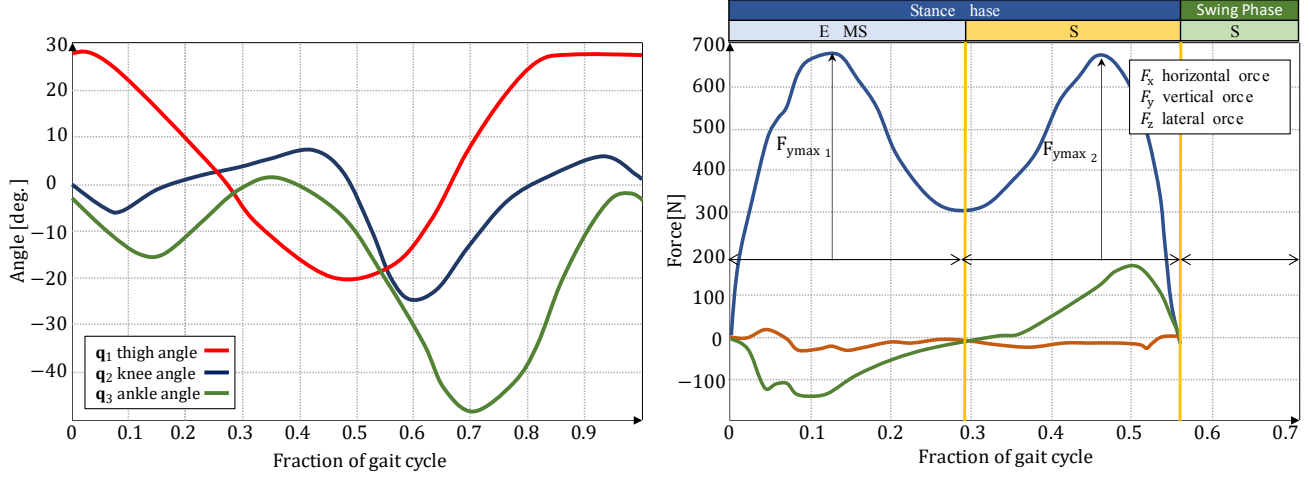


Figure 5. (a) Variation of thigh, knee and ankle angles with respect to fraction of gait cycle; (b) Single stride reference ground reaction force data and gait phase division: Early and Middle Stance Phase (E&MSP), Late Stance Phase (LSP), and Swing Phase (SP).

2.2.1. Kinematic Model and Multibody Dynamics

The equations of motion can be expressed with a set of N dependent coordinates $\mathbf{q} \in \mathbb{R}^N$ (translational or rotational), subjected to M holonomic kinematic constraints $\Phi \in \mathbb{R}^M$ that uniquely determine the position of all the bodies on a certain trajectory, as the following form [126]:

$$\frac{d}{dt} \left(\frac{\partial \mathcal{L}(\mathbf{q}, \dot{\mathbf{q}}, t)}{\partial \dot{\mathbf{q}}} \right) - \frac{\partial \mathcal{L}(\mathbf{q}, \dot{\mathbf{q}}, t)}{\partial \mathbf{q}} + \Phi_{\mathbf{q}}^T(\mathbf{q}, t) \lambda = \mathbf{Q}(\mathbf{q}, \dot{\mathbf{q}}, t) \quad \text{Equation}$$

If,

$$\frac{\partial \mathcal{L}(\mathbf{q}, \dot{\mathbf{q}}, t)}{\partial \dot{\mathbf{q}}} = \mathbf{M}(\mathbf{q}) \dot{\mathbf{q}} \Rightarrow \frac{d}{dt} \left(\frac{\partial \mathcal{L}(\mathbf{q}, \dot{\mathbf{q}}, t)}{\partial \dot{\mathbf{q}}} \right) = \dot{\mathbf{M}}(\mathbf{q}) \dot{\mathbf{q}} + \mathbf{M}(\mathbf{q}) \ddot{\mathbf{q}} \quad \text{Equation}$$

$$\frac{\partial \mathcal{L}(\mathbf{q}, \dot{\mathbf{q}}, t)}{\partial \mathbf{q}} = \frac{\partial \mathcal{T}(\mathbf{q}, \dot{\mathbf{q}}, t)}{\partial \mathbf{q}} - \frac{\partial \mathcal{U}(\mathbf{q}, t)}{\partial \mathbf{q}} \text{ or } \mathcal{L}_{\mathbf{q}} = \mathcal{T}_{\mathbf{q}} - \mathcal{U}_{\mathbf{q}} \quad \text{Equation}$$

Then the application of Equation 1 for the general case with a set of $(M+N)$ differential-algebraic equations (DAEs) of motion can be written as:

$$\begin{cases} \mathbf{M}(\mathbf{q}) \ddot{\mathbf{q}} + \Phi_{\mathbf{q}}^T(\mathbf{q}, t) \lambda = \mathbf{Q}(\mathbf{q}, \dot{\mathbf{q}}, t) - \dot{\mathbf{M}}(\mathbf{q}) \dot{\mathbf{q}} + \mathcal{T}_{\mathbf{q}} - \mathcal{U}_{\mathbf{q}} \\ \Phi(\mathbf{q}, t) = 0 \end{cases} \quad \text{Equation}$$

Equation 1 is called a grange's equations of the first kind [127], where $\Phi_{\mathbf{q}}^T$ is the $N \times M$ transposed Jacobian matrix of the kinematic constraint equations representing the directions of the normal reaction forces; λ is the $M \times 1$ vector of Lagrange multipliers representing the magnitudes of these constraint

forces; \mathbf{q} is the generalized coordinate vector set; Q represents the $N \times 1$ matrix of generalized force (if \mathbf{q} is an angle or a length, Q is a torque or a force as the case may be), and the *Lagrangian* function $\mathcal{L}(\mathbf{q}, \dot{\mathbf{q}}, t) = \mathcal{T}(\mathbf{q}, \dot{\mathbf{q}}, t) - \mathcal{U}(\mathbf{q}, t)$ as the difference between the kinetic (\mathcal{T}) and potential (\mathcal{U}) energy of the system.

Only two external forces affect the model: the gravitational force on each massed segment of the limb, the only externally applied forces on a prosthesis are the ground reaction forces $F_{\text{GRF}} = [F_x \ F_y \ F_z]^T$. Applying Jacobian linear force transformation (by projecting) $Q(\mathbf{q}, \dot{\mathbf{q}}, t)$ is opposed to the reaction $\Phi_{\mathbf{q}}^T(\mathbf{q}, t)\lambda$, where $\lambda = F_{\text{GRF}}$.

$$Q = \Phi_{\mathbf{q}}^T \cdot F_{\text{GRF}} + \tau \quad \text{Equation}$$

Figure 5b shows two peaks, the first one after the heel strike of the foot with the ground ($F_{y_{\text{max}_1}}$) and the second one before toe-off ($F_{y_{\text{max}_2}}$). The vertical forces F_y represent the ground reaction due to the bodyweight during the gait cycle, and both peaks are positive, while for the horizontal force F_x the first peak is negative and the second positive, the medial-lateral force is not taken into account in our calculation. For the analysis of the ground reaction forces of the gait cycle, the following system dynamics model is proposed:

$$M(\mathbf{q})\ddot{\mathbf{q}} + C(\mathbf{q}, \dot{\mathbf{q}})\dot{\mathbf{q}} + K(\mathbf{q}) = \Phi_{\mathbf{q}}^T(\mathbf{q}, t)\lambda + \tau(\mathbf{q}, t) \quad \text{Equation}$$

Equation 6 is identical to Equation 1 and Equation 4. The term $M(\mathbf{q})\ddot{\mathbf{q}}$ represents the inertial forces, in which $M(\mathbf{q})$ is the $N \times N$ generalized mass/inertia matrix (kinetic energy); $\mathbf{q}, \dot{\mathbf{q}}, \ddot{\mathbf{q}}$ are the $N \times 1$ position, velocity, and acceleration vectors; $C(\mathbf{q}, \dot{\mathbf{q}})\dot{\mathbf{q}} \sim \{\dot{M}(\mathbf{q})\dot{\mathbf{q}} - \mathcal{T}_{\mathbf{q}}\}$ is an $N \times N$ coupling matrix to global velocity vector (viscous damping, gyroscopic: centrifugal and Coriolis forces) that represent rotational kinetic energy; $K(\mathbf{q}) \sim \{\mathcal{U}_{\mathbf{q}}\}$ represents $N \times 1$ coupling matrix-vector (stiffness, circulatory: gravity forces) that represent potential and strain energy.

2.2.2. Topology Optimization for Dynamic Loads

To achieve dynamic optimization must be determined the displacement, velocity, and acceleration at time. Therefore, the Newmark method (explicit case of the central difference scheme) is chosen as the time integrator [128], defining first the velocity and acceleration as follows:

$$\begin{cases} \dot{\mathbf{q}}_k = \frac{1}{2\Delta t} (\mathbf{q}_{k+1} - \mathbf{q}_{k-1}) \\ \ddot{\mathbf{q}}_k = \frac{1}{\Delta t^2} (\mathbf{q}_{k+1} - 2\mathbf{q}_k + \mathbf{q}_{k-1}) \end{cases} \quad \text{Equation 7}$$

The displacement for time t_{k+1} is obtained by considering at time t_k , for notational simplicity we assume $M = M(\mathbf{q})$, $C = C(\mathbf{q}, \dot{\mathbf{q}})$, and $K = K(\mathbf{q})$

$$M\ddot{\mathbf{q}}_k + C\dot{\mathbf{q}}_k + K = Q \quad \text{Equation}$$

Substituting the Equation 7 into Equation 8 and factor the terms \mathbf{q}_{k-1} , \mathbf{q}_k and \mathbf{q}_{k+1} ,

$$\left(\frac{1}{\Delta t^2} M + \frac{1}{2\Delta t} C \right) \mathbf{q}_{k+1} = Q - \left(K - \frac{2}{\Delta t^2} M \right) \mathbf{q}_k - \left(\frac{1}{\Delta t^2} M - \frac{1}{2\Delta t} C \right) \mathbf{q}_{k-1} \quad \text{Equation}$$

The pseudo algorithm for solving the equation with time gradient time can be summarized as follows [129]:

- 1) calculate of M, C, K matrices,
- 2) initialize with the displacement, velocity, and acceleration $\mathbf{q}_k, \dot{\mathbf{q}}_k, \ddot{\mathbf{q}}_k$ at time $t = 0 = t_0$,
- 3) set the time step Δt , see [130],
- 4) calculate an initial guess $\mathbf{q}_{-1} = \mathbf{q}_0 - \Delta t \dot{\mathbf{q}}_0 + \Delta t^2 \frac{\ddot{\mathbf{q}}_0}{2}$,
- 5) use Equation 9 to calculate displacements at t_{k+1} .

The objective function ϕ (for mean dynamic compliance $C_d = F^T \mathbf{q} = \mathbf{q}^T \mathbf{K} \mathbf{q}$) of the topological optimization (T \odot) of the multibody system subjected to transient loads can be defined as [25],

$$\phi(x, \mathbf{q}, t) = \frac{1}{\Delta t} \int_{t_i}^{t_f} \mathbf{q}_k^T \mathbf{K} \mathbf{q}_k dt = \frac{1}{t_f - t_i} \int_{t_i}^{t_f} \phi(x, s, t) dt \approx \frac{1}{s+1} \sum_{k=0}^s \phi(x, \mathbf{q}_k, t_k) \quad \text{Equation}$$

where, x is the design variable, s is the total number of time steps; t_i is the initial time t_s is the end time and t_k is the k^{th} time step. The discrete approximation with equal time steps implies $\Delta t = (t_f - t_i)/s$. The equilibrium constraint means satisfying the set equations of motion. Therefore, the optimization problem a system consisting of n_j rigid or flexible bodies has been used proposed by other authors [130], as follows,

$$\text{T}\odot \left\{ \begin{array}{l} \text{find } x = (x^j)_{j=1}^{n_j} \in \mathbb{R}^{n_j}, \quad n = \sum_{j \in \mathbf{J}} n_j, \quad \mathbf{J} = \{1, \dots, n_j\} \\ \min_{x^j, \mathbf{q}_k^j} \phi^j(x^j, \mathbf{q}_k^j) = \frac{1}{s+1} \sum_{k=0}^s \phi^j(x^j, \mathbf{q}_k^j, t_k) \\ \text{subject to } \begin{cases} M^j \ddot{\mathbf{q}}_k + C \dot{\mathbf{q}}_k + K(\mathbf{q})_k = F_k, \\ \Phi(\mathbf{q}, t_k) = 0 \end{cases} \\ \text{and } \begin{cases} g^j(x^j) = \sum_{e=1}^{n_e} x_e^j V_e^j \leq V_{\max}^j \\ x^j \in [x_{\min}^j, x_{\max}^j] \end{cases} \end{array} \right. \quad \text{Equation}$$

where, j indicates that the variable refers to the body j which will be optimized; x is the design variable with lower and upper bounds x_{\min}, x_{\max} ; g is the mass constraint function; V_{\max} is the maximum available material volume; V_e is the volume of finite element e , and n_e is the total number these elements. The convergence criterion is the change in the norm of the design variable $\|x_{k+1}^j - x_k^j\| < \epsilon$, where ϵ is a given small threshold, if the convergence criterion is met, the optimization iteration process stops. The dynamic topology optimization problem is solved using the density-based approach [134]. The sensitivity and filtering (governed by the parameters r_{\min} and β) methods used in this work were adopted from previous work presented extensively in [131], [132], [135]. The penalty method was adopted from [136] where they use an adaptation of the solid isotropic material with penalization (SIMP) power-law interpolation scheme to relate the design variable x_e^j , the density ρ_e^j , and Young's modulus E_e^j of each finite element e is described as follows:

$$\begin{aligned}
E_e^j(x) &= (x_e^j)^p E_s^j \\
\rho_e^j(x) &= \begin{cases} c(x_e^j)^q \rho_s^j, & x_{\min}^j \leq x_e^j < 0.1 \\ x_e^j \rho_s^j, & 0.1 \leq x_e^j \leq 1 \end{cases}
\end{aligned}
\tag{Equation}$$

where E_s^j and ρ_s^j is the Young's modulus and Poisson's ratio of the isotropic solid material, respectively; p is the penalization term value; it is common to use $p > 1$ to expedite the convergence of parameters.

The mechanical properties of the bone are assumed to be linear, isotropic, and homogeneous. Simplifying and reduce the computation time has neglected the influence of soft tissues (muscle, fat, and skin). The tibia and fibula bones were modeled with linear elastic behavior (Young's modulus of 17,700 MPa and Poisson's ratio of 0.3). The values used for the optimization and the mechanical properties of the implant material are listed in Table 1.

Table 1. Parameter values used for dynamic optimization and material properties of the polyetheretherketone (PEEK) filament.

	V
Maximum iterations	
Minimum filter radius r_{\min}	mm
Elementwise projection parameter β	
Element length l_e	mm
Minimum Design Domain $x_{\min} = \epsilon$	5×10^{-4}
Maximum design domain x_{\max}	.
Maximum volume fraction V_{\max}	.
SIM penalization coefficients p, q, c	, , 10^5
Time Step Size Δt	s
Total time steps	
Simulation time t_i, t_f	s, s
Z	V
Young's modulus of solid E_s	.7 G a
Elastic Modulus	.7 G a
Mass Density ρ_s	. g cm
Poisson's ratio ν_s	.
Tensile Strength	M a
Elastic Strength	M a
Tensile Elongation	

2.3. Manufacturing and Post-Processing Methods (M&PPM)

The transtibial implant was additively manufactured via fused filament fabrication (FFF) using PEEK (K-PEEK 450G, Victrex, Lancashire, UK) filament. All samples were manufactured with a high-temperature polymer FFF 3D printer (Zortrax Endureal, Karlsruhe, Germany). Iterative testing of printing parameters such as temperature, speed, and layer height was performed in order to establish a set of consistent parameters that can be used to print each geometry. These parameters determined the structure quality by affecting printing conditions including the flow of melted filament, the success of inter-layer adhesion, and the ability of PEEK filament to bridge between underlying struts. We completed

iterative testing once we obtained a set of parameters that was able to produce sturdy cubes of each porous geometry ($\bar{\rho} = 0.8, 0.6, 0.4$), with pores that appeared consistent in shape and size under visual inspection. Additionally, we examined the openness of the inner pores by holding the cubes up to a light and confirming that the illuminated grid of pores was consistent with the grid seen in the designed model. Solid PEEK cubes were also printed for use as controls using these parameters, though a higher temperature was needed to ensure interlayer adhesion over the larger surface area. Samples used for mechanical testing were $24 \times 24 \times 24$ mm cubes with $3 \times 3 \times 3$ unit cells array.

The primary use of this type of material is to fabricate definitive implant trials or functional dummy implants (low-cost implants prototypes) that can be used by surgeons to determine correct implant dimensions and placement without using the definitive packaged implant. Certain pre- and post-printing treatments are required when processing high-temperature materials in the Zortrax Endureal. Aside from the printing process, which must be carried out with adequate thermal parameters, we've reduced material treatment to two steps that aid in achieving the desired printing results and final model properties. The first is the drying of the filament. It should be done prior to printing to reduce the amount of moisture in the material, which, if not removed, could have an adverse effect on the thermal and mechanical properties of the printed model. Similarly, finished prints must go through a controlled process known as "annealing," in which they are heated to their glass transition temperature (below the melting point), held there for a period, and then slowly cooled. Annealing dissipates stresses accumulated within models during the printing process and improves physical and mechanical properties significantly without changing their initial shape. Both procedures are carried out in the Endureal's main chamber and have dedicated menu options. The solutions implemented in this industrial 3D printer have made working with difficult filaments as simple as working with standard ABS or PLA. Users can simply begin printing and, after some time, remove supports from the printed model with very little effort required for material treatment.

3. Results

3.1. Isotropic and Lightweight Design with Porous Media

The modeling of porous media is based on the next implicit function $F: \mathbb{R}^3 \rightarrow \mathbb{R}$,

$$F(x, y, z) = \cos x + \cos y + \cos z + \ell \quad \text{Equation}$$

This mathematical function generates the Primitive surface or P-surface, which is part of the family of triply periodic minimal surfaces (TPMS). The modulation allows obtaining different level surfaces from the implicit function. Previous work [137], [138] have shown that this value has symmetry in the relative density for $\pm \ell$ (bias parameter). The intermediate value ($\ell = 0$) corresponds to that of the widely spread standard solid P-surface. Figure 6 shows that this structure shows symmetry also in its apparent properties (linear, shear, and bulk moduli and Poisson's ratio) even though its unit cell geometry is different, and it is also possible to obtain better anisotropy values with higher values of $\|\ell\|$.

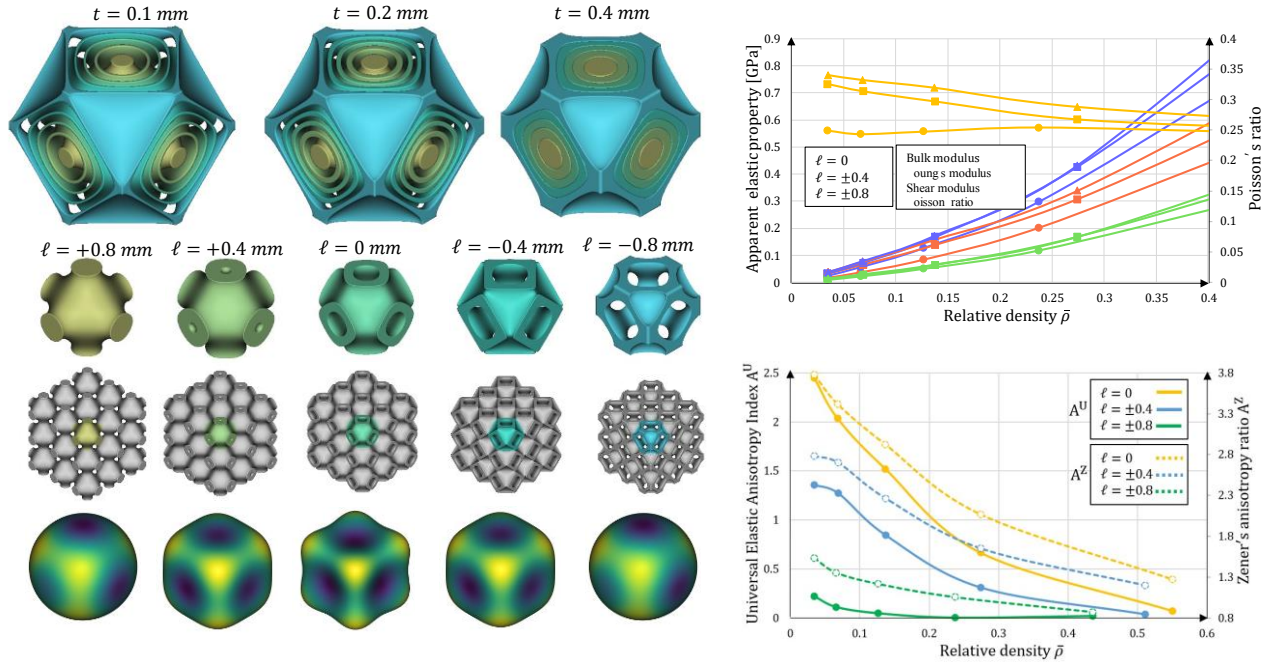


Figure 6. (a) Unit cell $10 \times 10 \times 10$ mm of solid Primitive structures with different values of the ℓ -parameter with thickness t of 0.1 mm, 0.2 mm, and 0.4 mm; (b) unit cell with a thickness $t=0.8$ mm; (c) $3 \times 3 \times 3$ unit cell array; (d) anisotropy representation elastic modulus of the unit cell; (e) apparent elastic properties of the unit cells; (f) Variation of the Universal Elastic Anisotropy Index A^U and Zener ratio A^Z .

Primitive is one of the TPMS structures with the highest anisotropy, yet it is the one that tends to have far superior properties when subjected to fatigue loads. The intuitive and logical idea is that increasing the relative density $\bar{\rho}$ by increasing only the thickness t results in more isotropic structures. Although this idea is confirmed, our simulations and anisotropy calculations based on the Universal Elastic Anisotropy Index A^U (see Figure 7a) and the Zener Index A^Z (see Figure 7b) show that this is the most inefficient way to design porous structures based on a single design parameter. For example, considering that the relative density and Young's modulus are functions of two parameters, it is possible to model contour lines transposed on the anisotropy contour lines. As can be seen in Figure 7c point A and point B are in the same relative density band between 15% and 30%, and as can also be seen in Figure 7d these same points have Young's modulus between 0.4 GPa and 0.8 GPa, the big difference is that point B has a higher isotropy.

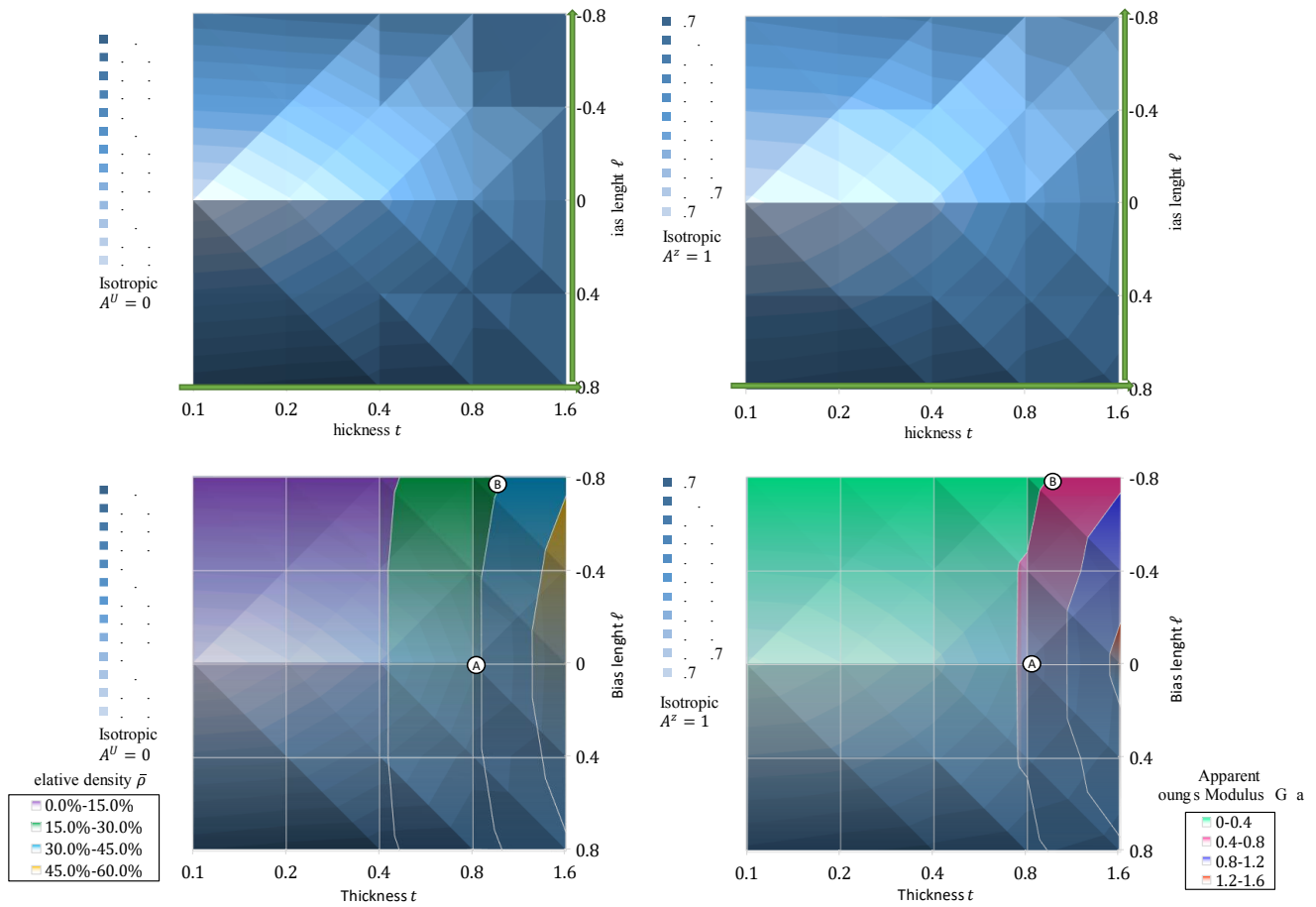


Figure 7. Contour lines of anisotropy variation using the universal anisotropy index A^u (a) and Zener's ratio (b) showing the symmetry that generalizes the l parameter; (c) Overlaid relative density and (d) apparent Young's modulus value bands.

3.2. Topologically Optimized Transtibial Implant

Topological optimization incorporates porous structure following a contour line field mapping of the Primitive structure taking Equation 11 as a starting point. This technique is based on the principle known as set-based design (SBD), which considerably reduces the homogenization and remapping calculations. The contour lines presented in this section are based on 25 individual simulations of unit cell homogenization with the combinations generated by the $l = \{-0.8, -0.4, 0, 0.4, 0.8\}$ and $t = \{0.1, 0.2, 0.4, 0.8, 1.6\}$ cases.

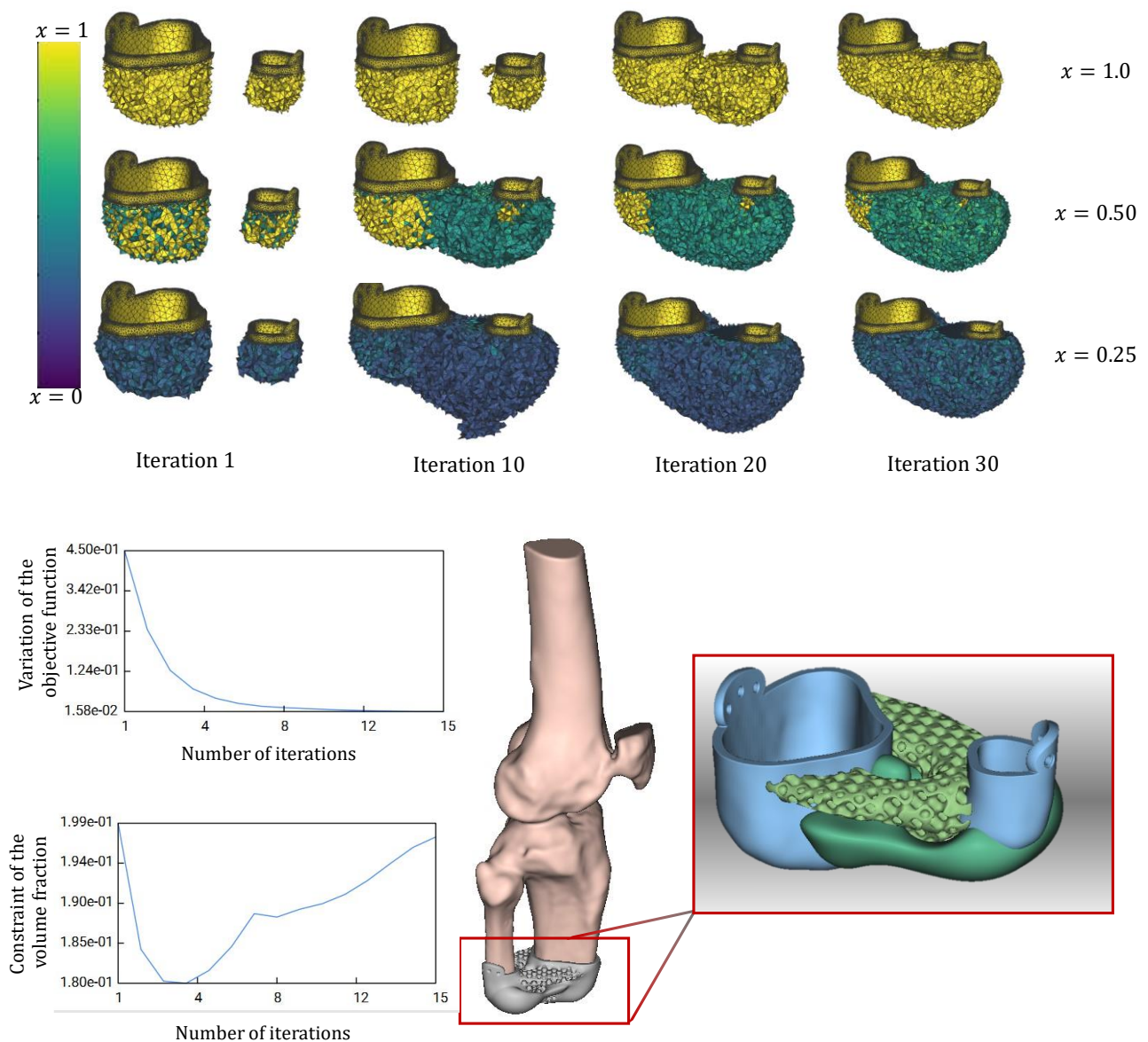


Figure 8. (a) Iteration history process of density field x ; (b) the objective function history; (c) the constraint (volume fraction) function history; (d) final design implant with architected structure.

4. Analysis and Discussion

The mechanical characterization of implants faces the challenge of better fatigue behavior at cyclic loading with dynamic stresses [139]. The primary load cycle of the human body is gait, which is a complex process consisting of consecutive and repetitive stages. Novel research has successfully adopted musculoskeletal modeling to study the finite element analysis of total knee arthroplasty [140] and hip joint replacement [141] without incorporating topological optimization. Therefore, a better design must be topologically optimized and must also consider the principal stresses generated during the patient's gait. In the specific case of lower limb amputation, the moments generated by the prosthesis are transmitted through the soft tissue of the socket interface and not directly to the skeletal structures as occurs in the intact lower limb. The most significant load on the residual limb occurs during the stance phase of gait due to the significant bending moment and dramatically contributes to the optimizing

process. The nature of moment transfer at the socket interface changes dynamically. This phenomenon generates different pressure concentrations on the anterior and posterior stump during the gait cycle (see Figure 9a). Dynamic topologic optimization is a promising solution since it allows using a transient response, depending on the time t . To achieve a better material distribution within the implant design domain $\Omega_D \subset \mathbb{R}^3$, an objective function ϕ is subject to a set of contour constraints Γ (see figure 9 b).

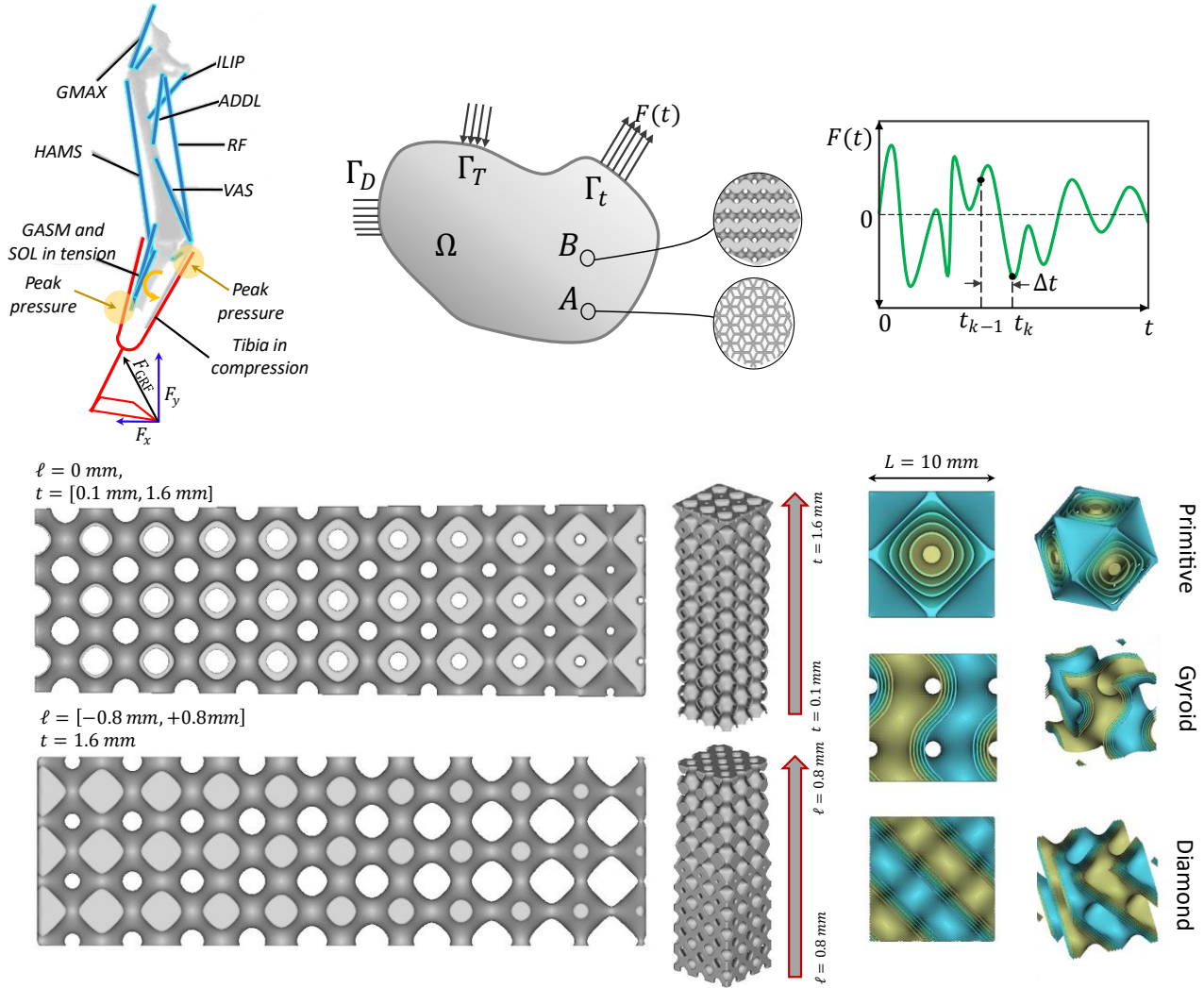


Figure 9. (a) Ground reaction forces and their effect on pressure peaks at the socket-stump interface and tension or compression behavior of the gastrocnemius (GASM) and soleus (SL) muscles and the tibia and fibula bones; (b) Graphical representation of the design domain subject to topological optimization with transient loads at time t , point -B- shows a surface-based structure and point -A- a beam-based structure; (c) thickness and bias (d) variation in a structure based on Primitive surface; (e) unit cell overlays of the TPMS Gyroid, Diamond and Primitive structures with various bias values.

The optimization based on porous structures with PEEK as bulk material allows solving another problem present in the use of metallic implants, which is caused by the high difference in Young's modulus values between a classical metallic implant (AISI 316L SS: 193 GPa) and the bone (10–30 GPa). This difference in stiffness causes stress-shielding phenomena (osteopenia). The primary adverse outcome is damage that reduces bone density at the interface with the implant, making it more fragile and subject to fracture. Therefore, the implementation of surface-based structures is a promising solution for building lightweight scaffolds from a biocompatible material and achieving biomimetic mechanical properties.

Surface-based structures can vary their porosity level using two parameters, on the one hand, their thickness t (see Figure 9 c), and on the other hand, their radial offset or bias length ℓ (see Figure 9d) from the base surface. The Primitive structure used in this paper is quite illustrative to show this last point compared to other structures. (see Figure 9e). Although these structures have a smooth curved topology, the surfaces often have sharp edges that can cause damage to the surrounding tissue; A feasible and commercially available solution is to incorporate the polyethylene surgical foam. Finally, the synthesis of the porous structure based on two design parameters made it possible to find the optimal design point of the isotropy condition ($A^U \approx 0$ and $A^Z \approx 1$) of the structure.

5. Conclusion

Personalized medicine is revolutionizing the way in which physicians and surgeons approach a patient's needs. Implants must be tailored to patients' individual needs, who are the end-user. Improved imaging technologies, coupled with the ability to fabricate parts by additive manufacturing, allow surgeons, radiologists, and other multidisciplinary teams to manufacture implants in their hospitals. This process would be a tremendous advantage for surgical planning, thus reducing costs and lead times to produce implants from third-party suppliers. The research presented shows an efficient way to optimize the topology of an implant based on the dynamic behavior of a multibody system. The approach to topological optimization uses an adaptation of the SIMP method to interpolate the stiffness of the materials and incorporate the apparent properties of the porous structure with the lowest possible anisotropy values. The design proposal based on surface structures and the modeling using two parameters allows achieving more isotropic porous structures, ensuring equitable directional of their apparent properties.

This work reveals the possibility of improved designs using an appropriate objective function and porous structure. Furthermore, the constraints given from the equations of motion for calculating the moment and position of the applied loads should be considered in the structural dynamics design process to achieve implants with better mechanical properties. This knowledge contributes to the promising research line of optimal implant design based on dynamic loading using the multibody technique and gait cycle trajectories. The present work results offer the possibility of extending, in further studies, the range of kinematics and dynamics; a further improvement could include the inclusion of abnormal gait, friction coefficients, and nonlinear soft tissue elasticity to apply this framework in a more successful scenario.

Appendix A Apparent Elastic Properties

The 6×6 matrix of the apparent stiffness tensor \mathbb{C}_{ij}^* is obtained from the homogenization process computed in nTopology®. The normalization (Ψ^*/Ψ_S) of the apparent property Ψ^* with respect to the base material properties Ψ_S is performed as an internal calculation of the algorithm. The four direct apparent mechanical properties – linear compressibility, Young's modulus, shear modulus and Poisson's ratio– are obtained using apparent compliance constants S_{ij} from the tensor \mathbb{S}_{ij}^* as follow [142], [143]:

- Young's modulus, $E(\mathbf{u})$: Defined as the uniaxial stiffness (ratio of stress to strain) of the material in the direction of unit vector \mathbf{u} .

$$\frac{1}{E^*} = S_{11}l_1^4 + S_{22}l_2^4 + S_{33}l_3^4 + (2S_{12} + S_{66})l_1^2l_2^2 + (2S_{23} + S_{44})l_2^2l_3^2 + (2S_{13} + S_{55})l_1^2l_3^2$$

where l_1, l_2 and l_3 are direction cosines of uniaxial vector \mathbf{u} .

- Linear compressibility, $K(\mathbf{u})$: Defined as the linear deformation in direction \mathbf{u} as a response to isostatic (hydrostatic) compression stress.

$$K^* = (S_{11} + S_{12} + S_{13})l_1^2 + (S_{12} + S_{22} + S_{23})l_2^2 + (S_{13} + S_{23} + S_{33})l_3^2$$

- Shear modulus, $G(\mathbf{u}, \mathbf{n})$: Defined as the resistance to shearing of the plane normal to \mathbf{n} in the direction \mathbf{u} .

$$\frac{1}{G^*} = 4S_{11}l_{11}^2l_{21}^2 + 4S_{22}l_{12}^2l_{22}^2 + 4S_{33}l_{13}^2l_{23}^2 + 8S_{12}l_{11}l_{21}l_{12}l_{22} + 8S_{23}l_{11}l_{21}l_{13}l_{23} + 8S_{13}l_{11}l_{21}l_{13}l_{23} + S_{44}(l_{12}l_{23} + l_{22}l_{13})^2 + S_{55}(l_{11}l_{23} + l_{21}l_{13})^2 + S_{66}(l_{11}l_{22} + l_{21}l_{12})^2$$

where $l_{11}, l_{12},$ and l_{13} are direction cosines of the shear stress direction \mathbf{u} and $l_{21}, l_{22},$ and l_{23} are direction cosines of the shear plane normal \mathbf{n} .

- Poisson's ratio, $\nu(\mathbf{u}, \mathbf{v})$: Characterizes the (negative) ratio of transverse or longitudinal strain in direction \mathbf{v} to lateral or axial strain in direction \mathbf{u} , when uniaxial stress is applied.

$$\nu(\mathbf{u}, \mathbf{v}) = -\frac{\varepsilon_{ij}\mathbf{u}_i\mathbf{u}_j}{\varepsilon_{rs}\mathbf{v}_r\mathbf{v}_s}$$

A.1. Special Case: Normalized Linear Compressibility K^* and Bulk Modulus B^*

Here a distinction between K_i^* (linear principal compressibility), K_V^* (volume compressibility), and B^* (bulk modulus). Some authors prefer to use the symbols β or κ to refer to compressibility. The relationship between them is as follows:

$$K_V^* = K_1^* + K_2^* + K_3^*$$

$$B^* = K_V^{*-1}$$

The correct procedure for normalizing the bulk modulus is $K_V^*/K_S = 3 \times K_i^*/K_S$, where K_S is the bulk modulus of the isotropic continuous base material calculated from $K_S = E_S/[3(1 - 2\nu)]$. This observation is important because it is common to forget the $3 \times$ factor involved in the calculation, and it is rare to find in the literature the normalization of the bulk modulus for porous structures.

<p style="text-align: center;">$I \quad p \quad c$</p> <p>the bulk modulus is the reciprocal of the volume compressibility,</p> $B_{\text{iso}}^* = \frac{1}{K_V^*}$ <p>or isotropic materials, $K_i = K_V/3$.</p>	<p style="text-align: center;">$Cu \quad c$</p> <p>the linear compressibility of both cubic and isotropic structures is independent of the direction,</p> $B_{\text{cubic}}^* = \frac{1}{3(S_{11} + 2S_{12})} = \frac{1}{3K_i^*}$ <p>or cubic materials, $K_i^* = K_1^* = K_2^* = K_3^*$</p>
--	--

Appendix B Equations of Motion and Energies

The dynamic model can be mathematically written as:

$$\begin{bmatrix} M_{(1,1)} & M_{(1,2)} & M_{(1,3)} \\ M_{(2,1)} & M_{(2,2)} & M_{(2,3)} \\ M_{(3,1)} & M_{(3,2)} & M_{(3,3)} \end{bmatrix} \begin{bmatrix} \dot{\theta}_1 \\ \dot{\theta}_2 \\ \dot{\theta}_3 \end{bmatrix} + \begin{bmatrix} C_{(1,1)} & C_{(1,2)} & C_{(1,3)} \\ C_{(2,1)} & C_{(2,2)} & C_{(2,3)} \\ C_{(3,1)} & C_{(3,2)} & C_{(3,3)} \end{bmatrix} \begin{bmatrix} \theta_1 \\ \theta_2 \\ \theta_3 \end{bmatrix} + \begin{bmatrix} K_1 \\ K_2 \\ K_3 \end{bmatrix} = \begin{bmatrix} Q_1 \\ Q_2 \\ Q_3 \end{bmatrix}$$

Mass matrix

$$M_{(1,1)} = m_1 \ell_1^2 + I_1 + m_2 (L_1^2 + \ell_2^2 + 2L_1 \ell_2 C_2) + I_2 + m_3 (L_1^2 + L_2^2 + \ell_3^2 + 2L_1 L_2 C_2 + 2L_1 \ell_3 C_{23}) + I_3$$

$$M_{(1,2)} = m_2 (\ell_2^2 + L_1 \ell_2 C_2) + I_2 + m_3 (L_2^2 + \ell_3^2 + L_1 L_2 C_2 + L_1 \ell_3 C_{23} + 2L_2 \ell_3 C_3) + I_3$$

$$M_{(1,3)} = m_3 (\ell_3^2 + L_1 \ell_3 C_{23} + L_2 \ell_3 C_3) + I_3$$

$$M_{(2,2)} = m_2 \ell_2^2 + I_2 + m_3 (L_2^2 + \ell_3^2 + 2L_2 \ell_3 C_3) + I_3$$

$$M_{(2,3)} = m_3 (\ell_3^2 + L_2 \ell_3 C_3) + I_3$$

$$M_{(3,3)} = m_3 \ell_3^2 + I_3$$

$$M_{(2,1)} = M_{(1,2)}$$

$$M_{(1,3)} = M_{(3,1)}$$

$$M_{(2,3)} = M_{(3,2)}$$

Coriolis and centrifugal Vector

$$C_{(1,1)} = -2m_2 L_1 \ell_2 S_2 \dot{\theta}_2 - 2m_3 L_1 L_2 S_2 \dot{\theta}_2 - 2m_3 L_1 \ell_3 S_{23} (\dot{\theta}_2 + \dot{\theta}_3) - 2m_3 L_1 \ell_3 S_3 \dot{\theta}_3$$

$$C_{(1,2)} = -m_2 L_1 \ell_2 S_2 \dot{\theta}_2 - m_3 L_1 L_2 S_2 \dot{\theta}_2 - m_2 L_1 \ell_3 S_{23} (\dot{\theta}_2 + \dot{\theta}_3) - 2m_3 L_1 \ell_3 S_3 \dot{\theta}_3$$

$$C_{(1,3)} = -m_2 L_1 \ell_3 S_{23} (\dot{\theta}_2 + \dot{\theta}_3) - m_3 L_1 \ell_3 S_3 \dot{\theta}_3$$

$$C_{(2,1)} = -m_2 L_1 \ell_2 S_2 \dot{\theta}_2 - m_3 L_1 L_2 S_2 \dot{\theta}_2 - m_3 L_1 \ell_3 S_{23} (\dot{\theta}_2 + \dot{\theta}_3) - 2m_3 L_2 \ell_3 S_3 \dot{\theta}_3 + m_2 L_1 \ell_2 S_2 \dot{\theta}_1 + m_3 L_1 L_2 S_2 \dot{\theta}_1 + m_3 L_1 \ell_3 S_{23} \dot{\theta}_1$$

$$C_{(2,2)} = -2m_3 L_2 \ell_3 S_3 \dot{\theta}_3 + m_2 L_1 \ell_2 S_2 \dot{\theta}_1 + m_3 L_1 L_2 S_2 \dot{\theta}_1 + m_3 L_1 \ell_3 S_{23} \dot{\theta}_1$$

$$C_{(2,3)} = -m_3 L_2 \ell_3 S_3 \dot{\theta}_3 + m_3 L_1 \ell_3 S_{23} \dot{\theta}_1$$

$$C_{(3,1)} = m_3 L_1 \ell_2 S_{23} \dot{\theta}_1 + m_3 L_2 \ell_3 S_3 (\dot{\theta}_1 + \dot{\theta}_2)$$

$$C_{(3,2)} = m_3 L_2 \ell_3 S_3 (\dot{\theta}_1 + \dot{\theta}_2)$$

$$C_{(3,3)} = 0$$

Gravity Vector

$$K_1 = m_1 g \ell_1 C_1 + m_2 g (L_1 C_1 + \ell_2 C_{12}) + m_3 g (L_1 C_1 + L_2 C_{12} + \ell_3 C_{123})$$

$$K_2 = m_2 g \ell_2 C_{12} + m_3 g (L_2 C_{12} + \ell_3 C_{122})$$

$$K_3 = m_3 g \ell_3 C_{123}$$

where $C_u = \cos \theta_u$, $C_{uv} = \cos(\theta_u + \theta_v)$, $C_{uvw} = \cos(\theta_u + \theta_v + \theta_w)$, $S_u = \sin \theta_u$, $S_{uv} = \sin(\theta_u + \theta_v)$, $S_{uvw} = \sin(\theta_u + \theta_v + \theta_w)$; for $u, v, w = 1, 2, 3$.

Forces Vector

The right hand of the equation of motion is:

$$\begin{bmatrix} Q_1 \\ Q_2 \\ Q_3 \end{bmatrix} = \begin{bmatrix} \tau_1 - \tau_2 \\ \tau_2 - \tau_3 \\ \tau_4 \end{bmatrix} + \Phi^T \begin{bmatrix} F_x \\ F_y \\ F_z = 0 \end{bmatrix}$$

Jacobian Matrix

$$\Phi = \begin{bmatrix} \phi_{11} & \phi_{12} & \phi_{13} \\ \phi_{21} & \phi_{22} & \phi_{23} \\ \phi_{31} & \phi_{32} & \phi_{33} \end{bmatrix}$$

$$\phi_{11} = -L_1 \sin(\theta_1) - L_2 \sin(\theta_1 + \theta_2) - L_3 \sin(\theta_1 + \theta_2 + \theta_3)$$

$$\phi_{12} = -L_2 \sin(\theta_1 + \theta_2) - L_3 \sin(\theta_1 + \theta_2 + \theta_3)$$

$$\phi_{13} = -L_3 \sin(\theta_1 + \theta_2 + \theta_3)$$

$$\phi_{21} = L_1 \cos(\theta_1) + L_2 \cos(\theta_1 + \theta_2) + L_3 \cos(\theta_1 + \theta_2 + \theta_3)$$

$$\phi_{22} = L_2 \cos(\theta_1 + \theta_2) + L_3 \cos(\theta_1 + \theta_2 + \theta_3)$$

$$\phi_{23} = L_3 \cos(\theta_1 + \theta_2 + \theta_3)$$

$$\phi_{31} = 1$$

$$\phi_{32} = 1$$

$$\phi_{33} = 1$$

Appendix C Anthropometry

In the particular model presented here, $j = 1$ corresponding to the thigh, $j = 2$ corresponding to the shank, and $j = 3$ corresponding to the foot. I_j is the moment of inertia of the shank/foot. m_j is the total mass of the shank/foot. l_j is the equivalent total length of the shank/foot, where j is the identification number of joints.

Table C.1 Anthropometric parameters of human lower segments, where m and H are the mass and height of the person, respectively [144].

Mass m_i	$m_1 = 0.1 \times m$	$m_2 = 0.0465 \times m$	$m_3 = 0.0145 \times m$
Length L_i	$L_1 = 0.245 \times H$	$L_2 = 0.246 \times H$	$L_3 = 0.152 \times H$
Moment of Inertia I_i	$I_1 = m_1 \times (0.323 \times L_1)^2$	$I_2 = m_2 \times (0.302 \times L_2)^2$	$I_3 = m_3 \times (0.475 \times L_3)^2$
Equivalent Mass ℓ_i	$\ell_i = 0.433 \times L_1$	$\ell_2 = 0.433 \times L_2$	$\ell_3 = 0.5 \times L_3$
	from hip	from knee	from ankle

Table C.2 Anthropometric segments parameters [145].

	V
patient body mass m	kg
patient stature H	.7 m
foot length (L_3)	. m
Shank length (L_2)	. m
thigh length (L_1)	. m
foot mass (m_3)	.77 kg
Shank mass (m_2)	.7 kg
thigh mass (m_1)	. kg
foot inertia (I_3)	. kg · m ²
Shank inertia (I_2)	. kg · m ²
thigh inertia (I_1)	. kg · m ²
Gravity (g)	. m/s ²

Table C.3 Anatomical joint limits used for the soft joint limit algorithm.

	hip flexion	hip abduction	Knee flexion	Ankle flexion
θ_{\max} (deg)				
θ_{\min} (deg)				

Author Contributions:

Josué García-Ávila: Conceptualization, Methodology, Investigation, Visualization, Writing- Original draft preparation, Software. **Cynthia Pamela González Gallegos:** Methodology, Investigation, Writing- Original draft preparation. **Erick Ramírez-Cedillo:** Methodology, Investigation, Formal Analysis, Review & Editing, Supervision, Resources. **Ciro A. Rodríguez:** Supervision, Review & Editing, Project administration. **Adriana Vargas-Martínez:** Supervision, Project administration. All authors have read and agreed to the published version of the manuscript.

Acknowledgments:

The authors would like to acknowledge support from CONACyT for Master studies of first author (scholarship number 1002683) and nTopology for providing access to research and academic licenses.

Declaration of conflicting interests:

The Authors declares that there is no conflict of interest.

Funding:

This research was funded by Tecnológico de Monterrey and Mexican National Council for Science and Technology (CONACYT) and J.G.-Á. MSc studies (scholarship number 1002683).

Publication:

The entire content of this section is being reviewed and prepared for future publication, some of the content has been previously presented as the results of master's thesis research titled “*Design and Additive Manufacturing of a transtibial prosthesis socket via powder bed fusion*” presented by Cynthia Pamela González Gallegos, URI: <https://hdl.handle.net/11285/643388>.

Declarations:

The results presented in this review are based on methods published in detail in the literature. We refer the reader to the original work for more details of each method applied. Important parameters for reproducing the results are described in the manuscript. The code used is available on request from the corresponding author.

CHAPTER 3: E-Skin Development and Prototyping via Soft Tooling and Composites with Silicone Rubber and Carbon Nanotubes.

Abstract	68
1. Introduction	69
2. Materials and Methods	71
2.1. Artificial Skin Design	71
2.2. Different Formulations with Varying Materials for Nanocomposites	72
2.3. Nanocomposite and Substrate Fabrication	73
2.4. Microelectrode Fabrication and Assessment	73
2.5. Soft Tooling Manufacturing Using Stereolithography-Based Additive Manufacturing	74
2.6. Mechanical Characterization	74
2.7. Hyperelastic Model Based on Mullins Effect	75
3. Results and Discussion	75
3.1. Nanocomposite and Substrate Fabrication	75
3.1.1. Challenges Associated with the Processing of SWCNT Nanocomposites	75
3.1.2. Defect Inspection of Nanocomposite Micropatterned Layers	76
3.1.3. Surface Resistance Measurements Results	78
3.2. Uniaxial stress-strain Behavior and Mullins Effect	79
3.3. Design Guidelines for AM-Based Soft Tooling	80
4. Conclusions and Future Work	81

Abstract

The strategy of embedding conductive materials on polymeric matrices has produced functional and wearable artificial electronic skin prototypes capable of transduction signals, such as pressure, force, humidity, or temperature. However, these prototypes are expensive and cover small areas. This study proposes a more affordable manufacturing strategy for manufacturing conductive layers with 6×6 matrix micropatterns of RTV-2 silicone rubber and Single-Walled Carbon Nanotubes (SWCNT). A novel mold with two cavities and two different micropatterns was designed and tested as a proof-of-concept using Low-Force Stereolithography-based additive manufacturing (AM). The effect SWCNT concentrations (3 wt.%, 4 wt.%, and 5 wt.%) on the mechanical properties were characterized by quasi-static axial deformation tests, which allowed them to stretch up to $\sim 100\%$. The elastomeric soft material's hysteresis energy (Mullins effect) was fitted using the Ogden–Roxburgh model and the Nelder–Mead algorithm. The assessment showed that the resulting multilayer material exhibits high flexibility and high conductivity (surface resistivity $\sim 7.97 \times 10^4 \Omega \text{ sq}$) and that robust soft tooling can be used for other devices.

Keywords: additive manufacturing; electronic skin; Low-Force Stereolithography; room-temperature-vulcanizing; RTV; single-walled carbon nanotubes; soft tooling; stereolithography; SWCNTs.

1. Introduction

The artificial recreation of tactile sensing is vital for developing more natural interaction between robots and the environment. Synthetic recreation in this sense could enhance remote online interactions and ultimately be part of a fully regenerative medicine scheme for limbs or other body parts. The development of electronic artificial skin or e-skin is a complex problem that deals with diverse sciences and disciplines, including electronics (soft robotics, wearables, haptic actuators, and neuroprosthesis control), bioengineering and materials sciences (tissue regeneration, personalized medicine, biosensors), and manufacturing (polymer solution casting, inkjet printing) [146], [147], as can be seen in Figure 1a. New materials and manufacturing procedures have enabled the production of larger and more sensitive surface areas [148]. The structure of human skin has inspired researchers to recreate the functionality of these tissues using multilayered material structures. Artificially constructed tissues sense environmental conditions, such as humidity, pressure, or temperature [149], [150]. Furthermore, conditions such as pH, blood oxygen saturation, heart rate, blood pressure, and muscular or neuronal electrical activity have been monitored using artificial skin [151], [152].

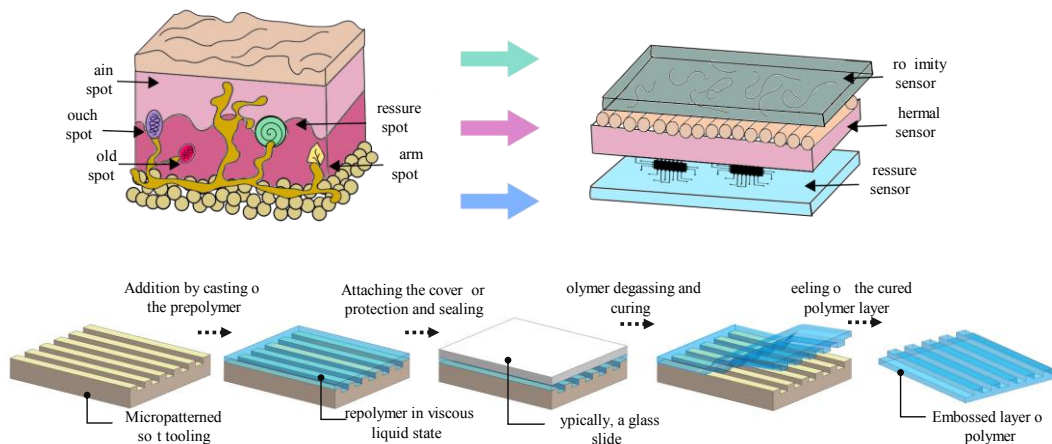


Figure 1. (a) Structure and sensing mechanisms of artificial electronic skin (right) and biological skin (left); (b) schematic illustration of the fabrication process of casting layers using soft tooling; (1) the first step is to clean the mold, (2) next, in the second step, the material is cast into the mold; (3) after coating and sealing via a protective substrate, the third step consists of degassing using some vacuum chambers and some negative pressure sources; finally, (4) curing is performed in a convection oven or other heat source prior removal.

There is a wide variety of transducers for sensing contact based on electromechanical, photoelectric, or electrochemical phenomena. These signals are generated in arrays of stacked materials (substrates and electrodes) regardless of the source. The substrates are mechanical foundations that support electrode layers that feature conductive properties that allow their sensing function. For instance, the electrodes are typically arranged in a 2D row–column matrix pattern creating overlapping intersections, which allows the generation of mutual capacitance between each pair of receivers (i.e., column) and transmitters (i.e., row); the capacitance sensitivity and detection range is intimately linked to the geometry of these electrodes.

Some of the polymers used to manufacture the substrates are based on polydimethylsiloxane (PDMS) [153], polyethylene terephthalate (PET), butyl rubber (IIR.), room-temperature-vulcanized silicone-rubbers (RTV) [154], and styrene-butadiene-styrene rubber (SBS) [155]. Electrodes are typically made from nanocomposites with conductive nanoparticles [156]. For example, Single-Walled Carbon Nanotubes (SWCNTs) embedded in PDMS thin films exhibit high sensitivity, fast response times, and

excellent stability [157]. Research about the synthesis of conductive R.T.V. silicone rubber composites layers with cross-linking of conductive fillers is limited to manufacturing processes such as Aerosol-Jet-Printing [158], or a more straightforward process to cast film samples [154], [159].

Additive manufacturing (AM) has played an essential role in manufacturing freeform flexible structures for biomedical devices. However, some scenarios are not feasible considering the limitations on the availability of materials or difficulties for post-processing the sample [160], especially for two-component silicones, such as the RTV-2 [161]. Indirect development using soft tooling (molds) produced using additive manufacturing has emerged as a cost-effective, scalable, customizable manufacturing alternative [162], [163] for such cases. This approach reduces manufacturing times, can be adapted to low-scale production scale, and has proven helpful in early production or new product prototypes [164]. Modern additive manufacturing processes, such as stereolithography (SLA), allow the production of soft tools with high precision and dimensional resolutions [165]. Although these are made from polymers, new ceramic and metallic metal printing advances are emerging. These options can improve curing times or enable new features. The flexibility of manufacturing devices with three-dimensional features can enhance the throughput for the early steps of the product life cycle. For example, different patterning cavities enable the generation of different device elements with fewer manufacturing steps. Developing and testing multi-cavity and multi-purpose soft tooling design methodologies can bolster artificial electronic skin manufacturing processes.

In recent years, soft tooling has evolved to develop configurations with more complex and intricate mold geometries. Standard geometries encountered are conical pillars (needles), rectangular or square prisms, cylindrical pillars, or tetrahedral pillars [166], [167]. Geometries that do not feature a taper experience adhesion problems that cause damage during peeling off. Some recommended techniques include the use of draft angles, rounded edges, and reducing the surface roughness of the mold [168]. A typical manufacturing process of artificial electronic skin is divided into four simple consecutive steps (see Figure 1b). However, the inherent difficulties associated with additive manufacturing using vat photopolymerization include processing times that are typically long and result in diminished thermo-mechanical properties [169]. Hence, soft tooling requires that the mold withstand the stress produced by heat and forces during manufacturing. Furthermore, while S.L.A. printing resolution excels among AM technologies, the build volume (working space of the devices) is smaller than that of more traditional technologies, such as Fused Deposition Modeling (FDM) [170].

There are diverse approaches to characterize the effect of carbon nanotube polymerization kinetics, including the presence and concentration of catalyzers [171], the piezoelectric performance [172], and the heat transfer response [173]. Reviews of CNTs published recently demonstrate the vast scope of the topic [174], [175]. Room-temperature-vulcanizing silicone (RTV-2) is a low-molecular-weight dimethyl polysiloxane-based rubber that can be cured without an external energy heat source and is widely used in sealing applications in the automotive industry, medical prosthetics, and electronic encapsulation. The development of e-skin based on RTV materials has been reported previously, but the manufacturing conditions have not been tested thoroughly.

One of the most critical steps during the production of silicone-based products is degassing, since it eliminates all the bubbles formed during the mixing stage. However, bubbles can appear during the casting of the material in open molds; some have explored the technique of centrifugal casting in closed molds [176] or the development of low-cost automatic vacuum casting systems [177]. In the case of nanocomposites based on RTV silicones, the temperature becomes another relevant variable because it accelerates the curing process and reduces the time available for the vacuum degassing process. However, the nanocomposite viscosity increases because of premature curing and the inclusion of SWCNTs. According to Vakili-Nezhaad et al. [178] the viscosity is increased up to 32.94% at a weight fraction of 0.2%. It is essential to characterize the effect of the conductive matrix because the mechanical

and electrical properties of the composite depend on their ratio. Another element to consider is the methodology for mixing the CNT with the matrix. Kundalwal and Rathi recently studied the effects of ultrasonic processing and magnetic stirrers for a dual mixing strategy for multiwalled carbon nanotubes (MWCNTs) [179].

In work reported previously, we showed that Low-Force Stereolithography (SLA-LF), a variation that employs a flexible V.A.T. tank to reduce the forces exerted on parts during the manufacturing process, could produce polydimethylsiloxane (PDMS) casting molds [163]. The aim of this study is threefold: first, we want to gain new insight regarding the manufacturability of molds for nanocomposites; second, we would like to assess the effect of the organic filler on the mechanical properties and conductivity properties for a nanocomposite; and finally, we would like to generate a framework for future robust design of molds. This study is of relevance because it addresses limitations from the manufacturing point of view.

To fulfill these objectives, we first conducted an experimental study of additive manufacturing with an initial mold design (an assay on the fabrication of layer RTV-2 and SWCNT-based nanocomposite structures) and modeled their mechanical properties. Next, with the insights provided by the study and a reexamination of existing research, we proposed design guidelines for the AM-based soft tooling of nanocomposite-based devices.

The methodology followed in this study provides insights and technical considerations that can be useful for the design of an alternative cost-effective rapid manufacturing methodology. Multi-cavity and multi-purpose soft tooling could be a resource to accelerate the manufacturing and sample testing processes.

2. Materials and Methods

2.1. Artificial Skin Design

The flexible sensor proposed here is a laminated structure with an active sensing area of 25.4 mm × 25.4 mm (cavity size) conformed by 64 individual electrodes (see Figure 2a). The sensing can be achieved using the nanocomposite material SWCNTs/RTV-2 to create a highly conductive array. While the outer and intermediate layers are made of elastomeric material, an external multiplexed data acquisition circuit is connected to each row (i), and column (j) of the conductive layer array (see Figure 2b). The topology of the array determines the spatial pressure resolution of the e-skin. The large deformation and flexibility of the nanocomposite makes it possible to vary the area of overlapped electrodes in the stacked layers. A change in capacitance due to deformation by an external force can be detected using the circuitry. Furthermore, the ability of these sensors to measure shear stress (σ_s) in addition to normal stress (σ_n) is a significant advantage. Although capacitive sensors require sophisticated electronic components, they have been found to provide greater sensitivity and flexibility, less dependence on temperature, more robust structures, low power consumption, better frequency response, and superior dynamic range compared with piezoresistive devices [180].

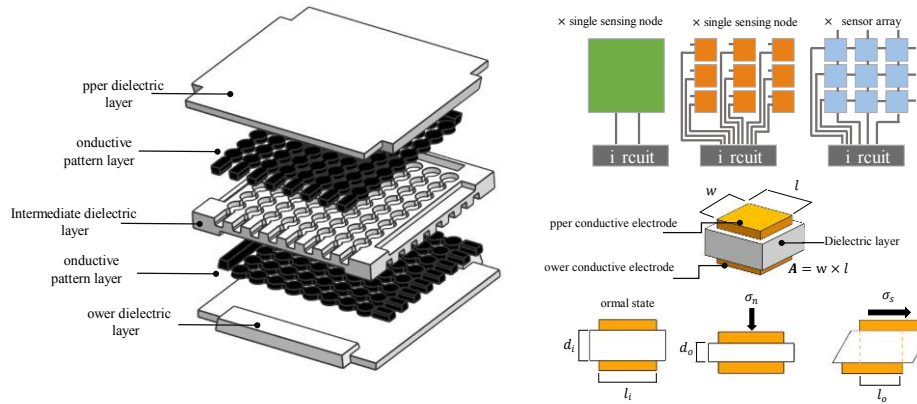


Figure 2. (a) Schematic illustration of the proposed all-elastomeric skin-like pressure sensor array; (b) conceptual topologies diagrams of array sensor; (c) principle of operation to measure normal and shear stress.

2.2. Different Formulations with Varying Materials for Nanocomposites

ELASTOSIL[®] P 7600 and ELASTOSIL 7683 RTV polymers (Wacker Chemie AG, Adrian, MI, USA) were tested on this work. The properties reported by the manufacturer are shown in Table 1.

Table 1. Physical and mechanical properties of the elastomeric matrix base material.

Property	ELASTOSIL [®] 7600	ELASTOSIL [®] 7683
Density	0.99 g/cm ³ (A) 1.05 g/cm ³ (B)	0.99 g/cm ³ (A) 1.05 g/cm ³ (B)
Viscosity	4000 mPa·s (A) 2000 mPa·s (B)	1400 mPa·s (A) 4000 mPa·s (B)
Pot life	27 min	40 min
Color	Translucent	Translucent
Hardness (Shore 00)	26	25
Elongation at break	600%	500%

Nanofiller contents (%) were prepared (Sample I, Sample II, and Sample III) (see Table 2). The RTV produced by the manufacturer (Wacker Chemie AG, Adrian, MI, USA) comprised parts A and B and were mixed in a 1:1 ratio. To form the nanocomposite, carbon Sussuba IITM Matrix (>7 carbon nanotube content, diameter 1.6 ± 0.4 nm, and G/D >100, Columbus, OH, USA) was used.

Table 2. Nanocomposite composition, wt. % Sussuba IITM Matrix sample preparation (g).

Component	Sample I Weight, g (3 wt.%)	Sample II Weight, g (4 wt.%)	Sample III Weight, g (5 wt.%)
Sussuba II TM Matrix 601	3.6	4.8	5.0
RTV-2 part A	58.2	57.6	57.0
RTV-2 part B	58.2	57.6	57.0

2.3. Nanocomposite and Substrate Fabrication

The process flow for the fabrication of the SWCNTs/RTV-2 nanocomposite for tensile specimens and micropatterns layers is shown in Figure 3. Part A and Substrate II™ Matrix were pre-mixed using a mechanical stirrer at 1000 revolutions per minute (RPM) for 15 min. Next, the curing agent (RTV-2 part B) was added and stirred (15 min and 1000 RPM). Finally, the sample was moved into a vacuum chamber for deaeration using a vacuum oil pump with a 5 ft³m⁻¹ displacement speed (25 μmHg for 5 min). Through visual inspection, care was taken to assure that bubbles were not present in the specimens.

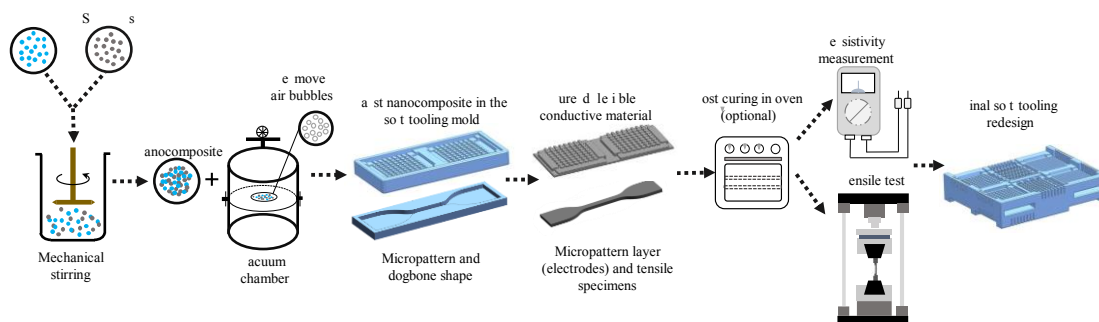


Figure 3. Schematic illustration of the assessment process for nanocomposites RTV-2/SWCNTs.

2.4. Microelectrode Fabrication and Assessment

All the molds (including the tension specimens; Figure 4a, green box) were designed using Siemens NX 12. On the other hand, the molds with microgeometry presented in Figure 4b were first manufactured with two cavities with 2 mm circular micropatterns and the third mold with 2 mm hexagonal microgeometry; their relevant geometric details can be seen in Figure 4c. The overall sizes of these two-cavity soft tooling and specimen tensile molds were 67.8 mm × 30.92 mm × 7 mm and 107 mm × 31 mm × 5.5 mm, respectively. The molds were printed with their larger side parallel to the print bed.

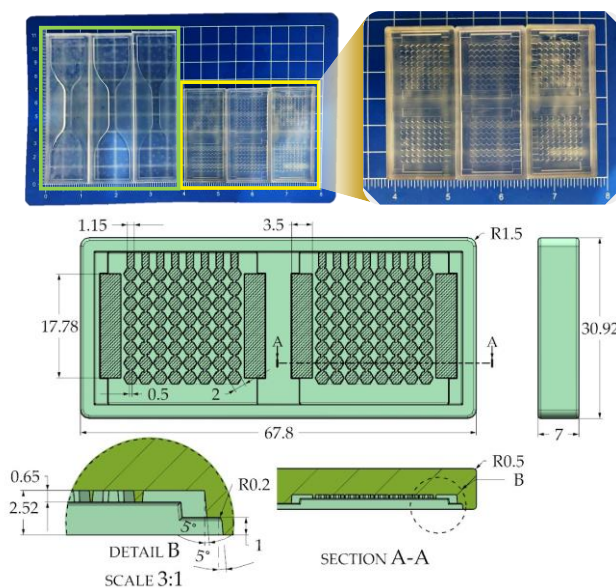


Figure 4. (a) Photos of three molds for tensile specimens (green box) and three initial two-cavity molds (yellow box) printed by Low-Force Stereolithography (x- and y-units show dimensions in inches and

centimeters respectively); **(b)** detail of two molds with hexagonal micropattern and one mold with circular micropattern (40% modified contrast); **(c)** overall dimensions of the hexagonal pattern geometry and soft tooling cavities (all dimensions in mm).

2.5. Soft Tooling Manufacturing Using Stereolithography-Based Additive Manufacturing

A benchtop SLA-LF Form 3 additive manufacturing equipment (Formlabs, Somerville, OH, USA) was used, employing a 50 μm for the high-temperature FLTHAM02 for manufacturing all the molds in this paper. The samples were cured using the provider's recommended settings or post-processing the sample accordingly (120 min at 160 $^{\circ}\text{C}$) on a hot plate.

2.6. Mechanical Characterization

To test the mechanical properties of the materials and compare them for different nanocomposite compositions, tensile tests were conducted.

The tensile tests were performed based on a standardized method considering a Type 1A specimen with an overall length of 100 mm and a 3 mm thickness, which met all the specifications listed standard ASTM D412-16 (2021) [181]. A universal testing machine (3365, INSTRON, Norwood, MA, USA) equipped with a 50 kN load cell was used, considering a crosshead speed of 500 mm/min. Three specimens of each type of continuous pure material and assessed composition (Sample I, Sample II, and Sample III) were loaded axially and monotonically at a speed deformation of 0.3 mm/s until complete failure. Next, loading-unloading uniaxial cyclic tests were performed at three different maximum strain levels ($\epsilon = 4, 3, 2$) for 10 continuous cycles. After the first couple of load cycles, the material stress-stretch response become repeatable [182].

The experimental results of the loading-unloading tests were fitted via inverse analysis with predicted data curves based on the Ogden-Roxburgh model using the Nelde-Mead optimization algorithm, as suggested in [183] and described in section 2.4. The fitting step was intended to optimize the Ogden-Roxburgh model. The coefficient of determination R^2 was calculated for the predicted results and compared to the experimental data for every iteration step. These values are then summarized as the descriptor for the objective minimization function for the next iteration step of a Nelder-Mead optimization loop [184].

To monitor the temperature during the mixing of the elements of the nanocomposite parts, a 640×480 pixel Flir ONE thermal imaging camera (Teledyne FLIR LLC, Wilsonville, OR, USA) was used.

A visual inspection of the features of the microelectrodes was performed using an S.Z.M. AmScope stereoscopic microscope (United Scope L.L.C., Irvine, CA, USA). The quality inspection of the defective single electrodes of each 8×8 matrix array was performed via a nonparametric Kruskal-Wallis test with multiple pairwise comparisons between groups. Considering the variability of possible defects between different concentrations of SWCNTs, distribution symmetry was not assumed, and the median was calculated instead of the mean. Pairwise differences between treatments were assessed using the Dunn-Bonferroni method, and the significance level α was 5%. All the statistical analyses were performed in SPSS[®] Statistics version 28.0.1.

To corroborate the surface electrical conductivity, samples of $15 \text{ cm} \times 15 \text{ cm}$ and 3 mm thickness were prepared with the nanocomposite types I, II, and III. These samples were screened on an analog DESCO model 19,784 surface resistance meter (Desco Industries Inc., Chino, CA, USA). This is a portable device that produces a signal if a resistance higher than $10^5 \Omega$ is detected. The methodology employed to measure the resistance was point-to-point (RTT, or Resistance Top to Top).

Surface resistivity ρ_s is a physical property of a material and the surface resistance R_s (also known as sheet resistance) depends on the material and the geometry of the electrodes (probes) used in the measurement. To differentiate between them, ρ_s is often expressed in $\Omega \text{ sq}$. The relationship between both characteristics according to standard ASTM D257 [185] for circular electrodes is:

$$\rho_s = \frac{\pi \times D \times R_s}{g} \quad \text{Equation}$$

where g is the gap between the electrodes and D is the diameter of the electrodes.

2.7. Hyperelastic Model Based on Mullins Effect

This strain-softening phenomenon (also called the Mullins effect) presented in the elastomeric matrix was predicted using the Ogden–Roxburgh hyperelastic constitutive model [186], which defines isotropic incompressible materials' strain energy function $W(\lambda_i, \eta)$ under quasi-static loading. Several works have successfully used this phenomenological model to obtain a predictive model for high-strain elastomeric soft materials [187], [188]. To compare the model with our available experimental results, we considered the simple uniaxial loading case, in which the principal stretches ratio are $\lambda_1 = \lambda$, $\lambda_2 = \lambda_3 = \lambda^{-1/2}$; we also write $\sigma_1 = \sigma$, $\sigma_2 = \sigma_3 = 0$. Next, the adapted strain energy function can be expressed as:

$$W(\lambda, \eta) = \eta W_0(\lambda) + \phi(\eta) \quad \text{Equation}$$

$$W_0(\lambda) = \sum_{i=3}^{N=3} \frac{\mu_i}{\alpha_i} (\lambda^{\alpha_i} + 2\lambda^{-\frac{1}{2}\alpha_i} - 3) \quad \text{Equation}$$

where $W_0(\lambda)$ is the original stress-energy function based on the classical Ogden nonlinear elastic model ($N = 3$), and $\phi(\eta)$ is a smooth energy damage function that depends on the scalar damage variable η evolving towards softening, as expressed using a Gaussian error function:

$$\eta = 1 - \frac{1}{r} \operatorname{erf} \left[\frac{W_{\max} - W_0}{m + \beta W_{\max}} \right] \quad \text{Equation}$$

where r , m , and β are material-dependent dimensionless parameters, r (always $r \geq 1$) is a measure of the extent of the damage relative to the virgin stress-strain behavior, m (always $m \geq 0$) defines the dependence of the damage phenomenon on the extent of deformation and β (always $\beta \geq 0$) specifies the slope of the softening curve compared to the initial loading curve, and W_{\max} is the maximum strain energy potential function over the range deformation history. In our case, the calibration process for a three-order Ogden–Roxburgh ($N = 3$) prediction ensured an adequate match between the predicted equation and the stress response of the experimental data. As in the polynomial form approach, there is no limitation on the parameter N . A higher value may provide a better fit for the exact predicted solution. However, on the other hand, it may cause numerical difficulty in computational consumption when fitting the material constants and requires enough data to cover the entire deformation range of interest. Therefore, a value of $N > 3$ is not usually recommended. This latter procedure was performed using parameter-extraction software, namely MCalibration[®] 6.5.1 by PolymerFEM [189] with integrated internal Ansys and Abaqus solvers.

3. Results and Discussion

3.1. Nanocomposite and Substrate Fabrication

3.1.1. Challenges Associated with the Processing of SWCNT Nanocomposites

Single-Wall Carbon Nanotubes (SWCNTs) are highly effective additives for improving polymer-based material conductivity. However, the attractive Van der Waals interactions between SWCNTs result in them agglomerating. Ideally, we must disperse separate nanotubes into the base material to achieve optimum strengthening and electrical conductivity. The tuba II™ Matrix highly concentrated masterbatch (SWCNTs homogeneously dispersed in polydimethylsiloxane PDMS) used in this work facilitated the well-dispersed of nanotubes loading fractions into the RTV-2 matrix in our sample with high concentrations (up to 5 wt.%). In this context, Pötschke et al. [190] reported that nanocomposites containing <2 wt.% nanotubes exhibited Newtonian behavior, quite similar to that of the unfilled matrix. This SWCNT-based masterbatch also avoided a widespread problem at the time of scalability of the product, especially the level of percolation threshold required to achieve adequate electrical conductivity in the nanocomposite with low concentration (2 wt.%).

However, the increase in viscosity of the masterbatch can limit the diffusion and sedimentation of *SWCNTs* by restricting the Brownian motion. According to the manufacturer, the best compatibility using the dilution process via a high-speed overhead stirrer is achieved with R.T.V. with low-viscosity (up to 50,000 mPa·s) and not more than 2 wt.%. Experimental data show that these results can be achieved even at higher concentrations without a pre-dilution process. Consequently, the cross-linking and viscosity are greatly accelerated with increasing temperatures, so the heat generated during mixing must be strictly controlled. This viscosity condition can be make it challenging to process nanocomposite during the final casting in soft-tooling and can cause high porosity levels, as shown in Figure 5a. However, RTV-2 features low surface tension, which also allows an excellent molding pattern replication.

On the other hand, the pot life of the elastomers used in both cases, which usually indicates the maximum period during which the catalyzed mixture of part A and part B is processable (or during which the initial viscosity doubles its value), did not exceed 1 h. Nevertheless, the presence of exothermic enthalpy of PDMS from the masterbatch caused its nanocomposite to reduce the pot life in the samples with 5 wt.% loading fractions. Figure 5b shows the peel-off substrates after the supplier's pot life and the curing phenomenon's alteration.

3.1.2. Defect Inspection of Nanocomposite Micropatterned Layers

The concentration of SWCNTs and temperature can significantly modify the rheological properties of SWCNT OCSiAl masterbatch concentrations that exceed 1 wt.% [191]. For this paper, the concentrations of SWCNTs could cause air-trapped defects in the soft tooling electrodes shapes due to the high viscosity; however, it is feasible to process the samples in sheet form without these defects occurring, as can be seen in Figure 5c. While we were able to achieve a free-solvent homogeneous nanocomposite mixture, the mechanical work of the stirrer increased the temperatures by about 50 °C. One way to mitigate the heat transfer was to employ a cold-water bath. Figure 6 shows that employing this method made it possible to maintain a constant temperature, around 17 °C.

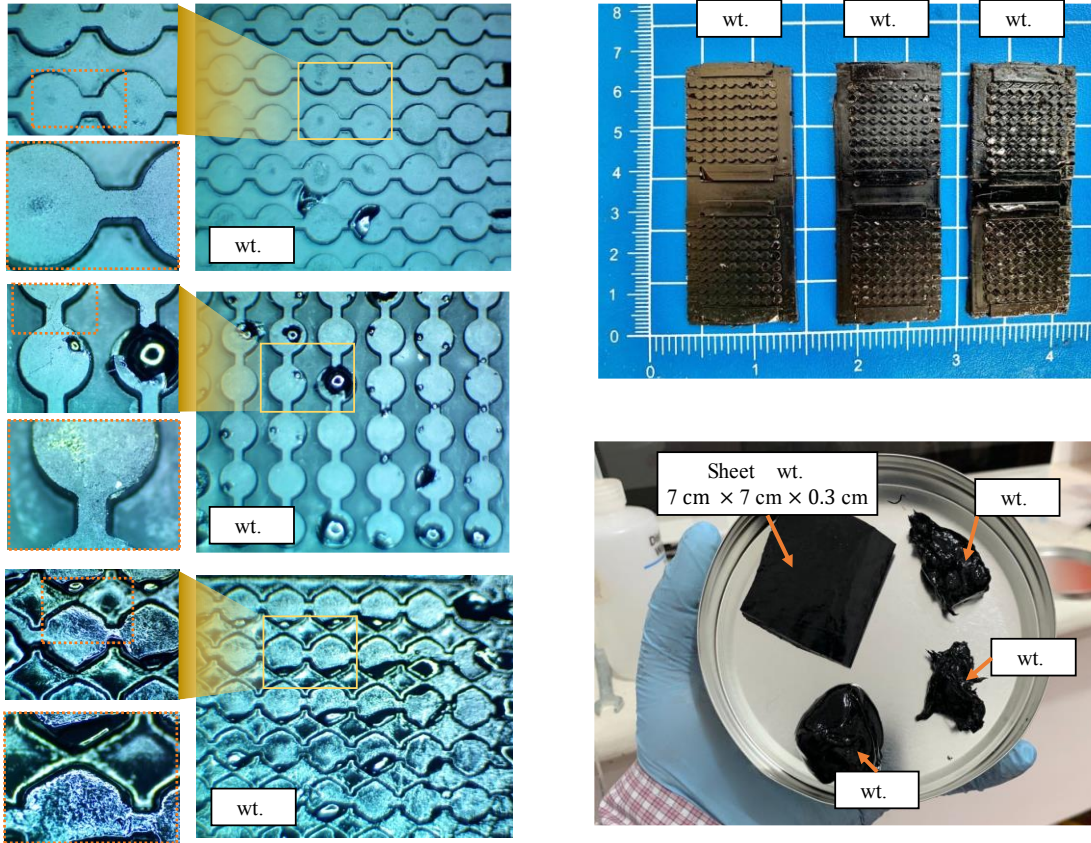


Figure 5. (a) Images from an optical microscope to inspect the definition of edges and defects in the patterns for different concentrations of nanotubes; (b) results obtained from peeling off without transverse detachment of the samples; (c) consistency of the viscous mixtures for different concentration of nanotubes.

The inspection of the defective electrodes in the micropatterned layers manufactured during this study o caused by SWCNT concentrations in the three groups ($k = 3$) with different filler concentrations was considered entirely independent; the test is based on the null hypothesis H_0 on the median ($\tilde{\mu}$) of the number of defective electrodes that assumes $\tilde{\mu}_1 = \tilde{\mu}_2 = \tilde{\mu}_3$ against the alternative hypothesis H_1 , where at least one median is different from the rest. The test statistic K was used, which followed a behavior comparable with the chi-square distribution (χ^2) with $k-1$ degrees of freedom. According to the results shown in Table 3 for significance level ($\alpha = 0.05$), the null hypothesis was rejected (p -value < 0.05), so there was sufficient statistical evidence to rule out the possibility that the three medians were equal. The pairwise comparison between the study groups with different concentrations of SWNTs corroborates that all the medians were different for each of the study groups (Table 4).

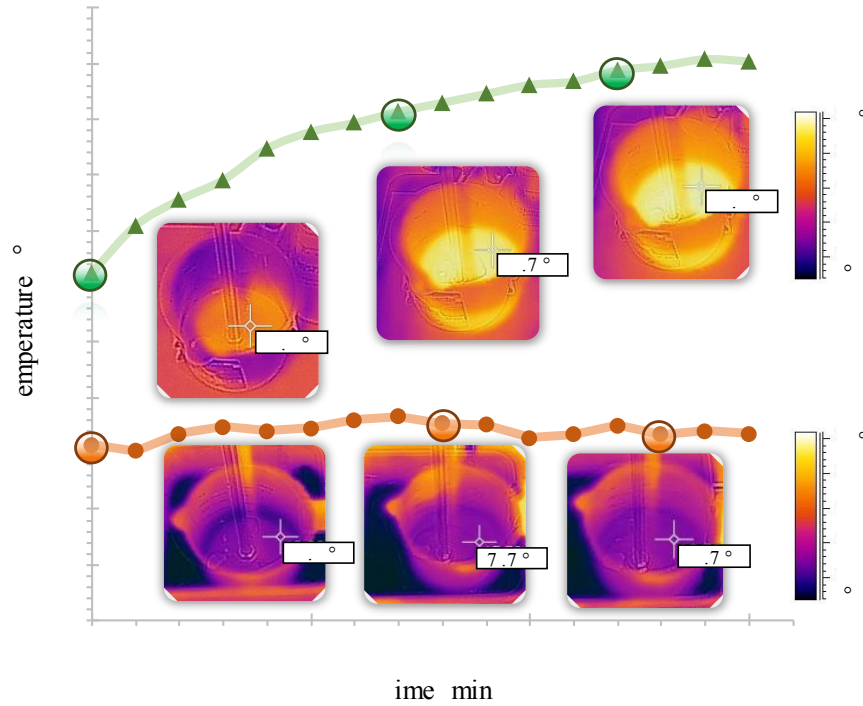


Figure 6. Temperature monitoring over 15 min in mixing processes assisted with and without a reverse bain-marie; the manu acturer’s recommended temperature is $< \text{ }^\circ$.

Table 3. Independent samples Kruskal–Wallis test summary.

Group	N	Median	Mean Rank	Z-Value
3 wt.%	12	8.0	6.3	– .
4 wt.%	12	11.5	19.1	0.23
5 wt.%	12	14.5	29.8	4.56
Total N	36	-	18.5	-
Method		DF	K-Value	p-Value
Not adjusted for ties		2	29.27	0.00000044
Adjusted for ties		2	29.65	0.00000036

Table 4. airwise comparison results using Dunn’s nonparametric post-hoc test.

Samples	Test Statistic K	Std. Error	Std. Test Statistic	p-Value	p-Value *
3 wt.%–4 wt.%	– .	4.274	– .	0.003	0.010
3 wt.%–5 wt.%	– .	4.274	– .	<0.001	0.000
4 wt.%–5 wt.%	– .7	4.274	– .	0.012	0.036

* Significance values were adjusted by the Bonferroni correction for multiple tests.

3.1.3. Surface Resistance Measurements Results

Our procedure required the use of two 5 lb cylindrical probes with a diameter $D = .75$ (1.91 cm) and a distance g of 2.5 cm, placing the nanocomposite material to be tested on an insulative surface, and performing the measurements in orthogonal directions, i.e., moving the probes to measure in a cross

direction and repeating the test. This is a simple go/no-go procedure to evaluate the presence of high electrical conductivity in the nanocomposite. All the samples manufactured yielded a value of $\rho_s \sim 7.97 \times 10^4 \Omega \text{ sq}$ using Equation . Conductive materials have a surface resistivity of less than $\times 10^5 \Omega \text{ sq}$. On the other hand, the volume resistivity (also known as bulk resistivity, specific electrical resistivity, or bulk resistivity) ρ_v (in $\Omega \cdot \text{cm}$) can be calculated by multiplying the surface resistance R_s by the sample thickness (in cm): $\rho_v = R_s \times t$; in our case, $\rho_v \sim 2.39 \times 10^4 \Omega \cdot \text{cm}$.

3.2. Uniaxial stress-strain Behavior and Mullins Effect

Figure 7a shows the stress-strain experimental data records under true uniaxial stress for the pure substance. The mean elongation break was registered at $\bar{\epsilon} = 441.075\%$ and 643.542% . The data were mostly consistent with the behavior predicted by the datasheet of 500%, 600% for ELASTOSIL[®] 7600 and 7683 material, respectively. Figure 7b shows that with higher nanotube concentrations, the stress value for the failure point increased to 0.306 MPa (3 wt.%), 0.406 MPa (4 wt.%), and 0.465 MPa (5 wt.%). Figure 7c,d reveals that the pure elastomeric material exhibited a level of dissipated energy hysteresis, known as the Mullins effect, during cycling loading for three different stretch ratios $\lambda = \{ \dots \}$, where the strain equals the stretch minus unity ($\epsilon = \lambda - 1$).

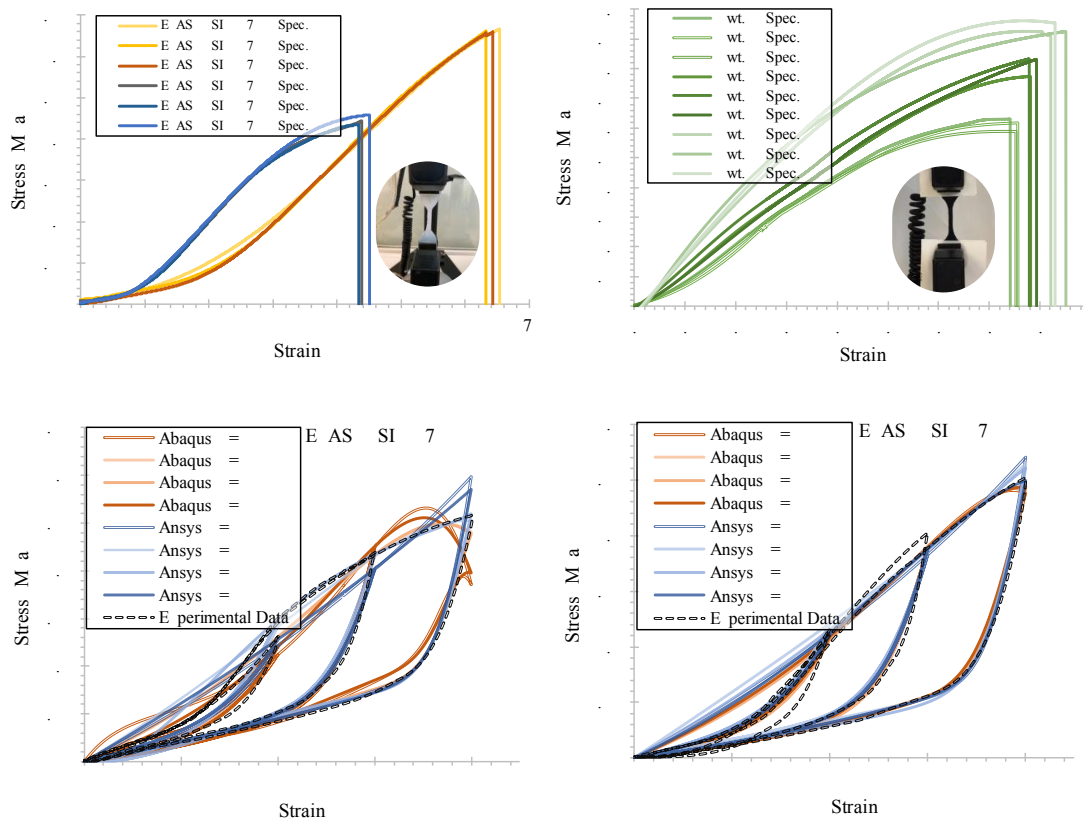


Figure 7. (a) Stress-strain curves of uniaxial tension test subjected to quasi-static axial loads of RTV-2 material and (b) RTV-2-based nanocomposite filled with different concentrations of SWCNTs; hysteresis curves of uniaxial stress loading and unloading on material ELASTOSIL[®] 7600 (c) and 7683 (d).

The Nelder–Mead optimization method and the Abaqus and Ansys solvers were used to calculate the parameters β , μ and α ($i = 1, 2, 3$) listed in Table 5. A three-order Ogden–Roxburgh model fit with

$R^2 \sim 0.87, \sim 0.92$ of the Mullins effect of an ELASTOSIL[®] 7600 and 7683, respectively. The parameters of the full Ogden-Roxburgh model summarized in Table 5 characterize the elastic strain energy of Equation 3. With this fast optimization method, fit curves were achieved before 3000 iterations (number of function evaluations); the R^2 values were evaluated and compared in a range of $N = \{3-6\}$ (see Table 6). The full numerical predicted curves for different systems of grade N are also given in Figure 7c,d.

Table 5. Summary of constitutive constants provided by the calibration process numerical solution-based solvers for Ogden–Roxburgh model ($N = 3$) via Ansys (right) and Abaqus (left) solvers.

Property	ELASTOSIL [®] 7600		ELASTOSIL [®] 7683	
	μ_1 [MPa]	–	0.024	1.65×10^{-1}
μ_2 [MPa]	–	0.049	0.013	0.021
μ_3 [MPa]	0.079	0.061	3.74×10^{-1}	0.017
α_1 [–]	1.396	0.226	1.733	0.271
α_2 [–]	1.322	0.266	0.571	0.345
α_3 [–]	–	0.267	–	0.372
r [MPa]	1.589	1.581	1.374	1.383
m [MPa]	0.120	0.119	0.124	0.120
β [MPa]	3.36×10^{-1}	2.27×10^{-1}	8.74×10^{-1}	1.67×10^{-1}

Table 6. Summary results of coefficient of determination (R^2) for Ogden–Roxburgh model using Ansys (right) and Abaqus (left) solvers and Nelder–Mead algorithm.

N	ELASTOSIL [®] 7600		ELASTOSIL [®] 7683	
	3	0.865	0.871	0.921
4	0.883	0.889	0.922	0.912
5	0.894	0.897	0.916	0.921
6	0.865	0.871	0.921	0.918

3.3. Design Guidelines for AM-Based Soft Tooling

This paper’s redesign of the multi-cavity mold was approached from 10 different aspects, based on lessons learned during experimental development. The design process involved analyzing these aspects before and during the definition of the final rubout design. Although the list of the 10 aspects is not exhaustive, they tackle the sources of issues for this purpose. These specific guidelines are based on more general principles of the robust and reliability-based design optimization methodology and from the exhaustive review of lessons learned from scientific research in the field of soft tooling [192].

1. Definition of requirements and limitations. Define the overall dimensions of the multilayer structure of the artificial skin, the thicknesses of the layers independently, the quantities of layers to be assembled, the required quality standards (e.g., surface roughness), the number of cavities and cores, the volume of production, material selection, critical specifications, and geometric tolerances [193].
2. Design of the topology of the replicated structure. Define the size and depth of the conductive microchannels, the shape of the geometry engraved in the mold, the spatial orientation, distance to the cavity edges, draft angles, and rounding in intricate corners.
3. Design of the alignment system. Define the type of alignment (geometric, magnetic, mechanical, etc.), pin dowel material, locking units, and complete restriction of the six D.O.F.

4. Design of machine structure. Define the rigid mold carrier, mold support frame, ejector pins, and rigidity on the support surface; consider the effects of external forces (e.g., gravity), and available operating space.
5. Cavity design. Define cavity orientation, wall thicknesses, cavity spacing or interconnection, cavity tightness and sealing, projected surface, and cross-section design.
6. Runner-system design. Define the feeding ducts, the amount of material required per cycle, the injection or casting speed, runners, sprue, gates, cavity-nesting, reservoirs, reverberators, and computational simulations.
7. Sequential process design. Define the release agent and the surfaces with release angles; define the production cycle times, design the Process Flow Diagram (P.F.D.), SMED changes, process parameter variation, and tolerance stack-up analysis.
8. Thermodynamic process design. This includes the percentage of contraction or expansion, in-mold rheology, surface coatings, and hot zones required for special thermoregulation, melt temperature, and mold temperature [194].
9. Design considering the manufacturing process. Especially for additive manufacturing, the definition of mold impression orientation, placement of support and filler material and its interference with critical zones, the machine's capacity where the mold will be manufactured, the cross-section of internal ducts [195].
10. Accessories and various designs. Define spare parts and useful life, a preventive and corrective maintenance plan, mounting or transportation accessories, soft tooling release documentation, safety equipment for operability, and external environment factors [196].

4. Conclusions and Future Work

This study provided evidence that supports the employment of RTV and SWCNT for manufacturing E-skin micropatterns. The findings presented here provide a starting point for further examination of the application of the prototypes developed with the manufacturing methodology described. The conclusions are summarized as follows:

1. Fabricating multilayer materials such as artificial electronic skin via printed soft tooling by additive manufacturing is feasible for materials with properties similar to RTV-2 and SWCNT-based nanocomposites.
2. Using RTV-2 material casting into the mold cavities, we showcased the application of soft tooling in the development and prototyping stages with very promising scalability and a low production cost approach.
3. An Ogden–Roxburgh model was successfully implemented to analyze the energy dissipation of flexible materials with values greater than $R^2 > 0.86$.
4. We developed a set of guidelines for the AM-based soft tooling of e-skin.
5. We verified the electrical path of the S₁ and S₂' micropattern geometries with advantages that included low volumetric and surface resistivity.
6. Future work will focus on testing the assembly of the micropatterned layers and the ability to generate capacitive phenomena to detect the deformation of the electrodes. Furthermore, the application of the design guidelines and the effect on the performance of the device remains to be developed in the future.

Author Contributions:

Josué García-Ávila: Conceptualization, Data curation, Investigation, Visualization, Writing— original draft. **J. Israel Martínez-López:** Data curation, Resources, Supervision, Visualization, Review & Editing. **Erick Ramírez-Cedillo:** Formal Analysis, Methodology, Project Administration, Resources, Supervision, Visualization. **Ciro A. Rodríguez:** Conceptualization, Data curation, Validation, Review & Editing. **Adriana Vargas-Martínez:** Funding Acquisition, Review & Editing. All authors have read and agreed to the published version of the manuscript.

Acknowledgments:

The Research Group of Advanced Manufacturing from Tecnológico de Monterrey provided support for the acquisition of materials and goods. The authors would like to acknowledge support from Wacker Chemie AG and Wacker Mexicana S.A de C.V. for providing access to ELASTOSIL® material and Eduardo Guerrero from OCSiAl Group for his support during the conductivity measurement stage. Josué García Ávila acknowledges the grant support of the Mexican National Council for Science and Technology (CONACYT). The authors acknowledge the support from Centro de Investigación Numérica and 3D Factory.

Declaration of conflicting interests:

The Authors declares that there is no conflict of interest.

Funding:

This research was funded by Tecnológico de Monterrey and Mexican National Council for Science and Technology (CONACYT) and J.G.-Á. MSc studies (scholarship number 1002683).

Publication:

All the content of this section has been published under the title "E-Skin Development and Prototyping via Soft Tooling and Composites with Silicone Rubber and Carbon Nanotubes", DOI: 10.3390/ma15010256.

Data Availability Statement:

The data presented in this study are openly available in FigShare at <https://doi.org/10.6084/m9.figshare.c.5764694.v1>.

CHAPTER 4: Modeling of Soft Stretchable Nanocomposite using Recurrent Neural Networks.

Abstract	83
1. Introduction	84
1.1. Analogy-Based Learning and Data-Driven Learning of Dynamic Mechanical Systems	84
1.2. Objective	85
2. Methods.....	86
2.1. Sample Preparation	86
2.2. Testing Validation Method for Stretchable Materials.....	87
2.3. Fundamental System Identification and RNN Analogy	88
2.4. Baseline Numerical Mechanical Model and One-Step Approximation.....	89
2.5. Data Sets Experimental Data and Network Setup	90
3. Results and Discussion.....	91
3.1. Stress-strain Behavior, Mullins Effect and Strain Energy	91
3.2. Nanocomposite Ball Dynamics Tuning Experimental Data	93
4. Conclusions, and Future Work.....	95

Abstract

Human skin and biological tissues are characterized by ruga, elastic, and non-flat surfaces; consequently, smart soft materials are a promising option that allows sensing of the interaction of the skin-wearables or bioelectronics interfaces that could not be achieved with conventional rigid and integrated circuits that exist today in the electronics field. This paper presents the fabrication of flexible nanocomposite fabricated using PDMS (Polydimethylsiloxane) and SWCNTs (Single-Walled Carbon Nanotubes). We analyzed the mechanical nonlinearity data during uniaxial monotonic tensile test and elastic and dissipated energy during cyclic strain-stress deformation hysteresis process of the nanocomposite material at different conductive filler loading (0.5, 1, and 1.5 wt.%). We performed a benchmark data-driven implementation using three main families of vanilla recurrent neural networks cell architectures: Simple Recurrent Neural Networks (SRNN), Long Short-Term Memory (LSTM), and Gated Recurrent Units (GRU). The models were defined, trained, and tested to obtain the predictive sequence data of cycle-to-cycle no linear strain-stress curves and finite element simulations using a state-space models from a spring-mass dynamic system analogy. Other experimental data were obtained from two out-of-plane non-conventional deflection tests to demonstrate the squashing/squeezing and jumping/bouncing deformation mechanisms of soft materials using a two continuous bilayer with different loading filler. The results demonstrate the feasibility and high accuracy of the numerical and physics-informed constitutive model and hybrid approach of analogy-based learning and data-driven learning for the design and computational analysis of soft and stretchable nanocomposites materials.

Keywords: data-driven; physic-based models; deep learning: recurrent neural networks; flexible electronics; nanocomposite; PDMS, SWCNTs.

1. Introduction

Neural networks have been widely used for the identification of nonlinear dynamical systems and their state space models of different natures such as biological neurons [197], oscillators [198], autonomous vehicles [199], and even economic systems [200]. Therefore, there is great potential for application potential of neural network architectures for state space model identification mechanics models of soft materials (rubbers, soft tissues, biomaterials) to obtain better predictive data under large nonlinear deformation behavior. Previously, the authors have investigated the nonlinear large elastic response of RTV silicone and filler material SWCNTS (single-walled nanotubes) by fitting load-unloading curves using traditional parameter fitting algorithms for well-known models such as the Ogden-Roxburgh this type of viscoelastic soft materials [201]. Viscoelasticity is a time-dependent mechanical behavior that can be easily observed/measured in soft materials and is dependent on the current state of deformation and deformation history. Many years theoretical models have been used to describe the behavior of viscoelastic materials that balance elastic and viscoelastic behavior, usually represented by a spring and a damper (dashpot), respectively, e.g., Maxwell model, Kelvin-Voight model, Prony series or Standard Linear Solid model [202]. On the other hand, Recurrent Neural Networks (RNN) are well suited to process this type of time series data and are designed to hold past or historic information of sequential data. Undoubtedly, a hybrid approach of analogy-based learning and data-driven learning promises to be a great way to adapt mechanistic models of soft materials with complex time-varying behaviors.

1.1. Analogy-Based Learning and Data-Driven Learning of Dynamic Mechanical Systems

A conventional dynamical system involves a state-space model that can be defined a behavior in function of continuous-time t . The state of the system can be one or a set of different physical quantities (temperature, position, velocity, etc.) used to describe it behaviour in any instant of time. This promising idea has been well received for the design of multi-joint systems such as ankle-foot prostheses during a study of gait-cycle phases but also opens up the prospect for the study of multifunctional materials such as flexible conductive materials and their mechanical performance during the large deformation history. For simple problems, it is easy find an analytical solution to describe the state of the system via government equations and fit know parameters. For many of the nonlinear dynamic mechanical systems, an analytical solution cannot be found or is difficult to find, and instead solutions must be approximated or use analogy descriptors based on similar systems across length scales, a suitable example is the spring-damper model as shown in Figure 1.

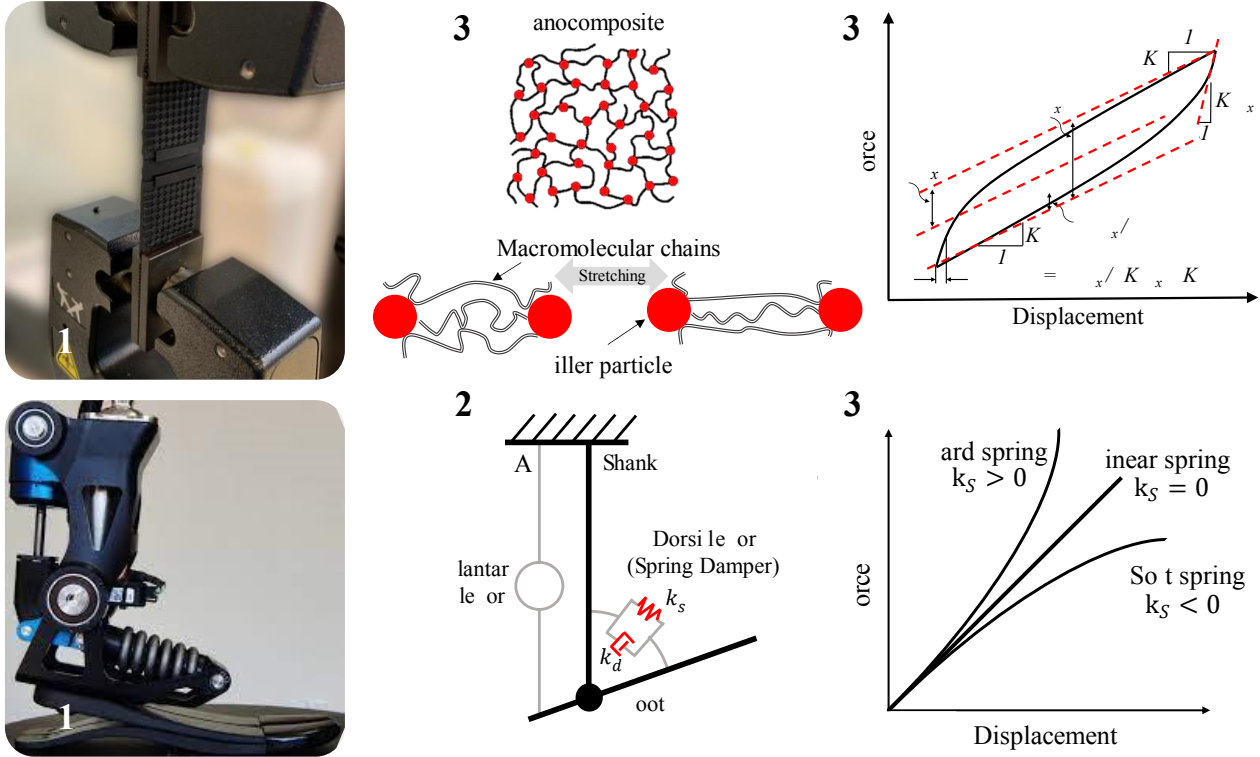


Figure 1 (a.1) Flexible material under twisting condition; (a.2) Cross-linked nanocomposite chains using spring-based interaction; (a.3) Uniaxial cycle response to show Mullins hysteresis effect behavior; (b.1) Powered ankle-foot prosthesis; (b.2) Compliant dorsiflexor model with spring-damper system in parallel configuration (k_s :elastic spring constant, k_d :dashpot viscosity constant), figure from [203]; (b.3) Curves of restoring spring force.

Traditional approximations, on the other hand, are frequently computationally expensive in terms of both time and processing power. Instead of these simulations, a data-driven learning-based approximation strategy can be used to generate superior results with learnt prediction models via neural networks. A recurrent neural network, for example, has several advantages, including the ability to process inputs of any length, the model's size not increasing with the size of the input, the calculation considering historical information and temporal dynamic behavior for time sequence data, and finally, the model learns faster if the gradient tends to have a more drastic variation [204]. Some authors have shown good results using RNN to predict the dynamic hysteresis of soft magnetic material [205] and nanocomposite piezo-resistive sensors fabricated from silicone rubber (Ecoflex) blended with carbon nanotubes (CNTs) [206].

1.2. Objective

In this paper, a data-driven computation simulations using the three classic recurrent neural networks (RNN) architectures and one-step approximation method for learning the input-output behavior of real dynamical viscoelastic response of soft nanocomposite materials are presented. Physics-informed schemes are incorporated in the loss function for optimizing the training and learning process for the time-varying dynamics of nonlinear stress-strain and Mullins effect curves. The nanocomposite was synthesized to obtain the flexible PDMS material with SWCNTs as material filler. The previous experience of the research group to fabricate flexible conductive materials is reflected in a mastered technique for using 3D printed molds by stereolithography that allows to obtain substrates and samples with well-defined geometric reliefs by soft tooling geometry without inhibiting polymer curing.

Three behaviors conditions are considered to obtain the data sets, the hysteresis loops of Mullins Effect, the uniaxial stress-strain curves, and two no conventional testing based on spring-damper system analogy. We performed a benchmark of the well-known vanilla recurrent neural network (RNN), see Figure 2, whose connection with dynamical systems is through interesting concepts such as effective increment in several k time steps via one-step discretization and state-space models. We introduce the concept of neural networks, and the surrounding concepts are presented that a neural network to approximate this effective increment, thus negating the need to have a known governing equation when determining the system to mechanically model the behavior of a soft material with nonlinear deformation.

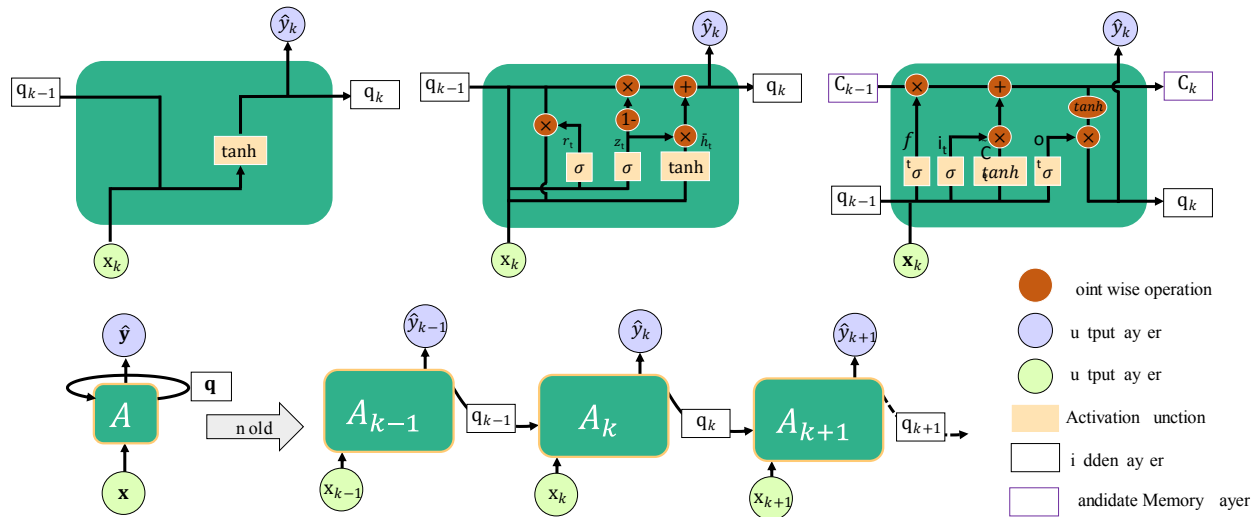


Figure 2. (a) Three types of vanilla Recurrent Neural Network cells: Simple Recurrent Neural Network (SRNN), Gate Recurrent Unit (GRU), and Long Short-Term Memory (LSTM); (b) A unfolded standard Recurrent Neural Network in repeating module.

2. Methods

2.1. Sample Preparation

We have followed the same methodology developed by the authors and documented in [201]. For this paper we have we have synthesis the nanocomposite using PDMS Sylgar 184 (Dow Corning, Midland, MI, SA) with ratio and uba ll™ Matri S s nanotubes (Sial, olumbus, , SA) at concentrations of 0.5, 1.0 and 1.5 wt.%. The nanocomposite was cast into 3D printed molds that do not inhibit curing to obtain 4 types of specimens as listed in Table 1.

Table 1. a nocomposite . . . wt. uba ll™ Matri sample pr eparation (g.) .

omponent	Sample I eight, g (. w t.)	Sample II e ight, g (w t.)	Sample III eight, g (. w t.)	Sample I eight, g (w t.)
S s uball™ Matri
Sylgard pa rt A	.7	.	.	.
Sylgard pa rt	.7	.	.	.

The double layer thin films were poured into 91x91mm commercial polycarbonate square containers, the approximate thickness of 1mm (see Figure 3a) was controlled by measuring the volume poured into the

containers, the bottom layer is 1.0 wt.% nanocomposite material and the top layer is PDMS as shown in Figure 3b, the pouring time between each layer had an intermediate time of 24 hrs., visual inspection was performed using an OCA 15EC equipment (DataPhysics Instruments GmbH, Filderstadt, Germany) in order to inspect the contours and layer thicknesses using backlight and the level surface of the equipment (see Figure 3c). The low filler concentrations and the homogeneity of the dispersion in the PDMS matrix is visibly appreciable against the light, showing that at such levels of concentrations the flexible membrane is still translucent as shown in Figure 3d.

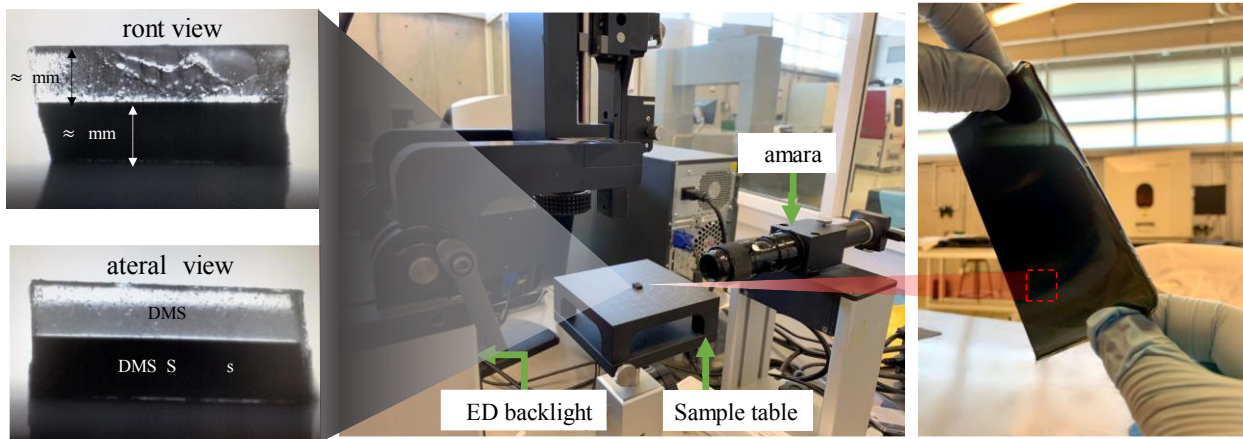


Figure 3. Front view (a) and lateral view (b) of nanocomposite thin bilayer film; (c) set-up for cross-sectional thickness inspection of film samples; (d) translucent flexible thin film with minimum filler loading of 0.5 wt.%.

2.2. Testing Validation Method for Stretchable Materials

Given the simplicity of uniaxial tension testing, engineering materials are often tested using this well-established method; however, many soft flexible materials exhibit different behavior when loaded under different states of deformation, especially when the response is considered nonlinear and hyperelastic. It is even feasible to state that flexible materials (continuous or architected) present at least 9 deformation mechanisms, see Figure 4. Although the typical deformation mechanisms illustrated in Figure 4a are mostly understood and some have been studied in-depth, our focus is on deformation mechanisms that are primarily determined by their boundary conditions and are only visibly demonstrable in flexible and stretchable materials as show in Figure 4b. These unique deformation descriptors are comparable to dripping, tip streaming or jetting regime during the dynamic droplet deformation and breakup behavior of fluids and colloids materials [207]. Squashing behavior as a descriptor of deformation in soft textured materials under indentation conditions has been reported previously [208]. However, the change in the shape of a generic bulk material may be due to other deformation mechanisms such as ripping, shearing, tearing, sticking, pushing, poking, sliding, pushing, clenching, grinding, or pulling, which are not addressed in this paper but are relevant to mention.

Therefore, it is of utmost importance to perform mechanical performance tests beyond the standard uniaxial tension or compression mechanical tests to fully capture the dynamic or static response of a soft material. According to the review of the literature on mechanical testing within this range of non-traditional methods, there are on the one hand multi-axial tests, such as well-known biaxial testing, and on the other hand there are out-plane tests based on indentation, such as small punch testing [209]. Typically, a small punch device is designed to characterize the behavior of a material under biaxial tension principle and is based on miniature specimen mechanical testing standard ASTM F2183 [210].

The test uses a small spherical punch, which is pressed into a miniature disk specimen held by the outer edge. The results of this type of testing are useful for characterizing the biaxial out-plane stress-strain response of a material and for validating the hyperelastic material model developed solely with stress-strain data from in-plane uniaxial tests. We have carried out two additional tests (see Figure 4b) besides to the typical monotonically uniaxial tests and loading and unloading tests to characterize the hysteresis Mullins effect to provide data to the deep learning model. Both tests use the small punch test design principle, as they make use of a spherical indenter, with diameter 10 mm, The small indenter, the custom-made fixture, and dogbone molds was 3D printed using a benchtop SLA-LF Form 3 additive manufacturing equipment (Formlabs, Somerville, OH, USA) (see Figure 4c).

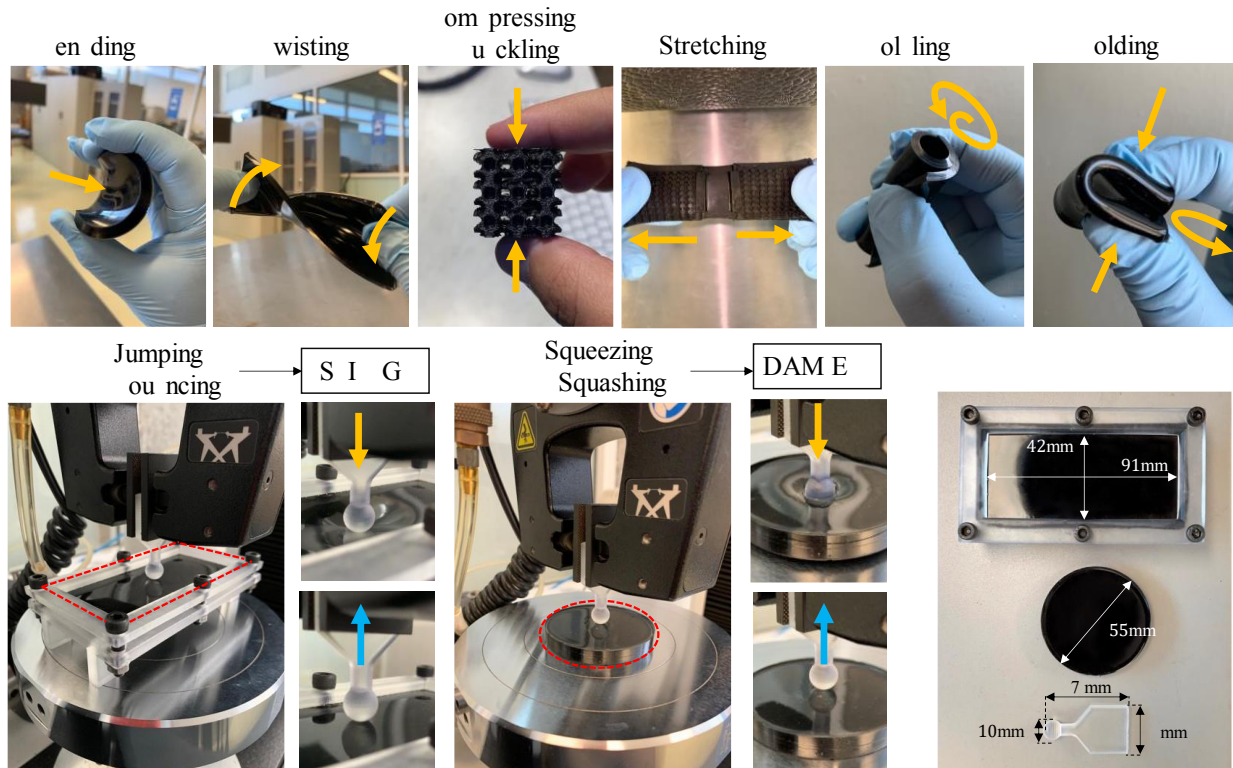


Figure 4. (a) Traditional in-plane deformation mechanisms for continuous or architected flexible materials; (b) deformation mechanisms inspired by out-of-plane indentation with unconventional boundary conditions that reveal elastic performance similar to spring or damper behavior descriptors; (c) custom-made fixture and indentation tip for out-of-plane deformation testing.

The uniaxial tensile tests were using Type 1A dogbone shape samples with an overall length of 100 mm and a 3 mm thickness according to ASTM D412-16 (2021)[181]. A universal machine (3365, INSTRON, Norwood, MA, USA) equipped with a 50 kN load cell was used. Three specimens of each type of continuous pure PDMS material and assessed composition (Sample I, Sample II, and Sample III) were loaded axially and monotonically at a speed deformation of 0.3 mm/s until complete failure. Next, loading-unloading uniaxial cyclic tests were performed with a maximum strain level $\epsilon = 0.6$ considering a 300 mm/min rate for 10 first continuous cycles to observe the stability of mechanical softening.

2.3. Fundamental System Identification and RNN Analogy

Since we can generally convert nonlinear models to a linear model (in a small region around the equilibrium point), we will assuming a linear time-invariant system. However, everything explained

below applies directly to nonlinear systems. We consider a continuous-time linear state-space model with n states, m inputs and r outputs are proposed as:

$$\begin{aligned}\dot{\mathbf{x}}(t) &= A\mathbf{x}(t) + B\mathbf{u}(t) \\ \mathbf{y}(t) &= C\mathbf{x}(t) + D\mathbf{u}(t)\end{aligned}\tag{Equation}$$

where at time $t \geq 0$, $\mathbf{x} \in \mathbb{R}^n$ is the state vector (internal system memory), $\mathbf{u} \in \mathbb{R}^m$ is the control input vector acting on the system, and $\mathbf{y} \in \mathbb{R}^r$ is an observable (measured) output vector. The matrices $A \in \mathbb{R}^{n \times n}$ (system matrix), $B \in \mathbb{R}^{n \times m}$ (input matrix), $C \in \mathbb{R}^{r \times n}$ (output matrix), and $D \in \mathbb{R}^{r \times m}$ (feedthrough matrix) are real state-space matrices and have compatible dimensions, where m, n, r integer positive numbers (n is also often called the order of the system). Similarly, the discrete-time version of the previous model has the following form:

$$\begin{aligned}\mathbf{x}_{k+1} &= A\mathbf{x}_k + B\mathbf{u}_k \\ \mathbf{y}_k &= C\mathbf{x}_k + D\mathbf{u}_k\end{aligned}\tag{Equation}$$

where k is a discrete-time instant. That is, the approximations of the original state are made at the time $t = kh$, where h is a sampling period or discretization step. On the other hand, the RNN architectures such as Simple Recurrent Neural Networks (SRNN) have the following mathematical expression:

$$\begin{aligned}\mathbf{q}_k &= \sigma_q(L\mathbf{q}_{k-1} + E\mathbf{p}_k + \mathbf{z}) \\ \mathbf{v}_k &= \sigma_u(P\mathbf{q}_k + \mathbf{g})\end{aligned}\tag{Equation}$$

where \mathbf{q}_k is a hidden layer vector, \mathbf{p}_k is a Neural Network (NN) input vector, \mathbf{v}_k is an NN output vector, \mathbf{z} and \mathbf{g} are vectors of NN parameters, L, E , and P are matrices consisting of NN parameters, and σ_q, σ_u are vectors activation function, and k is discrete time. If we use linear activation functions, then, the parameter vectors \mathbf{z} and \mathbf{g} are zero, the SRNN model described by Equation 3 resembles the state-space model described by Equation 2. Hence, our main objective is to train the parameters of RNN such that trained networks produce the input-output behavior of the discrete-time state-space model define in Equation 2.

2.4. Baseline Numerical Mechanical Model and One-Step Approximation

Instead of training the discrete signal directly using RNN, the neural network in this paper parameterizes the derivative of structural states with respect to time. For a mass-spring-damper system, the equilibrium equation using Newton's second law of motion in terms of the fractional time derivatives can be written as:

$$m\ddot{d} + k_d\dot{d} + k_s d = F\tag{Equation}$$

where m is the mass, d is a displacement from the equilibrium point, k_d and k_s are viscous damping and spring coefficients and F is the external control force. However, in the practice, we often do not know the precise values of the constants k_d and k_s , defining the mathematical model and will not be able to accurately predict the behavior of the system. Using the state-space variables $x^{(1)} = d$ and $x^{(2)} = \dot{d}$. Hence, $\dot{x}^{(1)} = \dot{d} = x^{(2)}$ and $\dot{x}^{(2)} = \ddot{d} = -\frac{k_d}{m}\dot{d} - \frac{k_s}{m}d + \frac{1}{m}F = -\frac{k_d}{m}x^{(2)} - \frac{k_s}{m}x^{(1)} + \frac{1}{m}F$. So, the model defined by Equation 4 can be rewritten the state equation as matrix:

$$\underbrace{\begin{bmatrix} \dot{x}^{(1)} \\ \dot{x}^{(2)} \end{bmatrix}}_{\dot{\mathbf{x}}} = \underbrace{\begin{bmatrix} 0 & 1 \\ -\frac{k_s}{m} & -\frac{k_d}{m} \end{bmatrix}}_A \underbrace{\begin{bmatrix} x^{(1)} \\ x^{(2)} \end{bmatrix}}_{\mathbf{x}} + \underbrace{\begin{bmatrix} 0 \\ 1 \\ \frac{1}{m} \end{bmatrix}}_{\tilde{B}} \underbrace{F}_{\mathbf{u}} \quad \text{Equation}$$

The position vector d (state variable $x^{(1)}$) is the only one that can be direct measured. Hence, the output equation takes the matrix form:

$$\underbrace{d}_{\mathbf{y}} = \underbrace{\begin{bmatrix} 0 & 1 \end{bmatrix}}_C \underbrace{\begin{bmatrix} x^{(1)} \\ x^{(2)} \end{bmatrix}}_{\mathbf{x}} \quad \text{Equation}$$

The state-space model define by Equation 5 and Equation 6 is in the continuous-time domain. From the machine learning perspective, this is not convenient, so it is necessary to obtain the representation in discrete time domain. The backward Euler method was used to transform it into the discrete-time domain. Using this one-step approximation, we obtain:

$$\dot{\mathbf{x}} = \frac{\mathbf{x}_k - \mathbf{x}_{k-1}}{h} = A\mathbf{x}_k + B\mathbf{u}_{k-1} \quad \text{Equation 7}$$

where h is the discretization time step. The last equation can be defined as:

$$\mathbf{x}_k = \tilde{A}\mathbf{x}_{k-1} + \tilde{B}\mathbf{u}_{k-1} \quad \text{Equation}$$

where $\tilde{A} = (I - hA)^{-1}$ and $\tilde{B} = h\tilde{A}B$, both discrete matrix representation, and the output equation remains unchanged form as:

$$\mathbf{y}_k = C\mathbf{x}_k \quad \text{Equation}$$

The discrete representations of the system defined in Equation 8 and Equation 9 are sufficiently convenient to define the estimation model. Note the similarities between the state model defined above and the Simple Recurrent Neural Network described in the previous section. First, the recursive relationship of the hidden layer vector (\mathbf{q}) and the state of the system (\mathbf{x}), and the presence of input vectors (\mathbf{p} and \mathbf{u}) and output vectors (\mathbf{v} , \mathbf{y}).

Table 2. Summary of state-space model and Simple Recurrent Neural Network definition.

Simple e current e ural e twork	State Space Model
$\mathbf{q}_k = \sigma_q(L\mathbf{q}_{k-1} + E\mathbf{p}_k + \mathbf{z})$ $\mathbf{v}_k = \sigma_u(P\mathbf{q}_k + \mathbf{g})$	$\mathbf{x}_k = \tilde{A}\mathbf{x}_{k-1} + \tilde{B}\mathbf{u}_{k-1}$ $\mathbf{y}_k = C\mathbf{x}_k$

2.5. Data Sets Experimental Data and Network Setup

In order to train, fit, and learn the neural network parameters ($L, E, \mathbf{z}, \mathbf{g}$) based on experimental data, the physical sequence force observable input vector $\mathbf{u}: \{u_0, u_1, \dots, u_N\}$ (and an initial state of the system) is required as input data, hence, it should produce the predictable sequence of output vector data $\hat{\mathbf{y}}: \{\hat{y}_0, \hat{y}_1, \dots, \hat{y}_N\}$ that accurately approximates the output sequence $\mathbf{y}: \{y_0, y_1, \dots, y_N\}$ of the real-system. In other words, the main objective is to use a physics-driven model takes an initial condition \mathbf{x}_0 at time t_0 and produces a accurate prediction $\hat{\mathbf{x}}$ of the actual state \mathbf{x} such that $\hat{\mathbf{x}}(t; \mathbf{x}_0) \approx \mathbf{x}(t; \mathbf{x}_0)$ as much as

possible. For the application of predicting state variables on a stress-strain curve that this manuscript aims to solve, the data set is defined as:

$$S = \{\mathbf{x}_k^{(i)}, \mathbf{x}_{k-1}^{(i)}; \mathbf{u}_k^{(i)}, h_k\}, i = 0, \dots, N \quad \text{Equation}$$

where N is the length of sampled data pairs and $\mathbf{x}_k^{(i)}$ denotes the i :th state variable \mathbf{x} in the k :th data pair and $\mathbf{x}_{k-1}^{(i)}$ is the pertaining state variable one discrete time-step h . The force $\mathbf{u}_k^{(i)}$ is the force that is acting on the system at the k :th time point. The goal is to make the \mathcal{L} loss function adequately small which is done through training the NN parameters. Here, Mean Squared Error (MSE) function \mathcal{L} is our loss function (also known as the cost function) defined as:

$$\mathcal{L}(\hat{y}, y) = \frac{1}{N} \sum_{i=1}^N (\hat{y}^{(i)} - y^{(i)})^2 \quad \text{Equation}$$

We implement a custom programming code using Python 3.10 for computing the discrete data sample from continuous-time system response via the backward Euler method with $N = 200$ simulation time steps and sampling period (discretization step) $h = 0.01$ s. The code was used to generate training, validation, and test data for three NN methods via Keras (deep learning API) from TensorFlow open-source platform. The network setup is a fully connected neural network with several unit cells conditions. Each unit cell architecture also has the variant sigmoid activation function $f(x) = \tanh x$.

3. Results and Discussion

3.1. Stress-strain Behavior, Mullins Effect and Strain Energy

The elastic energy (U_E), dissipated energy (U_D), and input total energy (U_T) of each loading-unloading cycle for the PDMS-SWCNTs samples were calculated as:

$$U = \int_{x_1}^{x_2} F dx \quad \text{Equation}$$

$$U_T = U_D + U_E \quad \text{Equation}$$

It can be seen from Figure 5 that the strain-stress and hysteresis curves of the three combinations of carbon nanotubes and PDMS showed a nonlinear trend. The elastic energy (U_E) that is stored in nanocomposite from elastic deformation is released during deformation recovery work. The dissipated energy (U_D) includes plastic strain energy which generates a permanent strain in the flexible material. The energy loss index refers to the ratio of the total energy accumulated to the strain energy dissipated in a uniaxial loading test. To verify the validity of the above viewpoint, the experimental data were further processed as $\frac{U_D}{U_T} \times 100$.

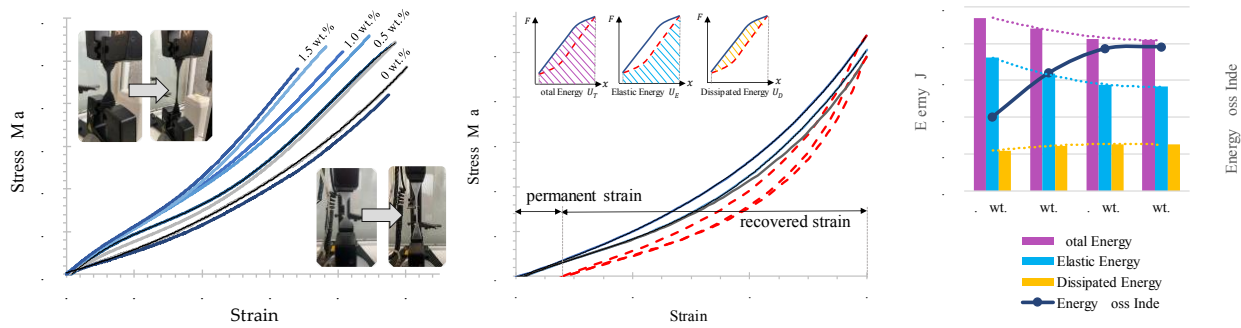


Figure 5. (a) Uniaxial static test until failure of the 4 types of specimens with different percentages of filler composition; (b) loading-unloading test showing the hysteresis behavior during nonlinear elastic deformation, as well as the permanent strain present in the nanocomposite material; (c) Trend histogram of the calculation of the 3 types of energy present during the cyclic-to-cycle tests performed.

The out-of-plane mechanical test data is relevant complementary data for the neural network training model as it allows obtaining conditions under unconventional mechanical performances. A mechanical test dominated by jumping and bouncing shows a highly deformable material with relatively low application forces and that easily recovers its original state with energy losses ranging 10% of all potential strain energy as seen in Figure 6a. In contrast, a squashing and squeezing dominated condition reflects high energy hysteresis behavior with an exponential trend as the strain in the material increases as illustrated in Figure 6b. The matching FEM simulation results accompanying the experimental data in Figure 6 were obtained to evidence the prelude to the final validation results presented in the next section, these simulations were modeled using the neural network framework with input data from the elastic tests and complementary cyclic tests without requiring the use of hyperelastic model equations or fitting parameters.

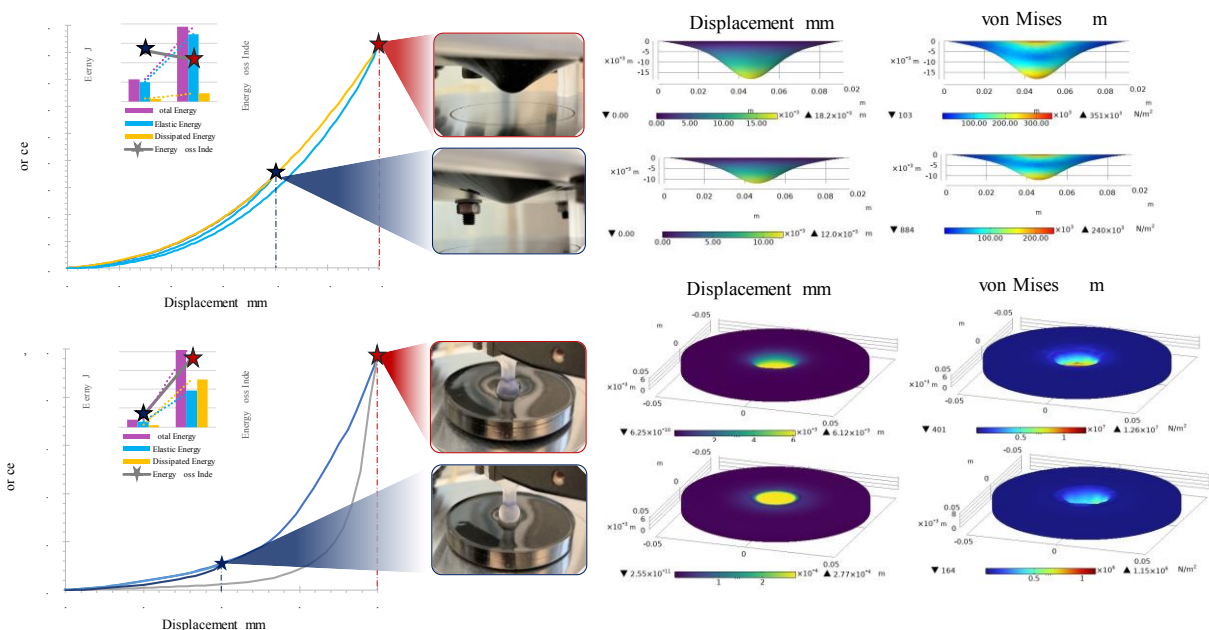


Figure 6. Non-conventional mechanical tests to demonstrate non-linear behavior and energy losses in flexible materials under various non-linear mechanical deformation conditions; (a) Test to show

bouncing and jumping mechanisms (spring-driven deformation), **(b)** Test to show squeezing and squashing mechanisms (damper-driven deformation).

3.2. Nanocomposite Ball Dynamics Tuning Experimental Data

To investigate the accuracy and efficiency of the proposed definitive data-driven method, the dynamic mechanical properties of a vertically dropped hollow ball is studied. The elastic shell of the ball is assumed to be four layers with thickness of 0.5mm each one, 1 layer of PDMS, and one layer for each loading concentration of nanocomposite at 0.5 wt.%, 1 wt.% and 1.5 wt.%. Nagurka and Huang [211] and many others subsequently [212], [213] analyzed the no linear dynamics of a bouncing ball by modeling it as a mass-spring-damper system analogy. The simple example of the bouncing ball clearly shows the presence of different deformation mechanisms acting on dynamically complex soft and stretchable objects illustrated in Figure 7. Other authors have also made use of the damping-spring-mass, bouncing ball, and deep learning to provide a successful reduced-order model to describe the dissipative behavior of nonlinear phenomena [214].

Next, the main parameters of the bouncing ball are estimated from the full experimental data using a deep learning process to obtain an equivalent virtual simulation configuration. Previously, this model has been tested using discretization techniques and traditional computational optimizations with good results [215]. The training process considers the energy loss and elastic energy from experimental data to obtain a closed-loop simulation. The governing equation of motion of the bouncing ball dynamics in the instant impact with the ground is described using Equation 4, where the F is the instant force gravity of the ball with initial conditions of $\mathbf{x}_0 = 0$ and $\dot{\mathbf{x}}_0 = -v_0$, where v_0 is the impact velocity just prior to the impact. The main problem is that de bounce mechanical behavior, involving no linear deformation, restitution, energy loss, and then rebound, requires an underdamped solution. The other states of the system, before the impact and the steady solution, which is applied after the bounces are extinguished, are trivial solutions.

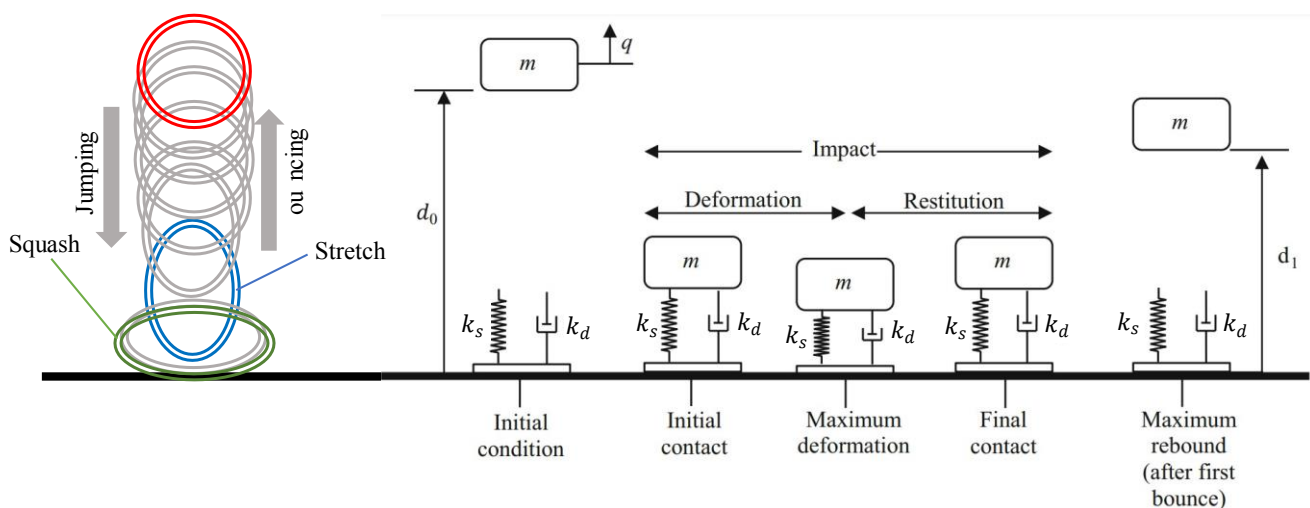


Figure 7. (a) Schematic representation of the deformation mechanism of bounding stretchable ball; (b) A mass-spring-damper model of a bouncing ball showing phases of the first cycle (figure adapted from [216]).

The contact spring is used for the bouncing at impact and the contact damper for the squashing energy dissipation. It is assumed that there is no air friction or any other energy loss that cannot be attributed to the spring-damper system. There are three regimes present during ball rebound, before impact, at the right moment of impact and after impact. The graphs in Figure 7a show the free fall and spring rebound. The vertical deformation and energy loss rates of the stretchable object were well explained by the spring-damper model. This model will be conceptually illustrated in Figure 7b using a nonlinear spring and a nonlinear viscous damper in parallel configuration (Kelvin-Voigt viscoelastic model). Figure 8 shows the predicted and real reference data for different numbers of units (8, 16, 32, and 64), and plots the training and validation losses with respect to 2000 epochs.

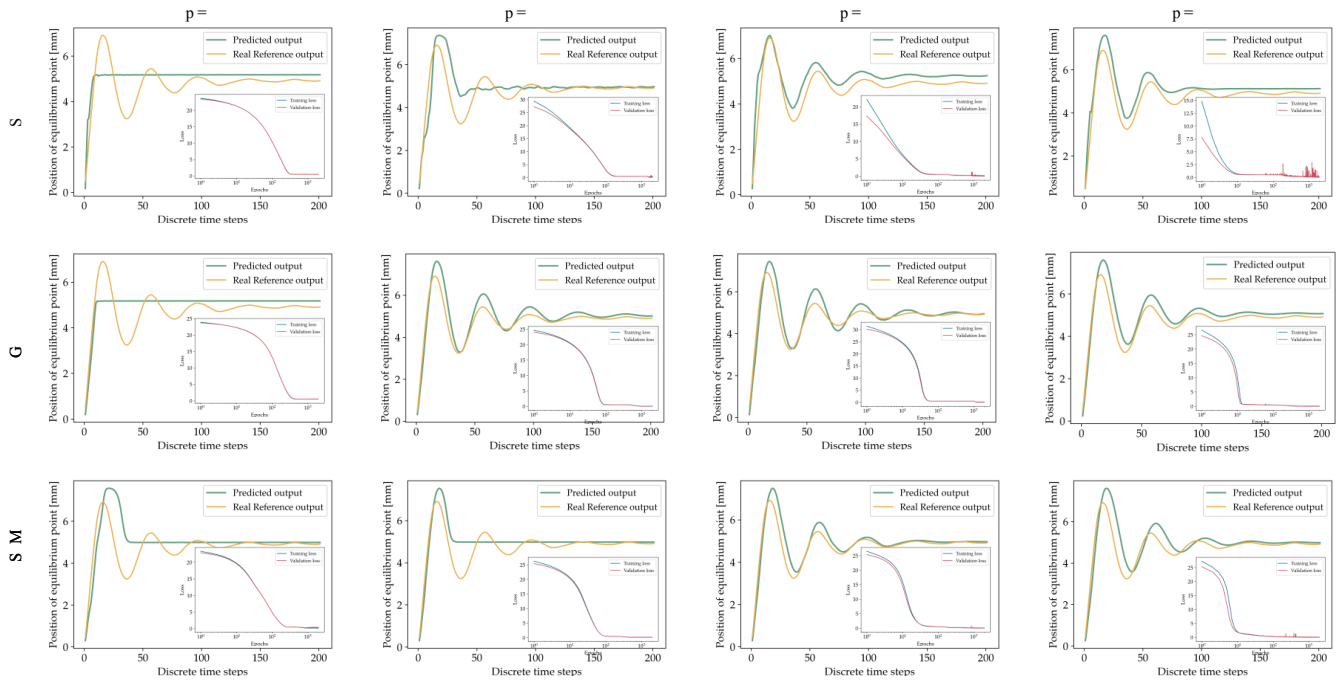


Figure 8. Predicted and real reference outputs of the SRNN, GRU, and LSTM architectures with their training, and validation losses for different number of units p .

All RNN architectures demonstrate that increasing the number of units improves prediction results. It should be noted here that the training is terminated after 2000 epochs, and the effect of overfitting is not seen. Many units imply a higher order model for estimating the system and increasing the number of epochs also allows for better outcomes. However, if we apply nonlinear activation function functions and omit the application of bias in the code, we get the results given in Figure 9a. When applying the afore mentioned adjustments, a simple SRNN design with two units and twice as many epochs can better predict the bouncing phenomena. The impact of the number of units on the processing time is negligible however processing the learning model at twice the number of epochs requires significantly more time, however the SRNN model requires significantly less processing time due to the simplicity of its architecture, see Figure 9b.

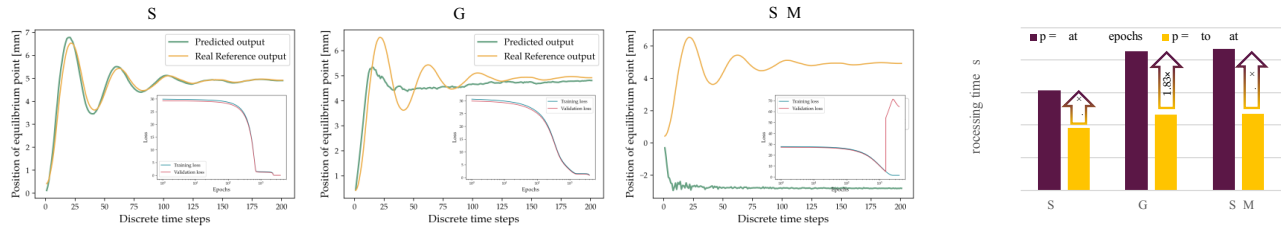


Figure 9. (a) Prediction performance, training, and validation losses for modified SRNN, GRU, LSTM architectures using 2 units and 4000 epochs; (b) Comparison of processing time.

4. Conclusions and Future Work

We present several neural network (NN) structures to approximate the nonlinear mechanical behavior of soft nanocomposite materials based on an analogy with the behavior of dynamic systems, using experimental elastic deformation data from static tensile testing and loading and unloading. The NN structures are based on Recurrent Neural Networks (RNN), Gated Recurrent Unit (GRU), and Long Short-Term Memory (LSTM). Derivations of the simplest case were presented to show the analogy of state-space models and mechanical dynamical systems. Once successfully trained, the methods produce discrete dynamical systems that approximate the unknown underlying governing equations of the nonlinear deformation of nanocomposite material. We present the details of the construction of the methods, their theoretical justifications, and use experimental examples and their implementation in computational simulation to demonstrate the effectiveness of the methods. We present the details of the construction of the methods, their theoretical justifications, and use experimental examples and their implementation in computational simulation to demonstrate the effectiveness of the methods. The fundamental difficulty with the approach given in this publication is that it requires knowledge of a beginning condition to be applied. In real-world applications, the beginning state of a dynamic system is rarely known. However, if the system is stable, the initial state can be ignored because the effect of the initial condition fades with time. Another option is to recast the model to be estimated as an autoregressive-exogenous (ARX) model. This model predicts the system's output only based on previous inputs and outputs.

The solution of a general mechanical dynamical system can then be approximated using only the trained neural network and a state-space variables. When training the neural network operator to approximate the effective output data, the analytical and experimental solutions of test mechanical configurations are used to produce the training data on which the network can be trained. We describe the concept of neural networks and the surrounding concepts that a neural network can approximate this effective increment, eliminating the necessity for a known governing equation when defining the system to mechanically represent the behavior of a soft material with nonlinear deformation. A broad mechanical dynamical system's solution can thus be approximated using only a trained neural network and state-space variables in complex deformation phenomena such as the bouncing ball. Efficiency in other deformation mechanism can and should be explored to improve our compression of soft materials and their energy losses.

Author Contributions:

Josué García-Ávila: Conceptualization, Data curation, Investigation, Visualization, Writing— original draft. **Diego de Jesus Torres-Serrato:** Data curation, Investigation, **J. Israel Martínez-López:** Data curation, Resources, Supervision, Visualization, Review & Editing. **Erick Ramírez-Cedillo:** Formal Analysis, Methodology, Project Administration, Resources, Supervision, Visualization **Ciro A.**

Rodríguez: Conceptualization, Data curation, Validation, Review & Editing. **Adriana Vargas-Martínez:** Funding Acquisition, Review & Editing. All authors have read and agreed to the published version of the manuscript.

Acknowledgments:

The Research Group of Advanced Manufacturing from Tecnológico de Monterrey provided support for the acquisition of materials and goods. Josué García Ávila acknowledges the grant support of the Mexican National Council for Science and Technology (CONACYT). The authors acknowledge the support from Centro de Investigación Numérica and 3D Factory.

Declaration of conflicting interests:

The Authors declares that there is no conflict of interest.

Funding:

This research was funded by Tecnológico de Monterrey and Mexican National Council for Science and Technology (CONACYT) and J.G.-Á. MSc studies (scholarship number 1002683).

Publication:

The entire content of this section is being reviewed and prepared for future publication.

REFERENCES

- [1] “Multiscale Methods – Division Mechanics of Functional Materials – Darmstadt.” https://www.mawi.tu-darmstadt.de/mfm/mfm_research/mfm_research_areas/mfm_multiscale_methods/index.en.jsp (accessed Jun. 11, 2022).
- [2] “Smart Inventions Inspired by Nature Biomimicry - Bloomberg.” <https://www.bloomberg.com/news/photo-essays/2015-02-23/14-smart-inventions-inspired-by-nature-biomimicry> (accessed May 21, 2022).
- [3] Hippocrates, *On Wounds in the Head. In the Surgery. On Fractures. On Joints. Mochlicon*. Cambridge: Harvard University Press, 1928. [Online]. Available: <https://www.hup.harvard.edu/catalog.php?isbn=9780674991651>
- [4] R. LeMoine, *Advances for Prosthetic Technology*. Tokyo: Springer Japan, 2016. doi: 10.1007/978-4-431-55816-3.
- [5] J. R. Kirkup, *A History of Limb Amputation*. London: Springer London, 2007. doi: 10.1007/978-1-84628-509-7.
- [6] M. R. Pitkin, *Biomechanics of Lower Limb Prosthetics*. Berlin, Heidelberg: Springer Berlin Heidelberg, 2010. doi: 10.1007/978-3-642-03016-1.
- [7] P. W. Moxey et al., *Lower extremity amputations - a review of global variability in incidence*, vol. 28, no. 10. 2011. doi: 10.1111/j.1464-5491.2011.03279.x.
- [8] OECD, *Health at a Glance 2019*. OECD, 2019. doi: 10.1787/4dd50c09-en.
- [9] E. Vázquez, *Los amputados y su rehabilitación. Un reto para el Estado*. 2016.
- [10] A. F. T. Mak, M. Zhang, and E. W. C. Tam, *Biomechanics of Pressure Ulcer in Body Tissues Interacting with External Forces during Locomotion*, vol. 12, no. 1. 2010. doi: 10.1146/annurev-bioeng-070909-105223.
- [11] W. Braune and O. Fischer, *The Human Gait*. Berlin, Heidelberg: Springer Berlin Heidelberg, 1987. doi: 10.1007/978-3-642-70326-3.
- [12] A. L. Baert and K. Sartor, *Imaging of the Foot and Ankle*. Berlin, Heidelberg: Springer Berlin Heidelberg, 2003. doi: 10.1007/978-3-642-59363-5.
- [13] J. M. R. S. Tavares and J. P. Fernandes, “Correction to New Developments on Computational Methods and Imaging in Biomechanics and Biomedical Engineering,” in *Lecture Notes in Computational Vision and Biomechanics*, vol. 999, 2019, pp. C1–C1. doi: 10.1007/978-3-030-23073-9_11.
- [14] G. A. Ateshian, K. M. Myers, and J. M. R. S. Tavares, *Computer Methods, Imaging and Visualization in Biomechanics and Biomedical Engineering*, vol. 36. Cham: Springer International Publishing, 2020. doi: 10.1007/978-3-030-43195-2.
- [15] K. M. Moerman, D. Solav, D. Sengeh, and M. Ferrer, “Automated and Data-driven Computational Design of Patient-Specific Biomechanical Interfaces,” doi: 10.1007/978-3-030-23073-9_11.
- [16] D. Solav, K. M. Moerman, A. M. Jaeger, and M. Ferrer, “A Framework for Measuring the Time-Varying Shape and Full-Field Deformation of Residual Limbs Using 3-D Digital Image Correlation,” *IEEE Transactions on Biomedical Engineering*, vol. 66, no. 10, pp. 2740–2752, Oct. 2019, doi: 10.1109/TBME.2019.2895283.
- [17] C. Murray, *Amputation, Prosthesis Use, and Phantom Limb Pain*. New York, NY: Springer New York, 2010. doi: 10.1007/978-0-387-87462-3.
- [18] L. Nolan, A. Wit, K. Dudziński, A. Lees, M. Lake, and M. Wychowański, *Adjustments in gait symmetry with walking speed in trans-femoral and trans-tibial amputees*, vol. 17, no. 2. 2003. doi: 10.1016/S0966-6362(02)00066-8.

- [19] A. Hazari and G. A. Maiya, *Clinical Biomechanics and its Implications on Diabetic Foot*. Singapore: Springer Singapore, 2020. doi: 10.1007/978-981-15-3681-6.
- [20] J. C. Cagle *et al.*, “Finite element model to assess transtibial prosthetic sockets with elastomeric liners,” *Medical and Biological Engineering and Computing*, vol. 56, no. 7, pp. 1227–1240, Jul. 2018, doi: 10.1007/S11517-017-1758-Z/FIGURES/11.
- [21] J. J. Darter, K. Sinitski, and J. M. Milken, “Maximal bone-socket displacement for persons with a traumatic transtibial amputation: The effect of elevated vacuum suspension at progressive body-weight loads,” *Prosthetics and Orthotics International*, vol. 40, no. 5, 2016, doi: 10.1177/0309364615605372.
- [22] M. E. Enot, J. Stines, M. Walter, M. Martinet, J. Pysant, and A. Lum, “Imaging of the pain ul lower limb stump,” *Radiographics*, vol. 20, no. SPEC.ISS., 2000, doi: 10.1148/radiographics.20.suppl_1.g00oc14s219.
- [23] K. M. Werner, A. A. Linberg, and E. J. Cole, “Reliability of digital fluoroscopic video for assessing axial and mediolateral movement of the femur during weight bearing in individuals with trans femoral amputations,” *Journal of Prosthetics and Orthotics*, vol. 25, no. 2, 2013, doi: 10.1097/JPO.0b013e31828adc1f.
- [24] G. Colombo, M. Comotti, D. Dezaelli, D. Degazzoni, M. Izzi, and A. Itali, “A method to improve prosthesis leg design based on pressure analysis at the socket-residual limb interface,” *Proceedings of the ASME Design Engineering Technical Conference*, vol. 1A-2016, 2016, doi: 10.1115/DETC2016-60131.
- [25] M. Gholizadeh, M. Azuan, A. Osman, A. Eshraghi, M. Anuar, and A. Aszak, “Clinical implication of interface pressure for a new prosthetic suspension system,” doi: 10.1186/1475-925X-13-89.
- [26] O. Al-Ketan, R. Rowshan, and R. K. Abu Al-ub, “Topology-mechanical property relationship of 3D printed strut, skeletal, and sheet based periodic metallic cellular materials,” *Additive Manufacturing*, vol. 19, pp. 167–183, Jan. 2018, doi: 10.1016/j.addma.2017.12.006.
- [27] A. S. Dalaq, D. W. Abueidda, R. K. Abu Al-ub, and I. M. Jasiuk, “Finite element prediction of effective elastic properties of interpenetrating phase composites with architected 3D sheet reinforcements,” *International Journal of Solids and Structures*, vol. 83, pp. 169–182, Apr. 2016, doi: 10.1016/j.ijsolstr.2016.01.011.
- [28] J. J. Limothy and G. Meschke, “A cascade continuum micromechanics model for the effective elastic properties of porous materials,” *International Journal of Solids and Structures*, vol. 83, pp. 1–12, Apr. 2016, doi: 10.1016/J.IJSOLSTR.2015.12.010.
- [29] M. Abst, E. Gregorová, and G. Michá, “Effective properties of suspensions, composites and porous materials,” *J Eur Ceram Soc*, vol. 27, no. 2–3, pp. 479–482, 2007, doi: 10.1016/J.JEURCERAMSOC.2006.04.169.
- [30] M. Abst and E. Gregorová, “Young’s modulus of isotropic porous materials with spheroidal pores,” *J Eur Ceram Soc*, vol. 34, no. 13, pp. 3195–3207, 2014, doi: 10.1016/J.JEURCERAMSOC.2014.04.009.
- [31] M. Ha ng, G. ang, S. e e lang, A. A. adpoor, and J. hou, “Topological design, permeability and mechanical behavior of additively manufactured functionally graded porous metallic biomaterials,” *Acta Biomaterialia*, vol. 84, pp. 437–452, Jan. 2019, doi: 10.1016/j.actbio.2018.12.013.
- [32] G. Kumar and A. Barber, “An integral representation of fields with applications to finite element analysis of spatially varying materials,” *CAD Computer Aided Design*, vol. 126, Sep. 2020, doi: 10.1016/j.cad.2020.102869.
- [33] M. He ng, S. Kumar, and D. M. Kochmann, “Data-driven topology optimization of spinodoid metamaterials with seamlessly tunable anisotropy,” *Computer Methods in Applied Mechanics and Engineering*, vol. 383, p. 113894, Dec. 2020, doi: 10.1016/j.cma.2021.113894.

- [34] A. A. Adipoor, “Additively manufactured porous metallic biomaterials,” *Journal of Materials Chemistry B*, vol. 7, no. 26. Royal Society of Chemistry, pp. 4088–4117, 2019. doi: 10.1039/c9tb00420c.
- [35] A. A. Adipoor, “Mechanical performance of additively manufactured meta-biomaterials,” *Acta Biomaterialia*, vol. 85. 2019. doi: 10.1016/j.actbio.2018.12.038.
- [36] F. S. L. Bobbert *et al.*, “Additively manufactured metallic porous biomaterials based on minimal surfaces: A unique combination of topological, mechanical, and mass transport properties,” *Acta Biomaterialia*, vol. 53, 2017, doi: 10.1016/j.actbio.2017.02.024.
- [37] J. Rouquerol *et al.*, “Recommendations for the characterization of porous solids (technical report),” *Pure and Applied Chemistry*, vol. 66, no. 8, pp. 1739–1758, Jan. 1994, doi: 10.1351/PAC199466081739/MACHINEREREADABLECITATION/RIS.
- [38] M. Ohlgemuth, J. Uhlir, J. O. Man, and E. J. Thoma, “Triply periodic bicontinuous cubic Microdomain Morphologies by Symmetries,” *Macromolecules*, vol. 34, no. 17, pp. 6083–6089, Aug. 2001, doi: 10.1021/MA0019499.
- [39] J. J. K. Kirkensgaard, “Covalent network morphologies and compositionally robust -colored perforated lamellar phase in A(BC)₂ mikto-arm star copolymer melts,” *Soft Matter*, vol. 6, no. 24, pp. 6102–6108, Dec. 2010, doi: 10.1039/C0SM00358A/.
- [40] G. S. Doerk and K. G. Sager, “Beyond native block copolymer morphologies,” *Molecular Systems Design & Engineering*, vol. 2, no. 5, pp. 518–538, Dec. 2017, doi: 10.1039/C7ME00069C.
- [41] C. Crook *et al.*, “Late-nanolattices at the theoretical limit of stiffness and strength,” *Nature Communications*, vol. 11, no. 1, Dec. 2020, doi: 10.1038/s41467-020-15434-2.
- [42] J. Guan, S. Ding, and J. Shen, “Additive manufacturing technology for porous metal implant applications and triple minimal surface structures: A review,” *Bioactive Materials*, vol. 4, no. 1. KeAi Communications Co., pp. 56–70, Mar. 01, 2019. doi: 10.1016/j.bioactmat.2018.12.003.
- [43] S. Kumar, S. Han, J. Heung, and D. M. Kochmann, “Inverse-designed spinodoid metamaterials,” *npj Computational Materials*, vol. 6, no. 1, pp. 1–10, Dec. 2020, doi: 10.1038/s41524-020-0341-6.
- [44] J. Hou, J. Jin, and J. Du, “Functionally graded scaffolds with programmable pore size distribution based on triply periodic minimal surface fabricated by selective laser melting,” *Materials*, vol. 13, no. 21, pp. 1–17, Nov. 2020, doi: 10.3390/ma13215046.
- [45] O. Al-Ketan, D. W. Lee, R. Rowshan, and R. K. Abu Al-Abboud, “Functionally graded and multi-morphology sheet MS lattices: Design, manufacturing, and mechanical properties,” *Journal of the Mechanical Behavior of Biomedical Materials*, vol. 102, p. 103520, Feb. 2020, doi: 10.1016/j.jmbbm.2019.103520.
- [46] A. U. Smolin, G. M. Eremina, and S. U. K. Orstelev, “Methods for describing structure of novel porous materials: A review,” in *IOP Conference Series: Materials Science and Engineering*, Nov. 2019, vol. 696, no. 1, p. 012017. doi: 10.1088/1757-899X/696/1/012017.
- [47] R. T. Armstrong *et al.*, “Porous Media Characterization using Minkowski functionals: Theories, Applications and Future Directions,” *Transport in Porous Media*, vol. 130, no. 1, pp. 305–335, Oct. 2019, doi: 10.1007/s11242-018-1201-4.
- [48] K. J. Mecke, “Additivity, convexity, and beyond Applications of Minkowski functionals in Statistical Physics,” in *Statistical Physics and Spatial Statistics*, Springer Berlin Heidelberg, 2007, pp. 111–184. doi: 10.1007/3-540-45043-2_6.
- [49] W. Mickel, G. E. Schröder-Urlik, and K. Mecke, “Ensemble Minkowski functionals of triply periodic minimal surfaces,” *Interface Focus*, vol. 2, no. 5, pp. 623–633, Oct. 2012, doi: 10.1098/rsfs.2012.0007.
- [50] H. G. Yon Schnering and R. Nesper, “Global surfaces of Fourier series fundamental invariants of structured matter,”

- [51] . Soyarslan, . lüm er, and S. argmann, “una ble au e ticity and elastomechanical symmetry in a class of very low density core-shell cubic crystals,” *Acta Materialia*, vol. 177, pp. 280–292, Sep. 2019, doi: 10.1016/j.actamat.2019.07.015.
- [52] A. Dutta, K. Mukher ee, S. Dhara, and S. Gupta, “Design o porous titanium sca old or complete mandibular reconstruction: The influence of pore architecture parameters,” *Computers in Biology and Medicine*, vol. 108, pp. 31–41, May 2019, doi: 10.1016/j.combiomed.2019.03.004.
- [53] . e to e nriques, M. M. orreia, . G. unes, and . A . erreira, “E p loring the D geometry of the diffusion kurtosis tensor-Impact on the development of robust tractography procedures and novel biomarkers,” *Neuroimage*, vol. 111, pp. 85–99, May 2015, doi: 10.1016/j.neuroimage.2015.02.004.
- [54] . ol abella, A. . isilino, G. äiat, and . Kowalczyk, “Mimetization o the elastic properties of cancellous bone via a parameterized cellular material,” *Biomechanics and Modeling in Mechanobiology*, vol. 16, no. 5, pp. 1485–1502, Oct. 2017, doi: 10.1007/s10237-017-0901-y.
- [55] J. Kang, E. Dong, D. i, S. Dong, . ha ng, and . ang, “Anisotropy characteristics of microstructures for bone substitutes and porous implants with application of additive manu acturing in orthopaedic,” *Materials and Design*, vol. 191, Jun. 2020, doi: 10.1016/j.matdes.2020.108608.
- [56] X. Yu, J. Zhou, H. Liang, Z. Jiang, and L. Wu, “Mechanical metamaterials associated with sti ness, rigidity and compressibility A brie review,” *Progress in Materials Science*, vol. 94, pp. 114–173, May 2018, doi: 10.1016/J.PMATSCI.2017.12.003.
- [57] D. Healy, N. Timms, M. A. Pearce, D. Healy, N. imm s, and M. A. earce, “Aniso is a MATLAB™ toolbo or the visualisation o elastic anisotropy,” *AGUFM*, vol. 2016, pp. ED43C-0874, 2016, Accessed: Jun. 23, 2021. [Online]. Available: <https://ui.adsabs.harvard.edu/abs/2016AGUFMED43C0874H/abstract>
- [58] J. Vince, *Calculus for Computer Graphics*. Springer London, 2013. doi: 10.1007/978-1-4471-5466-2.
- [59] D. ealy, . E rik imm s, and M. Alan earce, “ he variation and visualisation o elastic anisotropy in rock- orming minerals,” *Solid Earth*, vol. 11, no. 2, pp. 259–286, 2020, doi: 10.5194/se-11-259-2020.
- [60] . J. esl and . . Jain, “Invariant sur ace characteristics for 3D object recognition in range images,” *Computer Vision, Graphics, and Image Processing*, vol. 33, no. 1, pp. 33–80, Jan. 1986, doi: 10.1016/0734-189X(86)90220-3.
- [61] J. J. Koenderink and A. J. van Doorn, “Sur ace shape and curvature scales,” *Image and Vision Computing*, vol. 10, no. 8, pp. 557–564, Oct. 1992, doi: 10.1016/0262-8856(92)90076-F.
- [62] . en, . ia o, and . a o, “Multi-property cellular material design approach based on the mechanical behaviour analysis of the reinforced lattice structure,” *Materials and Design*, vol. 174, Jul. 2019, doi: 10.1016/J.MATDES.2019.107785.
- [63] . u, J. ua ng, . ou, . Shao, and J. iu, “St ress-constrained shell-lattice infill structural optimisation or additive manu acturing,” <https://doi.org/10.1080/17452759.2019.1647488>, vol. 15, no. 1, pp. 35–48, Jan. 2019, doi: 10.1080/17452759.2019.1647488.
- [64] J. . izzuto, “E pe rimental investigation o reciprocally supported element (S E) lattice honeycomb domes structural behaviour,” *Engineering Structures*, vol. 166, pp. 496–510, Jul. 2018, doi: 10.1016/J.ENGSTRUCT.2018.03.094.
- [65] J. auer, . . Meza, . A. Schaedler, . Schwaiger, . he ng, and . aldevit, “ anolattices An Emerging lass o Mechanical Metamaterials,” *Advanced Materials*, vol. 29, no. 40, Oct. 2017, doi: 10.1002/ADMA.201701850.

- [66] A. Ibach and J. Polyst, “Triperiodic surfaces and cubic phases in mixtures of oil, water, and surfactant,” *Journal of Chemical Physics*, vol. 110, no. 2–12, pp. 3207–3214, Feb. 1999, doi: 10.1063/1.477842.
- [67] P. J. F. Gandy, S. Ardhan, A. Mackay, and J. Klinowski, “Triperiodic surface approximations to the P, G, D and I-tri-periodic minimal surfaces,” *Chemical Physics Letters*, vol. 336, no. 3–4, pp. 187–195, Mar. 2001, doi: 10.1016/S0009-2614(00)01418-4.
- [68] G. von Schnering and G. Jesper, “How Nature Adapts Chemical Structures to Curved Surfaces,” *Angewandte Chemie International Edition in English*, vol. 26, no. 11, pp. 1059–1080, 1987. doi: 10.1002/anie.198710593.
- [69] G. Jesper and G. Grin, “Triperiodic space partitioners (S) and their relations to crystal chemistry,” *Zeitschrift für Kristallographie*, vol. 226, no. 8, pp. 692–710, Aug. 2011, doi: 10.1524/zkri.2011.1429.
- [70] K. Hoi and S. Ju, “Constant-radius blending in surface modelling,” *Computer-Aided Design*, vol. 21, no. 4, pp. 213–220, 1989, doi: 10.1016/0010-4485(89)90046-8.
- [71] A. Erhard, A. Rthe, M. Ani, and J. yvill, “Implicit blending revisited,” *Computer Graphics Forum*, vol. 29, no. 2, pp. 367–375, May 2010, doi: 10.1111/j.1467-8659.2009.01606.x.
- [72] J. J. eale, J. ing, and J. J. ilson, “A Simple Method for Computing Singular or Early Singular Integrals on Closed Surfaces,” *Communications in Computational Physics*, vol. 20, no. 3, pp. 733–753, Sep. 2016, doi: 10.4208/cicp.030815.240216a.
- [73] M. r aizat, “Adding handles to riemann’s minimal surfaces,” *Journal of the Institute of Mathematics of Jussieu*, vol. 1, no. 1, pp. 145–174, 2002, doi: 10.1017/S147474800200004X.
- [74] P. J. F. Gandy, D. vi ović, A. Ma ckey, and J. Klinowski, “Exact computation of the triply periodic D (diamond) minimal surface,” *Chemical Physics Letters*, vol. 314, no. 5–6, pp. 543–551, Dec. 1999, doi: 10.1016/S0009-2614(99)01000-3.
- [75] R. K. Abu Al-Rub, D.-W. Lee, K. A. Khan, and A. ala zotto, “Effective Anisotropic Elastic and Plastic Yield Properties of Periodic Foams Derived from Triply Periodic Schoen’s I-WP Minimal Surface,” *Journal of Engineering Mechanics*, vol. 146, no. 5, p. 04020030, May 2020, doi: 10.1061/(asce)em.1943-7889.0001759.
- [76] H eng, H u, K. Du, H ang, and H i, “Minimal surface designs for porous materials from microstructures to mechanical properties,” *Journal of Materials Science*, vol. 53, no. 14, pp. 10194–10208, Jul. 2018, doi: 10.1007/s10853-018-2285-5.
- [77] D. W. Abueidda, R. K. Abu Al-Rub, A. S. Dalaq, D. W. Lee, K. A. Khan, and I. Jasiuk, “Effective conductivities and elastic moduli of novel foams with triply periodic minimal surfaces,” *Mechanics of Materials*, vol. 95, pp. 102–115, Apr. 2016, doi: 10.1016/j.mechmat.2016.01.004.
- [78] E. Cuan-r quizo, J. Shalchy, and A. ha skar, “Compressive stiffness of staggered woodpile lattices: Mechanics, measurement, and scaling laws,” *International Journal of Mechanical Sciences*, vol. 187, Dec. 2020, doi: 10.1016/j.ijmecsci.2020.105932.
- [79] D. W. Lee, K. A. Khan, and R. K. Abu Al- ub, “Stiffness and yield strength of architected foams based on the Schwarz primitive triply periodic minimal surface,” *International Journal of Plasticity*, vol. 95, pp. 1–20, Aug. 2017, doi: 10.1016/j.ijplas.2017.03.005.
- [80] K. A. Khan and R. K. Abu Al- ub, “Time dependent response of architected foams,” *International Journal of Mechanical Sciences*, vol. 126, pp. 106–119, Jun. 2017, doi: 10.1016/j.ijmecsci.2017.03.017.
- [81] M. Ashby, “The properties of foams and lattices,” *Philosophical Transactions of the Royal Society A: Mathematical, Physical and Engineering Sciences*, vol. 364, no. 1838, pp. 15–30, Jan. 2006, doi: 10.1098/rsta.2005.1678.

- [82] . S. De shpande, M. . Ashby, and . A. . leck, “ foam topology ending versus stretching dominated architectures,” *Acta Materialia*, vol. 49, no. 6, pp. 1035–1040, Apr. 2001, doi: 10.1016/S1359-6454(00)00379-7.
- [83] S. M. Sajadi *et al.*, “Multiscale Geometric Design rinciples Applied to D rinted Schwarzites,” *Advanced Materials*, vol. 30, no. 1, p. 1704820, Jan. 2018, doi: 10.1002/adma.201704820.
- [84] D. Downing, A. Jones, M. randt, and M. e ary, “Increased e iciency gyroid structures by tailored material distribution,” *Materials and Design*, vol. 197, Jan. 2021, doi: 10.1016/j.matdes.2020.109096.
- [85] O. Al-Ketan, R. Rezgui, R. Rowshan, H. Du, N. X. Fang, and R. K. Abu Al-Rub, “Microarchitected Stretching-Dominated Mechanical Metamaterials with Minimal Surface opologi es,” *Advanced Engineering Materials*, vol. 20, no. 9, Sep. 2018, doi: 10.1002/adem.201800029.
- [86] C. M. Portela *et al.*, “E tre me mechanical resilience o sel -assembled nanolabyrinthine materials,” *Proc Natl Acad Sci U S A*, vol. 117, no. 11, pp. 5686–5693, Mar. 2020, doi: 10.1073/pnas.1916817117.
- [87] . oltue, . Karuna, S. Khruaduangkham, S. Seehanam, and . romoppatum, “Design exploration of 3D-printed triply periodic minimal surface scaffolds for bone implants,” *International Journal of Mechanical Sciences*, vol. 211, Dec. 2021, doi: 10.1016/J.IJMECSCI.2021.106762.
- [88] S. J. P. Callens, R. J. C. Uyttendaele, L. E. Fratila-Apachitei, and A. A. a dpoor, “Substrate curvature as a cue to guide spatiotemporal cell and tissue organization,” *Biomaterials*, vol. 232, p. 119739, Feb. 2020, doi: 10.1016/J.BIOMATERIALS.2019.119739.
- [89] L. Yang *et al.*, “Investigation on the orientation dependence o elastic response in Gyroid cellular structures,” *Journal of the Mechanical Behavior of Biomedical Materials*, vol. 90, pp. 73–85, Feb. 2019, doi: 10.1016/j.jmbbm.2018.09.042.
- [90] . hen, . M. ie , . u, . ang, Q. i, a nd S. hou, “ n hybr id cellular materials based on triply periodic minimal surfaces with extreme mechanical properties,” *Materials and Design*, vol. 183, Dec. 2019, doi: 10.1016/j.matdes.2019.108109.
- [91] S. . owin and M. M. Mehrabadi, “ n the identi cation o material symmetry or anisotropic elastic materials,” *Quarterly Journal of Mechanics and Applied Mathematics*, vol. 40, no. 4, pp. 451–476, Nov. 1987, doi: 10.1093/qjmam/40.4.451.
- [92] A. ata pano, . Desmorat, and . a nnucci, “Sti ness and Strength pti mization o the Anisotropy Distribution or aminated Structures,” *Journal of Optimization Theory and Applications*, vol. 167, no. 1, pp. 118–146, Oct. 2015, doi: 10.1007/s10957-014-0693-5.
- [93] M. Benedetti, A. du Plessis, R. O. Ritchie, M. Dallago, S. M. J. Razavi, and F. Berto, “Architected cellular materials A review on their mechanical properties towards atigue-tolerant design and abrication,” *Materials Science and Engineering R: Reports*, vol. 144. Elsevier Ltd, Apr. 01, 2021. doi: 10.1016/j.mser.2021.100606.
- [94] J. Kadkhodapour *et al.*, “ ailure mechanisms o additively manu actured porous biomaterials E ects o porosity and type o unit cell,” *Journal of the Mechanical Behavior of Biomedical Materials*, vol. 50, pp. 180–191, Oct. 2015, doi: 10.1016/j.jmbbm.2015.06.012.
- [95] K. . G. Mc ullough, . A. leck, and M. . Ashby, “Stress-life fatigue behaviour of aluminum alloy oams,” *Fatigue and Fracture of Engineering Materials and Structures*, vol. 23, no. 3, pp. 199–208, Mar. 2000, doi: 10.1046/j.1460-2695.2000.00261.x.
- [96] A. A. a dpoor, “Mechanics o additively manu actured biomaterials,” *Journal of the Mechanical Behavior of Biomedical Materials*, vol. 70. Elsevier Ltd, pp. 1–6, Jun. 01, 2017. doi: 10.1016/j.jmbbm.2017.03.018.

- [97] A. G. Seyhaupt, “Deformations of the gyroid and ionic minimal surfaces,” *Pacific Journal of Mathematics*, vol. 235, no. 1, pp. 137–171, Mar. 2008, doi: 10.2140/pjm.2008.235.137.
- [98] E. F. Lehder, I. A. Ashcroft, D. Willman, I. Maskery, and S. Antu, “A multi-scale computational model to predict the performance of cell seeded scaffolds with triply periodic minimal surface geometries,” in *Solid Freeform Fabrication 2019: Proceedings of the 30th Annual International Solid Freeform Fabrication Symposium - An Additive Manufacturing Conference, SFF 2019*, 2019, pp. 1954–1964.
- [99] J. Miralbes, D. Manz, J. Pascual, D. Couzias, and M. Maza, “Characterization of additively manufactured triply periodic minimal surface structures under compressive loading,” *Mechanics of Advanced Materials and Structures*, 2020, doi: 10.1080/15376494.2020.1842948.
- [100] A. Anesari, M. Abdi, D. Ickman, and I. Ashcroft, “Strategies for functionally graded lattice structures derived using topology optimisation for Additive Manufacturing,” *Additive Manufacturing*, vol. 19, pp. 81–94, Jan. 2018, doi: 10.1016/j.addma.2017.11.008.
- [101] J. Maszybrocka, J. Gapiński, M. Dworak, G. Skrabalak, and A. Stwora, “The manufacturability and compression properties of the Schwarz Diamond type Ti6Al4V cellular lattice fabricated by selective laser melting,” *International Journal of Advanced Manufacturing Technology*, vol. 105, no. 7–8, pp. 3411–3425, Dec. 2019, doi: 10.1007/s00170-019-04422-6.
- [102] S. Khan, S. Masood, E. Ibrahim, and A. Ahmad, “Compressive behaviour of a novel Triply Periodic Minimal Surface cellular structure manufactured by fused deposition modelling,” *Virtual and Physical Prototyping*, vol. 14, no. 4, pp. 360–370, Oct. 2019, doi: 10.1080/17452759.2019.1615750.
- [103] D. W. Lee, K. A. Khan, and R. K. Abu Al-Rub, “Stiffness and yield strength of architected foams based on the Schwarz primitive triply periodic minimal surface,” *International Journal of Plasticity*, vol. 95, pp. 1–20, Aug. 2017, doi: 10.1016/j.ijplas.2017.03.005.
- [104] O. Al-Ketan and R. K. Abu Al-Rub, “Experimental investigations on the mechanical properties of new type of interpenetrating phase composite based on Schwarz Primitive triply periodic minimal surfaces,” *Composites Part B: Engineering*, vol. 165, pp. 1–12, Mar. 2019, doi: 10.1016/j.compositesb.2018.10.025.
- [105] A. P. G. Castro, R. B. Ruben, S. B. Gonçalves, J. Pinheiro, J. M. Guedes, and P. R. Fernandes, “Numerical and experimental evaluation of M-S Gyroid scaffolds for bone tissue engineering,” *Computer Methods in Biomechanics and Biomedical Engineering*, vol. 22, no. 6, pp. 567–573, Apr. 2019, doi: 10.1080/10255842.2019.1569638.
- [106] D. W. Abueidda, M. Elhebeary, C. S. (Andrew) Shiang, S. Pang, R. K. Abu Al-Rub, and I. M. Jasiuk, “Mechanical properties of 3D printed polymeric Gyroid cellular structures: Experimental and finite element study,” *Materials and Design*, vol. 165, Mar. 2019, doi: 10.1016/j.matdes.2019.107597.
- [107] S. I. Ranganathan and M. Ostoja-Starzewski, “Universal elastic anisotropy index,” *Physical Review Letters*, vol. 101, no. 5, Aug. 2008, doi: 10.1103/PhysRevLett.101.055504.
- [108] S. Pang, S. Pang, S. Imtiaz, S. Liu, and S. Gao, “Energy-Ratio-Based Measure of Elastic Anisotropy,” *Physical Review Letters*, vol. 122, no. 4, 2019, doi: 10.1103/PhysRevLett.122.045502.
- [109] R. Li, Q. Shao, E. Gao, and S. Liu, “Elastic anisotropy measure for two-dimensional crystals,” *Extreme Mech Lett*, vol. 34, Jan. 2020, doi: 10.1016/j.eml.2019.100615.
- [110] S. M. Kube, “Elastic anisotropy of crystals,” *AIP Advances*, vol. 6, no. 9, p. 95209, Sep. 2016, doi: 10.1063/1.4962996.
- [111] K. Liu, S. Wang, A. Wang, and S. Liu, “Surgical revision for stump problems after traumatic above-ankle amputations of the lower extremity,” *BMC Musculoskeletal Disorders*, vol. 16, no. 1, Mar. 2015, doi: 10.1186/S12891-015-0508-3.

- [112] B. . a ylor and A. oka , “ ste omyoplastic r anstibial Amputation he Ertl e chnique,” *Journal of the American Academy of Orthopaedic Surgeons*, vol. 24, no. 4, pp. 259–265, Apr. 2016, doi: 10.5435/JAAOS-D-15-00026.
- [113] “ ómo usar una prótesis.” <https://demo.staywellhealthlibrary.com/spanish/video-library/Content/healthsheets-v1/aprender-a-usar-una-protesis/> (accessed May 19, 2022).
- [114] B. J. Brown *et al.*, “Ertl below-knee amputation using a Vascularized fibular strut in a Nontrauma elderly population: A case series,” *Annals of Plastic Surgery*, vol. 73, no. 2, pp. 196–201, 2014, doi: 10.1097/SAP.0B013E318273F740.
- [115] . S. Deol, . . e e, and G. . erlet, “Evolution and Modi cation o the Ertl ste omyoplastic r anstibial Amputation,” *Operative Techniques in Orthopaedics*, vol. 18, no. 4, pp. 293–298, Oct. 2008, doi: 10.1053/J.OTO.2009.01.008.
- [116] . Jahmani and D. ale y, “Stump ve rgrowth a ter imb Amputation in hildren,” *Limb Amputation*, Dec. 2019, doi: 10.5772/INTECHOPEN.90532.
- [117] M. L. Mongon, F. A. Piva, S. Mistro Neto, J. A. Carvalho, W. D. Belangero, and B. Livani, “ ortical tibial osteoperiosteal lap technique to achieve bony bridge in transtibial amputation E pe rience in nine adult patients,” *Strategies in Trauma and Limb Reconstruction*, vol. 8, no. 1, pp. 37–42, Apr. 2013, doi: 10.1007/S11751-013-0152-0.
- [118] . A . De oster and S. omedan, “Amputation steoplasty,” *The Iowa Orthopaedic Journal*, vol. 26, p. 54, 2006, Accessed: Jul. 09, 2021. [Online]. Available: /pmc/articles/PMC1888592/
- [119] . o meister, . Schwarze, and . . Ascho , “Das Endo-Exo-Prothesen- e rsorgungskonzept e rbesserung der ebensqualität nach E tre mitätenamputation,” *Unfallchirurg*, vol. 120, no. 5, pp. 371–377, May 2017, doi: 10.1007/S00113-017-0350-1.
- [120] . o meister, . Schwarze, and . . Ascho , “Das Endo-Exo-Prothesen- e rsorgungskonzept e rbesserung der ebensqualität nach E tre mitätenamputation,” *Unfallchirurg*, vol. 120, no. 5, pp. 371–377, May 2017, doi: 10.1007/S00113-017-0350-1.
- [121] C. A. Donnelley *et al.*, “ ost Analyses o rosthetic Devices A Systematic eview,” *Archives of Physical Medicine and Rehabilitation*, vol. 102, no. 7, pp. 1404-1415.e2, Jul. 2021, doi: 10.1016/J.APMR.2021.02.010.
- [122] . a ishya and A. aish, “ D rinting in r thopedics,” *General Principles of Orthopedics and Trauma*, pp. 583–590, 2019, doi: 10.1007/978-3-030-15089-1_26.
- [123] A. aleem and M. Javaid, “ olyether ether ketone (EEK) and its D pr inted implants applications in medical ield An overview,” *Clinical Epidemiology and Global Health*, vol. 7, no. 4, pp. 571–577, Dec. 2019, doi: 10.1016/J.CEGH.2019.01.003.
- [124] Y. H. Yu and S. J. iu, “ olyetheretherketone or orthopedic applications a review,” *Current Opinion in Chemical Engineering*, vol. 32, Jun. 2021, doi: 10.1016/J.COACHE.2021.100687.
- [125] M. . hittle, “Gait Analysis,” *Gait Analysis*, 2007, doi: 10.1016/B978-0-7506-8883-3.X5001-6.
- [126] J. García de Jalón and E. ayo, “Kinematic and Dynamic Simulation o Multibody Systems,” 1994, doi: 10.1007/978-1-4612-2600-0.
- [127] “Equations o Motion o Mechanical Systems in a grange a riabes and Quasi- oordinates,” *Studies in Applied Mechanics*, vol. 28, no. C, pp. 49–81, Jan. 1992, doi: 10.1016/B978-0-444-98700-6.50007-X.
- [128] . M. ewmark, “A method o computation or structural dynamics. Journal o Engineering Mechanics,” *Journal of Engineering Mechanics, ASCE*, vol. 85(EM3), no. EM3, 1959.
- [129] S. Min, . K ikuchi, . . ark, S. Kim, and S. hang, “ ptimal topology design o structures under dynamic loads,” *Structural Optimization*, vol. 17, no. 2–3, pp. 208–218, Apr. 1999, doi: 10.1007/BF01195945.
- [130] . Gavrea, D. egrut, and . A. ot ra, “ h e newmark integration method or simulation o multibody systems Analytical considerations,” *American Society of Mechanical Engineers*,

- Design Engineering Division (Publication) DE*, vol. 118 B, no. 2, pp. 1079–1092, 2005, doi: 10.1115/IMECE2005-81770.
- [131] J. Hao and S. Wang, “Dynamic response topology optimization in the time domain using model reduction method,” *Structural and Multidisciplinary Optimization* 2015 53:1, vol. 53, no. 1, pp. 101–114, Sep. 2015, doi: 10.1007/S00158-015-1328-7.
- [132] S. Ghandriz, S. Führer, and S. Elmquist, “Structural topology optimization of multibody systems,” *Multibody System Dynamics*, vol. 39, no. 1–2, pp. 135–148, Jan. 2017, doi: 10.1007/S11044-016-9542-7.
- [133] R. Behrou and J. K. Guest, “Topology optimization for transient response of structures subjected to dynamic loads,” *18th AIAA/ISSMO Multidisciplinary Analysis and Optimization Conference, 2017*, 2017, doi: 10.2514/6.2017-3657.
- [134] M. Bendsoe, “Optimal shape design as a material distribution problem,” *Structural optimization* 1989 1:4, vol. 1, no. 4, pp. 193–202, Dec. 1989, doi: 10.1007/BF01650949.
- [135] J. K. Guest, J. S. Vost, and S. Elytschko, “Achieving minimum length scale in topology optimization using nodal design variables and projection functions,” *International Journal for Numerical Methods in Engineering*, vol. 61, no. 2, pp. 238–254, Sep. 2004, doi: 10.1002/NME.1064.
- [136] A. Azari, A. Moghadasi, and A. Ghelid, “Adjoint sensitivity analysis of flexible multibody systems in differential-algebraic form,” *Computers and Structures*, vol. 228, Feb. 2020, doi: 10.1016/J.COMPSTRUC.2019.106148.
- [137] S. Ambu and A. E. Morabito, “Modeling, assessment, and design of porous cells based on schwartz primitive surface for bone scaffolds,” *Scientific World Journal*, vol. 2019, 2019, doi: 10.1155/2019/7060847.
- [138] S. Bonatti and D. Mohr, “Smooth-shell metamaterials of cubic symmetry: Anisotropic elasticity, yield strength and specific energy absorption,” *Acta Materialia*, vol. 164, pp. 301–321, 2019, doi: 10.1016/j.actamat.2018.10.034.
- [139] A. Kashi and S. Saha, “Failure mechanisms of medical implants and their effects on outcomes,” *Biointegration of Medical Implant Materials*, pp. 407–432, Jan. 2019, doi: 10.1016/B978-0-08-102680-9.00015-9.
- [140] M. A. Marra *et al.*, “A Subject-Specific Musculoskeletal Modeling Framework to Predict in vivo Mechanics of Total Knee Arthroplasty,” *Journal of Biomechanical Engineering*, vol. 137, no. 2, 2015, doi: 10.1115/1.4029258.
- [141] C. A. Myers *et al.*, “The impact of hip implant alignment on muscle and joint loading during dynamic activities,” *Clinical Biomechanics*, vol. 53, 2018, doi: 10.1016/j.clinbiomech.2018.02.010.
- [142] G. Ghosh, “A first-principles study of cementite (Fe₃C) and its alloyed counterparts: Elastic constants, elastic anisotropies, and isotropic elastic moduli,” *AIP Advances*, vol. 5, no. 8, Aug. 2015, doi: 10.1063/1.4928208.
- [143] A. Fertiz, A. Goutin, A. Guech, and S. L. Odert, “Anisotropic elastic properties of flexible metal-organic frameworks: How soft are soft porous crystals?,” *Physical Review Letters*, vol. 109, no. 19, p. 195502, Nov. 2012, doi: 10.1103/PhysRevLett.109.195502.
- [144] D. A. Winter, *Biomechanics and Motor Control of Human Movement*. Hoboken, NJ, USA: John Wiley & Sons, Inc., 2009. doi: 10.1002/9780470549148.
- [145] S. E. Rodrigo, J. A. Ambrósio, M. J. da Silva, and S. Benise, “Analysis of human Gait based on Multibody formulations and optimization tools #,” <http://dx.doi.org/10.1080/15397730802425497>, vol. 36, no. 4, pp. 446–477, Oct. 2008, doi: 10.1080/15397730802425497.

- [146] S. Bauer *et al.*, “40th Anniversary Article: A Structure from Robots and Sensor Skin to Energy Harvesters,” *Advanced Materials*, vol. 26, no. 1, pp. 149–162, Jan. 2014, doi: 10.1002/ADMA.201303349.
- [147] A. Ag, S. S. Mukhopadhyay, and J. Kosel, “Wearable Flexible Sensors: A Review,” *IEEE Sensors Journal*, vol. 17, no. 13, pp. 3949–3960, Jul. 2017, doi: 10.1109/JSEN.2017.2705700.
- [148] A. Hait and S. E. Powers, “The Value of Reusable Feminine Hygiene Products Evaluated by Comparative Environmental Life Cycle Assessment,” *Resources, Conservation and Recycling*, vol. 150, p. 104422, Nov. 2019, doi: 10.1016/J.RESCONREC.2019.104422.
- [149] N. T. Tien *et al.*, “A Flexible Bimodal Sensor Array for Simultaneous Sensing of Pressure and Temperature,” *Advanced Materials*, vol. 26, no. 5, pp. 796–804, Feb. 2014, doi: 10.1002/ADMA.201302869.
- [150] D. J. Lipomi *et al.*, “Skin-like Pressure and Strain Sensors Based on Transparent Elastic Films of Carbon Nanotubes,” *Nature Nanotechnology* 2011 6:12, vol. 6, no. 12, pp. 788–792, Oct. 2011, doi: 10.1038/nnano.2011.184.
- [151] S. Sadri, D. Goswami, and S. Martinez, “Rapid Fabrication of Epidermal Paper-Based Electronic Devices Using Laser Printing,” *Micromachines* 2018, Vol. 9, Page 420, vol. 9, no. 9, p. 420, Aug. 2018, doi: 10.3390/MI9090420.
- [152] S. Khan, A. E. Steinfeld, S. M. Kochner, A. Pierre, and A. S. Arias, “Monitoring Vital Signs with Flexible and Wearable Medical Devices,” *Advanced Materials*, vol. 28, no. 22, pp. 4373–4395, Jun. 2016, doi: 10.1002/ADMA.201504366.
- [153] M. P. Wolf, G. B. Salieb-eugelaar, and S. Unzicker, “DMS with Designer Functionalities—Properties, Modification Strategies, and Applications,” *Progress in Polymer Science*, vol. 83, pp. 97–134, Aug. 2018, doi: 10.1016/J.PROGPOLYMSCI.2018.06.001.
- [154] C. M. Sánchez-González, J. F. Soriano-Peña, J. C. Rubio-Avalos, and J. J. Pacheco-Ibarra, “Fabrication of Flexible Piezoresistive Sensors Based on Poly-silicone and Milled Carbon Fibers and the Temperature’s Effect on Their Electric Resistance,” *Sensors and Actuators A: Physical*, vol. 302, p. 111811, Feb. 2020, doi: 10.1016/J.SNA.2019.111811.
- [155] S. Lochrane, S. Koncar, M. Lewandowski, and S. Duour, “Design and Development of a Flexible Strain Sensor for Textile Structures Based on a Conductive Polymer Composite,” *Sensors* 2007, Vol. 7, Pages 473-492, vol. 7, no. 4, pp. 473–492, Apr. 2007, doi: 10.3390/S7040473.
- [156] S. Maiti, S. K. Shrivastava, S. Suin, and S. Khatua, “Polystyrene/MWCNT/Graphite Nanoplate Nanocomposites: Efficient Electromagnetic Interference Shielding Material through Graphite Nanoplate–MWCNT–Graphite Nanoplate Networking,” *ACS Applied Materials and Interfaces*, vol. 5, no. 11, pp. 4712–4724, Jun. 2013, doi: 10.1021/AM400658H.
- [157] Y. Su *et al.*, “Piezoresistive Electronic-Skin Sensors Produced with Self-Channeling Laser Microstructured Silicon Molds,” *IEEE Transactions on Electron Devices*, vol. 68, no. 2, pp. 786–792, Feb. 2021, doi: 10.1109/TED.2020.3045962.
- [158] S. Reitelshöfer, M. Göttler, P. Schmidt, P. Treffer, M. Landgraf, and J. Franke, “Aerosol-Jet-Printing Silicone Layers and Electrodes for Stacked Dielectric Elastomer Actuators in One Processing Device,” <https://doi.org/10.1117/12.2219226>, vol. 9798, pp. 350–358, Apr. 2016, doi: 10.1117/12.2219226.
- [159] H. Yang, L. H. Gong, Z. Cheng, and S. Bao, “Highly Stretchable and Sensitive Conductive Rubber Composites with Tunable Piezoresistivity for Motion Detection and Flexible Electrodes,” *Carbon N Y*, vol. 158, pp. 893–903, Mar. 2020, doi: 10.1016/J.CARBON.2019.11.079.
- [160] J. Herzberger, J. M. Serrine, S. Williams, and E. Song, “Polymer Design for Printing Elastomers: Recent Advances in Structure, Properties, and Printing,” *Progress in Polymer Science*, vol. 97, p. 101144, Oct. 2019, doi: 10.1016/J.PROGPOLYMSCI.2019.101144.

- [161] A. Colpani, A. Fiorentino, and E. Cerretti, “Feasibility analysis and characterization of an extrusion-based AM process for a two-component and biocompatible silicone,” *Journal of Manufacturing Processes*, vol. 49, pp. 116–125, Jan. 2020, doi: 10.1016/J.JMAPRO.2019.11.017.
- [162] M. Khosravani and S. Heinicke, “3D-printed sensors: Current progress and future challenges,” *Sensors and Actuators A: Physical*, vol. 305, p. 111916, Apr. 2020, doi: 10.1016/J.SNA.2020.111916.
- [163] J. I. Martínez-López *et al.*, “Characterization of Soft Tooling Topopolymers and Processes of Micromixing Devices with Variable Cross-Section,” *Micromachines (Basel)*, vol. 11, no. 11, p. 970, Oct. 2020, doi: 10.3390/mi11110970.
- [164] S. Liu, J. Sun, and S. Li, “Process Analysis of Rapid Tooling Technology Used on Rapid Prototyping,” *Advanced Materials Research*, vol. 216, pp. 798–803, 2011, doi: 10.4028/WWW.SCIENTIFIC.NET/AMR.216.798.
- [165] D. Dempsey, S. McDonald, D. Masato, and S. Barry, “Characterization of Stereolithography Printed Soft Tooling for Micro Injection Molding,” *Micromachines 2020, Vol. 11, Page 819*, vol. 11, no. 9, p. 819, Aug. 2020, doi: 10.3390/MI11090819.
- [166] S. Rajaraman, J. A. Ragg, J. D. Ross, and M. G. Allen, “Micromachined three-dimensional electrode arrays for transcutaneous nerve tracking,” *Journal of Micromechanics and Microengineering*, vol. 21, no. 8, p. 085014, Jun. 2011, doi: 10.1088/0960-1317/21/8/085014.
- [167] D. Arata, J. Dias, S. Ieringa, S. Anlitterswijk, and S. Babovic, “Self-instructive high-resolution micropatterned polylactic acid surfaces,” *Biofabrication*, vol. 9, no. 3, p. 035004, Jul. 2017, doi: 10.1088/1758-5090/AA7D24.
- [168] S. Lv *et al.*, “Micro/nanofabrication of brittle hydrogels using 3D printed soft ultrafine fiber molds for damage-free demolding,” *Biofabrication*, vol. 12, no. 2, p. 025015, Feb. 2020, doi: 10.1088/1758-5090/AB57D8.
- [169] J. Z. Manapat, Q. Chen, P. Ye, and R. C. Advincula, “3D Printing of Polymer Nanocomposites via Stereolithography,” *Macromolecular Materials and Engineering*, vol. 302, no. 9, pp. 1–14, 2017, doi: 10.1002/mame.201600553.
- [170] J. A. R. Linares-Alvelais, J. Obedt Figueroa-Cavazos, C. Chuck-Hernandez, H. R. Siller, C. A. Rodríguez, and J. I. Martínez-López, “Quasistatic high-pressure post-processing of specimens fabricated by DLP, SLA, and FDM: An alternative for the sterilization of polymer-based biomedical devices,” *Materials*, vol. 11, no. 12, 2018, doi: 10.3390/ma11122540.
- [171] A. Ali *et al.*, “Kinetic and thermal study of ethylene and propylene homo polymerization catalyzed by zirconocene activated with alkylaluminum/borate: Effects of alkylaluminum on polymerization kinetics and polymer structure,” *Polymers (Basel)*, vol. 13, no. 2, pp. 1–20, Jan. 2021, doi: 10.3390/polym13020268.
- [172] S. K. Kumar, A. Kumar, S. S. Sain, and S. S. Sark, “Silicone rubber composites reinforced with carbon nanotubes, titanium-dioxide and their hybrid: Mechanical and piezoelectric actuation performance,” *Nano Materials Science*, vol. 3, no. 3, pp. 233–240, Sep. 2021, doi: 10.1016/J.NANOMS.2020.12.002.
- [173] K. Chelara, S. Seluri, S. S. Hang, M. Madhav, and S. S. Hiu, “Cationic-induced modifications in microstructure and properties of PBAT/PP blend: Enhanced rigidity, heat resistance, and electrical conductivity,” *Polymer (Guildf)*, vol. 203, p. 122758, Aug. 2020, doi: 10.1016/J.POLYMER.2020.122758.
- [174] N. M. Nurazzi *et al.*, “Mechanical Performance and Applications of Self-Reinforced Polymer Composites—A Review,” *Nanomaterials 2021, Vol. 11, Page 2186*, vol. 11, no. 9, p. 2186, Aug. 2021, doi: 10.3390/NANO11092186.
- [175] S. K. Kumar, M. A. Alam, A. Manikkavel, M. Song, D. J. Lee, and S. S. Sark, “Silicone Rubber Composites Reinforced by Carbon Nanofillers and Their Hybrids for Various Applications: A

- review,” *Polymers 2021, Vol. 13, Page 2322*, vol. 13, no. 14, p. 2322, Jul. 2021, doi: 10.3390/POLYM13142322.
- [176] A. D. Mazzeo and D. E. a rdt, “ entri ugal casting o micro luidic components with DMS,” *Journal of Micro and Nano-Manufacturing*, vol. 1, no. 2, Jun. 2013, doi: 10.1115/1.4023754/380381.
- [177] . . Kuo, M. . u, and M. . a i, “Development o a ow -Cost Automatic Vacuum Degassing System or apid ool ing,” *Applied Mechanics and Materials*, vol. 459, pp. 349–355, 2014, doi: 10.4028/WWW.SCIENTIFIC.NET/AMM.459.349.
- [178] G. Vakili-Nezhaad and A. Dorany, “E ect o Single-Walled Carbon Nanotube on the Viscosity o ubricants,” *Energy Procedia*, vol. 14, pp. 512–517, Jan. 2012, doi: 10.1016/J.EGYPRO.2011.12.967.
- [179] S. I. Kundalwal and A. athi, “Improved mechanical and viscoelastic properties o T-composites abricated using an innovative ultrasonic dual mi i ng technique,” *Journal of the Mechanical Behavior of Materials*, vol. 29, no. 1, pp. 77–85, Jan. 2020, doi: 10.1515/JMBM-2020-0008/MACHINEREAADABLECITATION/RIS.
- [180] M. Cheng *et al.*, “A review o le ible orce sensors or human health monitoring,” *Journal of Advanced Research*, vol. 26, pp. 53–68, Nov. 2020, doi: 10.1016/J.JARE.2020.07.001.
- [181] AS M I nternational, “AS M D -06a: Vulcanized Rubber and Thermoplastic Elastomers– e nsion,” *ASTM International*, vol. i, no. Reapproved 2013, pp. 1–14, 2021, [Online]. Available: <http://scholar.google.com/scholar?hl=en&btnG=Search&q=intitle:Standard+Test+Methods+for+Vulcanized+Rubber+and+Thermoplastic+Elastomers+?+Tension#0>
- [182] . K. uo, “Mullins damage e ect on rubber products with residual strain,” *International Journal of Damage Mechanics*, vol. 24, no. 2, pp. 153–167, Feb. 2014, doi: 10.1177/1056789514522504.
- [183] J. ergström, “Mechanics o Solid olymers he ory and omputational Modeling,” *Mechanics of Solid Polymers: Theory and Computational Modeling*, pp. 1–509, Jun. 2015, doi: 10.1016/C2013-0-15493-1.
- [184] J. . a garias, J. A. eeds, M. . right, and . E. right, “ onvergence roperties o the Nelder--Mead Simple Method in ow Dimensions,” <http://dx.doi.org/10.1137/S1052623496303470>, vol. 9, no. 1, pp. 112–147, Jul. 2006, doi: 10.1137/S1052623496303470.
- [185] A. International, “AS M D 7 S tandard test methods or D re sistance or conductance o insulating materials,” *Standard*, vol. i, no. C, 2007.
- [186] . . gde n and D. G. o bur gh, “A pseudoelastic model or the Mullins e ect in illed rubber,” *Proceedings of the Royal Society of London. Series A: Mathematical, Physical and Engineering Sciences*, vol. 455, no. 1988, pp. 2861–2877, 1999, doi: 10.1098/RSPA.1999.0431.
- [187] W. Xu *et al.*, “Stress-Softening in Particle-Filled Polyurethanes under Cyclic Compressive oa ding,” *Polymers 2020, Vol. 12, Page 1588*, vol. 12, no. 7, p. 1588, Jul. 2020, doi: 10.3390/POLYM12071588.
- [188] D. De omm asi, D. erri, G. . Mar ano, and G. ugli isi, “Material parameters identi cation and experimental validation of damage models or rubberlike materials,” *European Polymer Journal*, vol. 78, pp. 302–313, May 2016, doi: 10.1016/J.EURPOLYMJ.2016.03.036.
- [189] J. ergstrom, “M alibra tion.” ol ymer EM,
- [190] . . Etschke, . D . ornes, and D. . aul, “ he ological behavior of multiwalled carbon nanotube polycarbonate composites”.
- [191] . . udyak, A. . Minakov, and M. I. ryazhnikov, “ reparation, characterization, and viscosity studding the single-walled carbon nanotube nano luids,” *Journal of Molecular Liquids*, vol. 329, p. 115517, May 2021, doi: 10.1016/J.MOLLIQ.2021.115517.

- [192] J. D. Arrett, “Taguchi’s Quality Engineering Handbook,” <http://dx.doi.org/10.1198/tech.2007.s480>, vol. 49, no. 2, pp. 224–225, May 2012, doi: 10.1198/TECH.2007.S480.
- [193] P. Polytechnica and S. M. Eng, “Influence of Mold Properties on the Quality of Injection Molded Parts,” *Periodica Polytechnica Mechanical Engineering*, vol. 49, no. 2, pp. 115–122, Oct. 2005, doi: n/a.
- [194] S. Link, K. Kovács, and J. G. Kovács, “Thermal analysis based method development for novel rapid tooling applications,” *International Communications in Heat and Mass Transfer*, vol. 108, p. 104297, Nov. 2019, doi: 10.1016/J.ICHEATMASSTRANSFER.2019.104297.
- [195] J. R. C. Dizon, A. D. Valino, L. R. Souza, A. H. Espera, Q. Chen, and S. S. Advincula, “Three-dimensional-printed molds and materials for injection molding and rapid tooling applications,” *MRS Communications*, vol. 9, no. 4, pp. 1267–1283, 2019, doi: 10.1557/MRC.2019.147.
- [196] N. Hanumaiah, B. Ravi, and N. S. Mukherjee, “Rapid hard tooling process selection using Q-D-A methodology,” *Journal of Manufacturing Technology Management*, vol. 17, no. 3, pp. 332–350, 2006, doi: 10.1108/17410380610648290/FULL/XML.
- [197] G. G. Rigatos, “Advanced models of neural networks: Nonlinear dynamics and stochasticity in biological neurons,” *Advanced Models of Neural Networks: Nonlinear Dynamics and Stochasticity in Biological Neurons*, pp. 1–275, Jan. 2015, doi: 10.1007/978-3-662-43764-3.
- [198] J. C. Coulombe, M. C. A. York, and J. Sylvestre, “Computing with networks of nonlinear mechanical oscillators,” *PLOS ONE*, vol. 12, no. 6, p. e0178663, Jun. 2017, doi: 10.1371/JOURNAL.PONE.0178663.
- [199] G. Rödönyi *et al.*, “Identification of the nonlinear steering dynamics of an autonomous vehicle,” *IFAC-PapersOnLine*, vol. 54, no. 7, pp. 708–713, Jan. 2021, doi: 10.1016/J.IFACOL.2021.08.444.
- [200] A. Yousefpour, H. Jahanshahi, J. M. Muñoz-Acheco, S. Ekiros, and S. Hei, “A fractional-order hyper-chaotic economic system with transient chaos,” *Chaos, Solitons & Fractals*, vol. 130, p. 109400, Jan. 2020, doi: 10.1016/J.CHAOS.2019.109400.
- [201] J. García-Ávila, C. A. Rodríguez, A. Vargas-Martínez, E. Ramírez-Cedillo, and J. Israel Martínez-Óppez, “E-Skin Development and Prototyping via Soft Tooling and Composites with Silicone Rubber and Carbon Nanotubes,” *Materials (Basel)*, vol. 15, no. 1, Jan. 2021, doi: 10.3390/MA15010256.
- [202] A. Onanti, J. Kaplan, G. Haras, and A. Kabla, “Fractional viscoelastic models for power-law materials,” *Soft Matter*, vol. 16, no. 26, pp. 6002–6020, Jul. 2020, doi: 10.1039/D0SM00354A.
- [203] “Locomotion Laboratory.” http://lau.labor.it-tud.de/doku.php?id=projects:projects_walkrunankle (accessed May 21, 2022).
- [204] J. Schmidhuber, “Deep learning in neural networks: An overview,” *Neural Networks*, vol. 61, pp. 85–117, Jan. 2015, doi: 10.1016/J.NEUNET.2014.09.003.
- [205] S. Grech, M. Muzio, M. Gentella, and S. Sammut, “Dynamic ferromagnetic hysteresis modelling using a Preisach-recurrent neural network model,” *Materials*, vol. 13, no. 11, Jun. 2020, doi: 10.3390/MA13112561.
- [206] M. Cho, J. Lee, S. Kim, J. S. Kim, and S. Similsina, “An Extremely Simple, and Flexible Carbon Fiber Electrode for Tunable Elastomeric Piezo-Resistive Sensors and Devices Realized by S/M,” *ACS Applied Materials and Interfaces*, vol. 11, no. 12, pp. 11910–11919, Mar. 2019, doi: 10.1021/ACSAMI.9B00464.
- [207] J. M. Montanero and A. M. Gálvez-Alvó, “Dripping, jetting and tip streaming,” *Reports on Progress in Physics*, vol. 83, no. 9, p. 097001, Aug. 2020, doi: 10.1088/1361-6633/ABA482.

- [208] K. Suzuki, M. Hirai, and M. Hozono, “ Oscillating friction on shape-tunable wrinkles,” *ACS Applied Materials and Interfaces*, vol. 6, no. 13, pp. 10121–10131, Jul. 2014, doi: 10.1021/AM5010738.
- [209] S. Arunkumar, “ Overview of Small punch test,” *Metals and Materials International*, vol. 26, no. 6, pp. 719–738, Jun. 2020, doi: 10.1007/S12540-019-00454-5/FIGURES/13.
- [210] ASTM, “ D638-02: Standard Test Method for Small Punch Testing of Ultra-High Molecular Weight Polyethylene Used in Surgical Implants ,” *ASTM Book of Standards*, vol. 13.01, no. Reapproved 2008, 2008.
- [211] M. Garg and S. Tang, “A mass-spring-damper model of a bouncing ball,” *Proceedings of the American Control Conference*, vol. 1, pp. 499–504, 2004, doi: 10.23919/ACC.2004.1383652.
- [212] M. Hecht, M. Ludwig, S. Dorbolo, and M. Vandewalle, “ Bouncing dynamics of a spring,” *Physica D: Nonlinear Phenomena*, vol. 272, pp. 1–7, Apr. 2014, doi: 10.1016/J.PHYSD.2014.01.002.
- [213] J.-Y. Chastaing, E. Bertin, and J.-M. G eminard, “Dynamics of a bouncing ball,” *American Journal of Physics*, vol. 83, no. 6, pp. 518–524, Jun. 2015, doi: 10.1119/1.4906418.
- [214] M. Pizzoli, F. Saltari, F. Mastroddi, J. Martinez-Carrascal, and L. M. Gonz alez-Guti errez, “ Online reduced-order model for vertical sloshing by employing neural networks,” *Nonlinear Dynamics*, vol. 107, no. 2, pp. 1469–1478, Jan. 2022, doi: 10.1007/S11071-021-06668-W/FIGURES/8.
- [215] M. Chen, A. Linderholt, and T. Abrahamsson, “An efficient simulation method for large-scale systems with local nonlinearities,” *Conference Proceedings of the Society for Experimental Mechanics Series*, vol. 6, pp. 259–267, 2016, doi: 10.1007/978-3-319-29910-5_27.
- [216] Y. Chen, A. Linderholt, and T. Abrahamsson, “An efficient simulation method for large-scale systems with local nonlinearities,” *Conference Proceedings of the Society for Experimental Mechanics Series*, vol. 6, pp. 259–267, 2016, doi: 10.1007/978-3-319-29910-5_27.

VITA

Josué García-Ávila, from Guerrero, México. He earned a Bachelor's degree in Mechatronics Engineering from Universidad Anáhuac and upon defending this thesis will confer a Master's degree in Manufacturing Systems at Tecnológico de Monterrey, where he was graduate student of Advanced Manufacturing Research Group. He worked in the automotive industry as a Sr. Manufacturing Engineer (Machining & Assembly) at Bocar Group during several years and lived in Costa Rica for 2 years doing humanitarian work. Now, his research interests include data-driven mechanics of architected, multifunctional, sustainable, soft, and stretchable materials to mimetic artificial living matter for biomedical applications and beyond. Josué has a couple of first-author publications and was recipient of academic scholarship by National Council of Science and Technology of Mexico (CONACyT) during his master studies. He will be pursuing a PhD's degree in Mechanical Engineering at Stanford School of Engineering and is award, by nomination of the graduate admissions committee, the EDGE Doctoral Fellowship.

E-mail Address: josue.g.avila@gmail.com